CERN/LHCC/2000-0036
LHCb TDR 2
6 September 2000

LHCb Calorimeters

Technical Design Report

11

The LHCb Collaboration [1]

University of Rio de Janeiro, UFRJ, Rio de Janeiro, Brasil
S.Amato, D.Carvalho, P.Colrain, T.da Silva, J.R.T.de Mello, L.de Paula, M.Gandelman, J.Helder Lopes, B.Marechal, D.Moraes, E.Polycarpo

University of Clermont-Ferrand II, Clermont-Ferrand, France
Z.Ajaltouni, G.Bohner, V.Breton, R.Cornat, O.Deschamps, A.Falvard, J.Lecoq, P.Perret, C.Trouilleau, A.Ziad

CPPM Marseille, Aix University-Marseille II, Marseille, France
E.Aslanides, J.P.Cachemiche, R.Le Gac, O.Leroy, M.Menouni, R.Potheau, A.Tsaregorodtsev

University of Paris-Sud, LAL Orsay, Orsay, France
G.Barrand, C.Beigbeder-Beau, D.Breton, T.Caceres, O.Callot, R.Cizeron, Ph.Cros, B.D'Almagne, B.Delcourt, F.Fulda Quenzer, A.Hrisoho, B.Jean-Marie, J.Lefrancois, J.M.Noppe, V.Tocut, K.Truong

Humboldt University, Berlin, Germany
T.Lohse

Technical University of Dresden, Dresden, Germany
R.Schwierz, B.Spaan

University of Freiburg, Freiburg, Germany
H.Fischer, J.Franz, F.H.Heinsius, K.Königsmann, H.Schmitt

Max-Planck-Institute for Nuclear Physics, Heidelberg, Germany
C.Bauer, D.Baumeister, N.Bulian, H.P.Fuchs, T.Glebe, W.Hofmann, K.T.Knöpfle, S.Löchner, M.Schmelling, B.Schwingenheuer, F.Sciacca, E.Sexauer, U.Trunk

Physics Institute, University of Heidelberg, Heidelberg, Germany
S.Bachmann, P.Bock, H.Deppe, H.B.Dreis, F.Eisele, M.Feuerstack-Raible, S.Henneberger, P.Igo-Kemenes, Ch.Rummel, R.Rusnyak, U.Stange

Kirchhoff Institute for Physics, University of Heidelberg, Heidelberg, Germany
V.Lindenstruth, R.Richter, M.W.Schulz, A.Walsch

[1] This list includes few additional colleagues who made particular contributions to the work presented in this TDR.

Frascati Laboratori Nazionali, Frascati, Italy
G.Bencivenni, C.Bloise, F.Bossi, P.Campana, G.Capon, P.DeSimone, C.Forti, M.Murtas, L.Passalacqua, V.Patera(1), L.Satta(1), A. Sciubba(1)
(1) also at Dipartimento di Energetica, University of Rome, "La Sapienza"

University of Bologna and INFN, Bologna, Italy
M.Bargiotti, A.Bertin, M.Bruschi, M.Capponi, I.D'Antone, S.Castro, R.Dona, D.Galli, B.Giacobbe, U.Marconi, I.Massa, M.Piccinini, M.Poli, N.Semprini-Cesari, R.Spighi, V.Vagnoni, S.Vecchi, M.Villa, A.Vitale, A.Zoccoli

University of Cagliari and INFN, Cagliari, Italy
W.Bonivento, A.Cardini, M.Caria, A.Lai, D.Pinci, B.Saitta

University of Ferrara and INFN, Ferrara, Italy
V.Carassiti, A.Cotta Ramusino, P.Dalpiaz, A.Gianoli, M.Martini, F.Petrucci, M.Savrie

University of Florence and INFN, Florence, Italy
A.Bizzeti, M.Calvetti, E.Iacopini, M.Lenti, F.Martelli, G.Passaleva, M.Veltri

University of Genoa and INFN, Genoa, Italy
S.Cuneo, F.Fontanelli, V.Gracco, P.Musico, A.Petrolini, M.Sannino

University of Milano and INFN, Milano, Italy
M.Alemi, T.Bellunato, M.Calvi, C.Matteuzzi, P.Negri, M.Paganoni, V.Verzi

University of Rome, "La Sapienza" and INFN, Rome, Italy
G.Auriemma, V.Bocci, C.Bosio, G.Chiodi, D.Fidanza, A.Frenkel, K.Harrison, S.Mari, G.Martellotti, S.Martinez, G.Penso, R.Santacesaria, C.Satriano, A.Satta

University of Rome, "Tor Vergata" and INFN, Rome, Italy
G.Carboni, D.Domenici, R.Messi, L.Pacciani, L.Paoluzi, E.Santovetti

NIKHEF, The Netherlands
T.S.Bauer(4), M.Doets(1,2), Y.Gouz(1,5), V.Gromov(1), R.Hierck(1), L.Hommels(1), E.Jans(1), T.Ketel(2), S.Klous (2), B.Koene(1), M.Merk(1), M.Needham(1), H.Schuijlenburg(1), T.Sluijk(1), L.Wiggers(1), G.van Apeldoorn(3), N.van Bakel(1,2), J.van den Brand(2), R.van der Eijk(1), N.Zaitsev(3,6)
(1) Foundation of Fundamental Research of Matter in the Netherlands,
(2) Free University Amsterdam,
(3) University of Amsterdam,
(4) University of Utrecht,
(5) On leave from Protvino,
(6) On leave from Petersburg

Institute of High Energy Physics, Beijing, P.R.C.
C.Gao, C.Jiang, H.Sun, Z.Zhu

Research Centre of High Energy Physics, Tsinghua University, Beijing, P.R.C.
M.Bisset, J.P.Cheng, Y.G.Cui, Y.Gao, H.J.He, Y.P.Kuang, Y.J.Li, Y.Liao, Q.Lin, J.P.Ni, B.B.Shao, J.J.Su, Y.R.Tian, Q.Wang, Q.S.Yan

Institute for Nuclear Physics and University of Mining and Metalurgy, Krakow, Poland
E.Banas, J.Blocki, K.Galuszka, P.Jalocha, P.Kapusta, B.Kisielewski, W.Kucewicz, T.Lesiak, J.Michalowski, B.Muryn, Z.Natkaniec, W.Ostrowicz, G.Polok, E.Rulikowska-Zarebska, M.Stodulski, M.Witek, P.Zychowski

Soltan Institute for Nuclear Physics, Warsaw, Poland
M.Adamus, A.Chlopik, Z.Guzik, A.Nawrot, M.Szczekowski

Horia Hulubei-National Institute for Physics and Nuclear Engineering (IFIN-HH), Bucharest-Magurele, Romania
D.V.Anghel, C.Coca, D.Dumitru, G.Giolu, C.Magureanu, R.Petrescu, S.Popescu, T.Preda, A.M.Rosca, V.L.Rusu

Institute for Nuclear Research (INR), Moscow, Russia
V.Bolotov, S.Filippov, J.Gavrilov, E.Guschin, V.Kloubov, L.Kravchuk, S.Laptev, V.Laptev, V.Postoev, A.Sadovski, I.Semeniouk

Institute of Theoretical and Experimental Physics (ITEP), Moscow, Russia
S.Barsuk, I.Belyaev, A.Golutvin, O.Gouchtchine, V.Kiritchenko, G.Kostina, N.Levitski, A.Morozov, P.Pakhlov, D.Roussinov, V.Rusinov, S.Semenov, A.Soldatov, E.Tarkovski

P.N.Lebedev Physical Institute, Moscow, Russia
Yu.Alexandrov, V.Baskov, L.Gorbov, B.Govorkov, V.Kim, P.Netchaeva, V.Polianski, L.Shtarkov, A.Verdi, M.Zavertiaev

Institute for High Energy Physics (IHEP-Serpukhov), Protvino, Russia
I.V.Ajinenko, K.Beloous, V.Brekhovskikh, S.Denissov, R.I.Dzhelyadin, A.V.Dorokhov, A.Kobelev, A.K.Konoplyannikov, A.K.Likhoded, V.D.Matveev, V.Novikov, V.F.Obraztsov, A.P.Ostankov, V.I.Rykalin, V.K.Semenov, M.M.Shapkin, N.Smirnov, M.M.Soldatov, A.Sokolov, V.V.Talanov, O.P.Yushchenko

Petersburg Nuclear Physics Institute, Gatchina, St.Petersburg, Russia
B.Botchine, S.Guetz, V.Lazarev, N.Saguidova, V.Souvorov, E.Spiridenkov, A.Vorobyov, An.Vorobyov

University of Barcelona, Barcelona, Spain
S.Botta Ferragut, A.Dieguez, L.Garrido Beltran, D.Gascon, S.Gomez, R.Miquel, D.Peralta-Rodriguez, M.Rosello Canal(1), X.Vilasis Cardona(1)
(1)Departament d'Engineria Electronica La Salle, Universitat Ramon Llull, Barcelona

University of Santiago de Compostela, Santiago de Compostela, Spain
B.Adeva, P.Conde, F.Gomez, J.A.Hernando, A.Iglesias, A.Lopez-Aguera, A.Pazos, M.Plo, J.M.Rodriguez, J.J.Saborido, M.J.Tobar

University of Lausanne, Lausanne, Switzerland
P.Bartalini, A.Bay, C.Currat, O.Dormond, F.Dürrenmatt, Y.Ermoline, R.Frei, G.Gagliardi, J.P.Hertig, G.Haefeli, P.Koppenburg, J.P.Perroud, F.Ronga, O.Schneider, L.Studer, M.Tareb, M.T.Tran

University of Zürich , Zürich, Switzerland
R.Bernet, E.Holzschuh, P.Sievers, O.Steinkamp, U.Straumann, D.Wyler, M.Ziegler

Institute of Physics and Technologies, Kharkiv, Ukraine
S.Maznichenko, O.Omelaenko, Yu.Ranyuk, M.V.Sosipatorow

Institute for Nuclear Research, Kiev, Ukraine
V.Aushev, V.Kiva, I.Kolomiets, Yu.Pavlenko, V.Pugatch, Yu.Vasiliev, V.Zerkin

University of Bristol, Bristol, U.K.
N.Brook, R.Head, F.Wilson

University of Cambridge, Cambridge, U.K.
V.Gibson, S.G.Katvars, C.R.Jones, C.Shepherd-Themistocleous, C.P.Ward, D.R.Ward, S.A.Wotton

Rutherford Appleton Laboratory, Chilton, U.K.
C.A.J.Brew, C.J.Densham, S.Easo, B.Franek, J.G.V.Guy, R.N.J.Halsall, J.A.Lidbury, J.V.Morris, A.Papanestis, G.N.Patrick, F.J.P.Soler, S.A.Temple

University of Edinburgh, Edinburgh, U.K.
S.Eisenhardt, A.Khan, F.Muheim, S.Playfer, A.Walker

University of Glasgow, Glasgow, U.K.
A.J.Flavell, A.Halley, V.O'Shea, F.J.P.Soler

University of Liverpool, Liverpool, U.K.
S.Biagi, T.Bowcock, R.Gamet, P.Hayman, M.McCubbin, C.Parkes, G.Patel, S.Walsh, V.Wright

Imperial College, London, U.K.
G.J.Barber, D.Clark, P.Dauncey, A.Duane, J.Hassard, R.Hill, M.J.John, D.R.Price, P.Savage, B.Simmons, L.Toudup, D.Websdale

University of Oxford, Oxford, U.K
M.Adinolfi, J.Bibby, M.J.Charles, N.Harnew, F.Harris, I.McArthur, J.Rademacker, N.J.Smale, S.Topp-Jorgensen, G.Wilkinson

CERN, Geneva, Switzerland
J.André, F.Anghinolfi, A.Augustinus, P.Binko, M.Bonnet, A.Braem, B.Bruder, J.Buytaert, M.Campbell, A.Cass, M.Cattaneo, P.Charra, E.Chesi, J.Christiansen, R.Chytracek, J.Closier, G.Corti, C.D'Ambrosio, H.Dijkstra, D.Dominguez, J.P.Dufey, M.Ferro-Luzzi, F.Fiedler, W.Flegel, F.Formenti, R.Forty, M.Frank, I.Garcia Alfonso, C.Gaspar, G.Gracia Abril, T.Gys, F.Hahn, S.Haider, J.Harvey, B.Hay, H.J.Hilke, A.Jacholkowska(1), R.Jacobsson, P.Jarron, C.Joram, B.Jost, A.Kashchuk(3), I.Korolko(2), D.Lacarrère, M.Laub, M.Letheren, J.F.Libby, R.Lindner, M.Losasso, P.Mato Vila, H.Müller, T.Nakada(4), J.Ocariz, S.Probst, F.Ranjard, W.Riegler, F.Rohner, T.Ruf, B.Schmidt, T.Schneider, A.Schöning, A.Schopper, W.Snoeys, W.Tejessy, F.Teubert, O.Ullaland, A.Valassi, E.van Herwijnen, P.Vazquez Regueiro, I.Videau(1), F.Vinci do Santos, G.von Holtey, P.Wicht, A.Wright, K.Wyllie, P.Wertelaers, M.Zuin
(1) on leave from LAL, Orsay
(2) on leave from ITEP, Moscow
(3) on leave from PNPI, Gatchina
(4) also at University of Lausanne

Acknowledgments

The Calorimeter Group and the LHCb Collaboration are greatly indebted to all the technical and administrative staff for their important contributions to the design, testing and prototype activities. We are grateful for their dedicated work and are aware that the successful construction and commissioning of the LHCb calorimeters will also in future depend on their skills and commitment.

Contents

Chapter 1 Introduction

The LHCb experiment makes use of the high production rate of B particles at the LHC collider to perform a thorough study of the CP-symmetry violation in the neutral B-meson systems. The peaking of $b\bar{b}$-pair production at small angles to the beams leads to a fixed-target like structure of the experimental setup which has been described in the LHCb technical proposal [1].

The calorimeter system is used at several stages. It provides high transverse energy hadron, electron and photon candidates for the first trigger level, which makes a decision 4 microseconds after the interaction. It provides the identification of electrons which is essential to flavour tagging through semileptonic decays. The reconstruction with good accuracy of π^0 and prompt photons gives access to the study of B-meson decay channels which are important to the complete physics program.

The present document is based on concepts which were already present in the technical proposal. Since then, much development work has taken place. It is thoroughly described in the notes quoted in reference. The studies have been performed in the following directions :

- Software developments, and simulation: the study of the expected physics performance has led to the optimization of the detector geometry, in particular the choice of the cell sizes. The trigger scheme has been fully worked out, and has in particular influenced the delimitation of the detector zones, as well as the structure of the readout electronics.

- Prototype studies: prototype elements of the various detectors and of electronics have been, and are still studied, an extensive test beam activity being devoted to these measurements. The results have been used to validate the detector concepts, and perform some basic technical choices.

- Construction technology: the basic engineering design of the detectors has been produced. These documents show how they can be constructed, and what resources will be needed.

With respect to the technical proposal, the present report brings a few major differences. One is the implementation of the scintillator pad detector (SPD), signaling the presence of a charged particle by means of the same technology as that of the preshower detector (PS). The cell geometry has been strongly modified, and the HCAL depth reduced. Several basic choices have been made. The SPD and PS will be readout by multianode photomultipliers; the choice by the trigger group of the 2×2 cells clustering

option implies that a large part of the Level 0 electronics is implemented on the front end boards, making the whole system economic in high speed connections.

Chapter 2 Performance Requirements and Detector Specifications

The main purpose of the calorimeter system is the identification of hadrons, electrons and photons, and the measurement of their energies and positions. This information is the basis of the Level 0 trigger, and therefore has to be provided with sufficient selectivity in a very short time. The set of constraints resulting from this functionality defines the general structure and the main characteristics of the calorimeter system and its associated electronics [1]. The ultimate performance for hadron and electron identification will be obtained at the off line analysis level. This stage, however, has little influence on the detector design.

The other essential function of the calorimeter system is the detection of photons with enough precision to enable the reconstruction of B-decay channels containing a prompt photon or π^0. The requirement of a good background rejection and reasonable efficiency for these channels adds demanding conditions on the detector performance in terms of resolution and shower separation. Economic reasons however excluded questioning the basic technical choices defined when preparing the technical proposal. The study of two benchmark channels has been used to optimize the design and demonstrate that these physics goals could be reached [2].

2.1 General detector structure

The general structure is that of an electromagnetic calorimeter (ECAL) followed by a hadron calorimeter (HCAL). The most demanding identification is that of electrons. Within the bandwidth allocated to the electron trigger (as defined in the technical proposal [1]) the electron Level 0 trigger will be useful if, while rejecting 99% of inelastic pp interactions, it provides an enrichment factor of at least 15 in B events. The rejection of the high background of charged pions requires the longitudinal segmentation of the electromagnetic shower detection, i.e. a preshower detector. The optimization of its thickness (2 X_0) results from a compromise between trigger performance and ultimate energy resolution [3]. The electron trigger is then confronted to the background of the high E_T π^0 tail. This is reduced by the introduction of the scintillator pad detector (SPD) plane in front of the preshower (PS). At Level 0, the background to the electron trigger will then be dominated by photon conversions in the spectrometer material, which cannot be identified at this stage.

To get optimal energy resolution for high energy photon showers, the ECAL must be thick enough. 25 X_0 are necessary [4]. On the other hand, the trigger requirements on

the HCAL resolution do not impose a stringent shower confinement condition. Its length has therefore been set to 5.6 interaction lengths [5].

2.2 Geometrical acceptance and transverse granularity

For the reconstruction of B decays, the calorimeter acceptance should match that of the charged particles spectrometer. The trigger efficiency is shown to have a weak dependence on the outer detector size. Hence the choice of outer limits of 300 mrad horizontally and 250 mrad vertically. At small angles, the background increases rapidly, and a central hole of 30 mrad in both directions avoids severe radiation damage and occupancy problems.

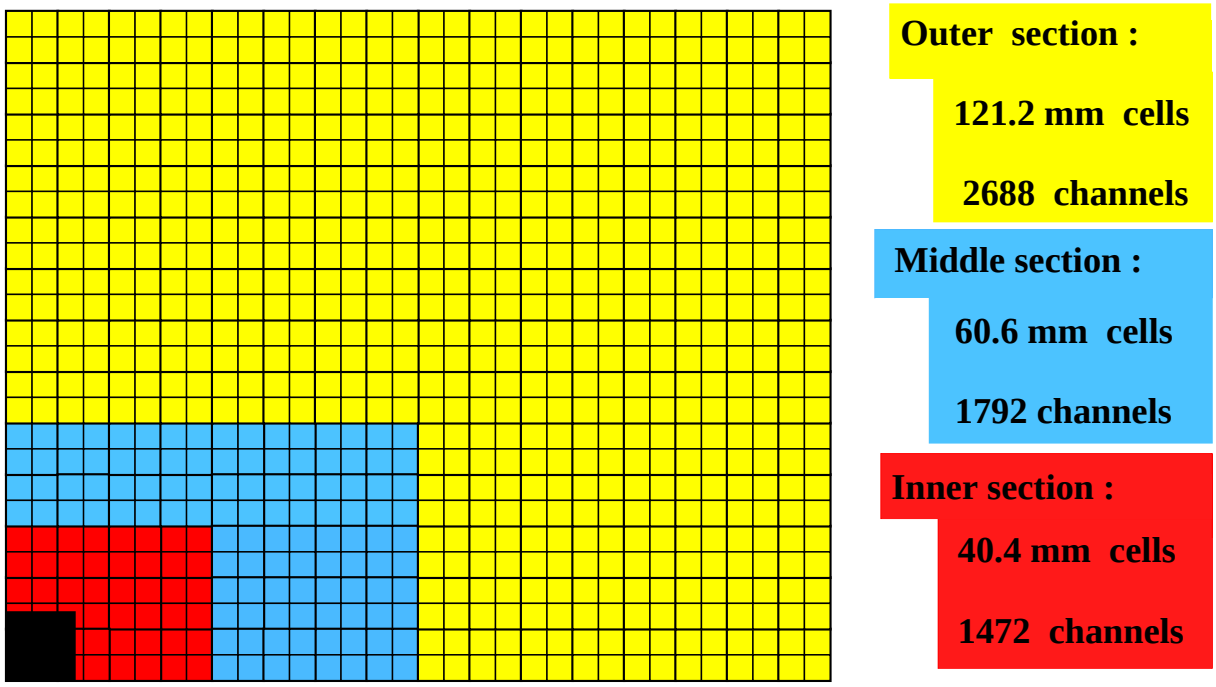

Figure 2.1: *Lateral segmentation of the SPD/PS and ECAL. One quarter of the detector front face is shown. The cells dimensions are given for ECAL and reduce by ≈1.5% for SPD/PS.*

The hit density varies by two orders of magnitude over the calorimeter surface. It is therefore natural to adopt a variable lateral segmentation. A segmentation in three different cell-size zones has been chosen for ECAL (see Fig. 2.1). The most demanding request is the separation of the two showers from high-energy π^0. In the innermost region of the ECAL, the cell size is close to the Moliere radius, so that most of the energy of an isolated shower is contained in a quartet of cells. The cell repartition between the three zones has been optimized, taking the total number of about 6000 channels as a constraint.

Given the dimensions of the hadronic showers and the performance requirements of the hadron trigger, the HCAL cells were chosen larger than those of ECAL and a lateral

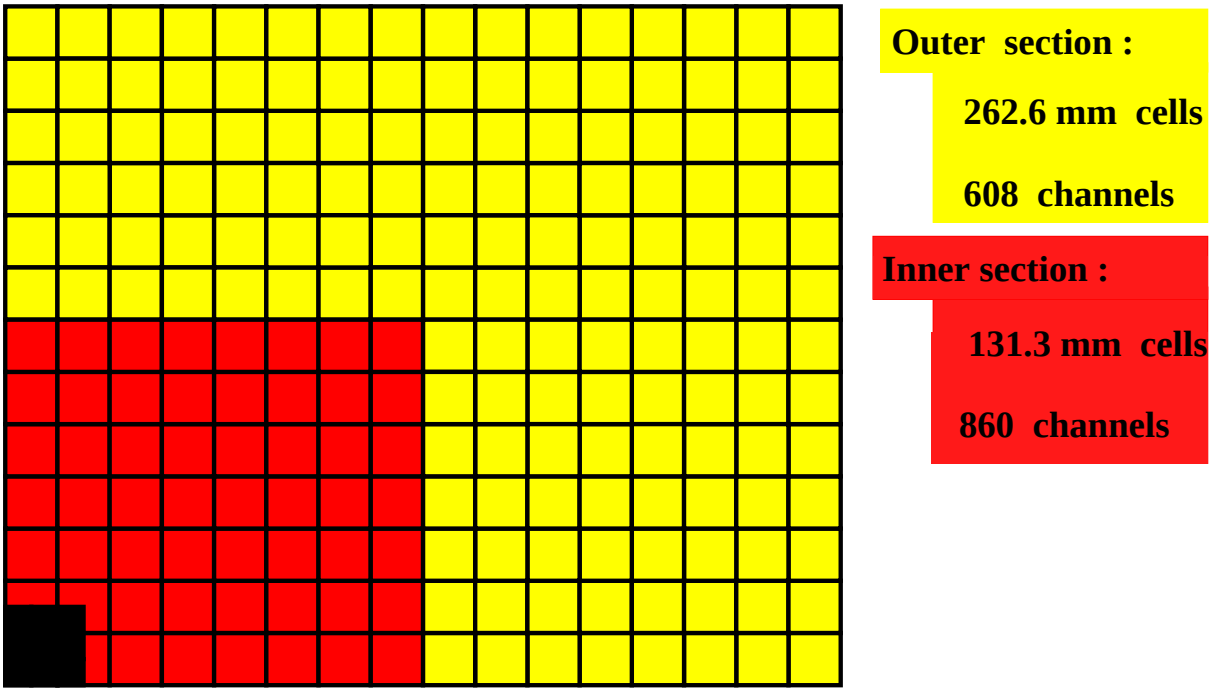

Figure 2.2: *Lateral segmentation of HCAL. One quarter of the detector front face is shown.*

segmentation into two zones has been adopted (see Fig. 2.2), leading to a substantial economy in the number of read out channels.

In order to optimize Level 0 trigger-logic performance, a projective matching of the various detector elements as seen from the interaction point has been implemented [4, 6, 7].

2.3 Detector technologies

The basic technical choices for ECAL and HCAL are driven by the energy resolution performances expected. The trigger requirement can very well be satisfied by sampling calorimeters.

- ECAL : Recent year's developments of the "shashlik" technology [8, 9] have shown that electromagnetic shower energies can be measured with a resolution of $\sigma(E)/E = 10\%/\sqrt{E} \oplus 1.5\%$ (E in GeV), which, together with preshower information, provides sufficient electron/hadron separation at the trigger level as well as at the reconstruction stage. This performance is obtained using a sampling structure of 2 mm lead sheets interspersed with 4 mm thick scintillator plates, and a careful design of the light collection by the wavelength shifting (WLS) fibers. This energy resolution will be a preponderant factor in the mass resolution of B decays containing a π^0 or prompt photon. An appreciable improvement could only be obtained by a different technology such as the use of crystal detector elements. Given the detector area of about 50 m^2, such a choice is a priori beyond the collaboration's resources.

- HCAL : The structure chosen is an iron/scintillating tile calorimeter readout by WLS fibers, the scintillator and iron plates being parallel to the beam. Again, the technique has been extensively studied in the recent years, in particular by the RD34 and ATLAS collaborations at CERN [10]. For LHCb the sampling structure provides on average 4 mm scintillator thickness, every 16 mm of iron. With an overall material thickness of 1.2 m, the energy resolution obtained is: $80\%\sqrt{E} \oplus 10\%$.

- SPD and PS : Given the above choices, it is attractive to adopt scintillators for these two detection planes located just before (SPD) and just after (PS) a 12 mm thick lead wall. The detector elements are 15 mm thick scintillator pads. A groove in the scintillator holds the helicoidal WLS fiber which collects the scintillation light. The light from both WLS fiber ends is sent by long clear fibers to photomultipliers that are located above or below the detector. This structure provides on average about 25 photoelectrons in response to a minimum ionising particle, which enables a clean separation between electron and photon showers.

Table 2.1 summarizes the requirements to the calorimeter sub-detectors.

Table 2.1: *Requirements to the calorimeter sub-detectors.*

sub-detector	SPD/PS	ECAL	HCAL
number of channels	2×5952	5952	1468
overall lateral dimension in x,y	6.2 m×7.6 m	6.3 m×7.8 m	6.8 m×8.4 m
depth in z	180 mm, 2 X_0, 0.1 λ_I	835 mm, 25 X_0, 1.1 λ_I	1655 mm, 5.6 λ_I
basic requirements	20-30 photoelectrons per MIP	$\sigma(E)/E =$ $10\%/\sqrt{E} \oplus 1.5\%$	$\sigma(E)/E =$ $80\%\sqrt{E} \oplus 10\%$
dynamic range	0-100 MIPs 10 bits (PS), 1 bit (SPD)	0-10 GeV E_T 12 bits	0-10 GeV E_T 12 bits

2.4 Photodetectors

The four detectors follow the same basic principle: scintillation light is transmitted to a phototube by wavelength shifting fibers. The single fibers of the SPD and PS can advantageously be read on multianode photomultipliers. The fiber bunches in ECAL and HCAL require individual phototubes. The main differences between the four systems are their light yields and dynamic ranges. The SPD has to distinguish clearly a minimum ionising particle, which generates only about 25 photoelectrons. It will be useful to get sensitivity to a MIP in the preshower, but in order to correct the energy measurements in ECAL, its dynamic range must extend up to 100 MIPs, requiring digitisation over 10 bits. This large range imposes stringent limits on pixel to pixel cross-talk.

The highest electron or photon energies to be detected in ECAL are about 200 GeV. On the other hand, the reconstruction of low energy π^0 requires digitisation sensitivity to a few 10 MeV. This is due to the broad range of B longitudinal momentum. However, the transverse momentum spectra of electrons, photons and π^0's are roughly constant as function of the production angle. The typical transverse momenta being of the order of the B mass. It is therefore intended to adapt the gain of the phototubes in inverse proportion to their radial position, in order to have a constant E_T scale. Excellent linearity will be a strong requirement, as well as gain stability. The fiber bunch should be seen with constant efficiency. Even using a light mixer, this requires a good photocathode uniformity. As discussed in the next paragraph, the phototubes will have to be fast enough.

The same type of criteria apply to HCAL, and it will obviously be an advantage to use the same photomultipliers in both detectors. The energy ranges to be detected are typically the same. However, the HCAL structure delivers only 50 photoelectrons per GeV, a factor 15-20 less than ECAL. HCAL tubes will therefore operate at higher gain.

2.5 Front-end electronics

The basic structure is dictated by the need to handle the data for Level 0 trigger as quickly as possible. The front-end electronics and the SPD/PS photomultipliers are located at the detector periphery. The signals are shaped directly on the back of the photomultiplier (for PS/SPD) or after 10 m long cables (for ECAL/HCAL). They are then digitized in crates positioned on top of the detectors, and the trigger circuits hosted in the same crates can perform the clustering operations [11]. For each channel, the data, sampled at the bunch crossing rate of 40 MHz, are stored in a digital pipeline waiting for the Level 0 trigger decision.

In order to exploit the intrinsic calorimeter resolution over the full dynamic range, ECAL and HCAL signals are digitised by a 12 bit flash ADC [12]. 10 bits are enough for the preshower, and the SPD information is only one bit, a simple discriminator telling whether a cell has been hit [13, 14].

The second requirement is to reduce the signal tails associated to the bunch crossing preceding the one being sampled. For ECAL and HCAL, this goal can be achieved at the percent level by suitable signal treatment within 25 ns. In the case of preshower and SPD, the signal shape fluctuations require to maximise the signal integration time. They therefore have a different front-end design of the integrator.

The next essential point is that, in order not to deteriorate the resolution, the electronic noise must remain at the least significant bit level [15]. At the short shaping times being used, this requires careful design of the very front-end part.

2.6 Calibration

A pre-calibration of all calorimeter components at the level of approximately 10% is foreseen before calibrating to a higher accuracy. This task is performed by dedicated calibration systems on each sub detector that are described in chapter 5.

The ultimate calibration accuracy should be of the order of a percent. This will be obtained off line with high statistics data, the absolute value being obtained from physics signals such as the π^0 mass or electrons of known momentum [16]. The relative calibration and stability of the channels must be permanently controlled during data taking to guarantee the trigger operation. Dedicated devices will be implemented to that effect.

Chapter 3 Prototype Performance and Simulation Results

3.1 The pad/preshower detector

3.1.1 Introduction

In order to optimize the basic design of the scintillator pad/preshower (SPD/PS) detector, various prototypes have been tested in particle beams [17], and the detector performances have been compared with Monte Carlo simulations [3].

The special requirements to the SPD/PS system are a relatively large number of scintillating pads ($\approx$12000) that have to be readout in a fast, compact and cost effective way. A very compact readout system can be achieved by using a multi-anode photomultiplier tube (MAPMT) with 64 channels, that would allow to readout the $\approx$12000 channels with only $\approx$200 photomultiplier tubes. However, the choice of MAPMTs with pixel sizes of 2×2 mm^2 has a strong implication on the design of the SPD/PS optical system. Due to the very small area that is available for coupling the readout fibers to the photomultiplier tube, the light transmission from each scintillator pad to the MAPMT has to be performed by one single fiber. In order to optimize the light collection efficiency and the readout time for such a design, different techniques for coupling a single fiber to a scintillator pad have been studied, and numerous prototypes have been tested in the beam.

The SPD/PS system is made from a lead converter plate that is sandwiched between two layers of scintillator pads. The lead converter thickness was optimized by simulation studies and the performance of the final system was verified in the beam by testing a SPD/PS prototype together with the electromagnetic and hadronic calorimeter prototypes in a combined test.

3.1.2 Optimization of the light-collection efficiency

The light-collection efficiency of the SPD/PS system depends on several parameters that have been tuned for an optimal performance. The different variants of coupling the fiber to the scintillator pad, the choice of the scintillator material and its thickness, the influence of the wrapping material, and the effect of different fiber types have been measured in detail [17]. In the following we discuss the parameters that have been optimized, and the choice of the basic design that arise from the various measurements.

Two different techniques of coupling the fiber to the scintillator pad have been evaluated and are illustrated in Figure 3.1. In the so called "DEEP" groove option the WLS

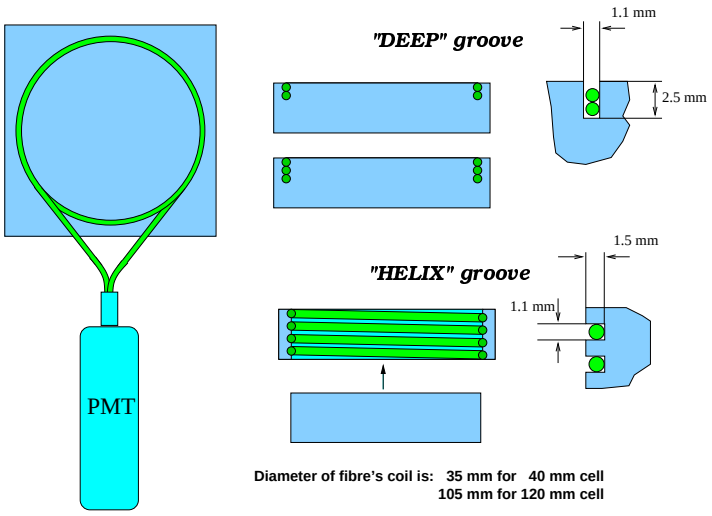

Figure 3.1: *Design of preshower prototypes.*

fiber coils in several (2-4) turns in a groove of rectangular cross section that is machined into the large side of a scintillator pad. In the more complex "HELIX" option the scintillator is split into two parts by cutting out from the scintillator pad a central cylindrical piece that serves as a plug once the outer part has been equipped with the fiber. The fiber runs in a groove that is milled on the inner surface of the outer part. For better contact, optical grease (BC-630) or glue (BC-600) is applied between the fiber and the scintillator. These two design approaches were compared for various cell dimensions and thickness, for different number of fiber turns, and for different types of scintillator material. A detailed comparison of all measurements [17] shows that there is no significant difference in the light collection between the two options of design. We choose the "DEEP" groove option for the final design since it is simpler and cheaper to machine, to assemble and to glue. Moreover, it has been shown [17] that the uniformity of response to a minimum ionizing particle in the groove region was found to be better in this design. The global variation in light yield over the pad surface of a 120×120 mm^2 cell is 2-3% and better for smaller cell sizes.

The light yield for two different types of scintillator material was studied, comparing PolyVinylToluene (PVT) plastic from BICRON (BC-408) and cast polystyrene (PS) scintillator produced in Russia. The PVT scintillator BC-408 gives $\approx$1.6 times more light than conventional polystyrene scintillator. However, polystyrene scintillator is more economic and simpler to machine. Our experience with machining of BC408 shows that even careful milling of the groove can produce defects on the polished surface. In order to compensate for the reduced light yield of polystyrene, a 15 mm thick scintillator pad can be used instead of 10 mm. The measurements indeed confirm that the light yield is proportional to the pad thickness and that the light output for a 15 mm thick PS scintillator is comparable to the one of a 10 mm thick BC-408 scintillator. Therefore we keep PS scintillator as the base-line solution, compensating the lower light yield by the increased thickness.

In order to determine the optimal length of the fiber that is coiled inside the pad, two

effects have to be taken into account. The length of the fiber coupled to the scintillator increases the signal duration by ≈5 nsec/m. Since the SPD/PS detector has to be readout in 25 ns, the fiber length is constrained. On the other hand, one expects the light collection efficiency to increase with the fiber length that is in contact with the scintillator. However, the measurements have shown that due to the short attenuation length of ≈50-100 cm in a bent fiber, the light collection efficiency is not proportional to the fiber length and even comes down for large number of coils. In conclusion, in the final design 3.5 fiber turns have been chosen as close to the optimal value. For the same number of fiber coils the ratio of light yield is ≈2:3 when comparing a 12 cm×12 cm cell with a 4 cm×4 cm cell.

Other properties like mechanical durability, radiation hardness and fast response are also important for the choice of the fiber type. A comparison of Y11 and BCF91A multi-clad fibers has shown that Y11(250) double-clad S-type fiber from KURARAY [18] and BCF91A from BICRON [19] give about the same light yield, but that the Y11 S-type has better mechanical properties [20]. The BCF91A fiber has less mechanical stability against bending at small radius. Also, from a comparative study it has been shown [21] that the signal from Y11(250) MC is faster than from BCF91A fibers, and that it fulfills the timing requirements. The effect of grease or glue as an optical coupling between the Y11(250) MC fiber and the scintillator was also studied. The measurements show that the BC-600 glue and the BC-630 grease both improve the light collection by ≈30%.

Another important parameter that influences the light collection efficiency is the reflectivity of the scintillator surface. Different techniques to enhance the reflectivity have been studied: wraping the entire pad with white TYVEK paper, chemical treatment of the surface with the so-called DMA method, and aluminizing the lateral sides of a pad. It was concluded that the light collection in the case of chemically treated scintillator surfaces (DMA) does not differ from TYVEK wrapping in case of 40×40 mm^2 pads, while in case of large cells the light collection is better with TYVEK by ≈30%. It could be advantageous to treat the edges of the pads with the DMA method or to aluminize them, since both methods reduce the amount of non-active material between cells as compared to wrapping with TYVEK paper. However it was measured that for aluminized lateral sides the light yield is reduced by $20 - 50\%$ as compared to TYVEK wrapping. In conclusion, wrapping all scintillator pads with TYVEK is the preferred baseline solution.

The performance of the final design of a 4 cm×4 cm×15 mm pad that is made out of polystyrene scintillator is shown in Fig. 3.2. The 1 mm diameter Y11(250)MC S-type fiber is coiled with 3.5 turns and glued to the scintillator according to the "DEEP" groove design. The fiber is coupled to a photomultiplier with 15% quantum efficiency. The typical light yield from 50 GeV electrons, that act like MIPs in the scintillator, was measured to be ≈105 photoelectrons at the peak of the distribution.

3.1.3 Optimization of the lead-converter thickness

The electron/pion separation is based on the fact that electrons produce a shower that starts in the lead absorber with a bulk of secondary particles leaving the lead and reaching the scintillator of the PS, thus inducing a signal that is much larger than a typical signal from a minimum ionizing hadron. On one hand the absorber thickness should be large to generate a big number of secondary particles and on the other hand it should be thin

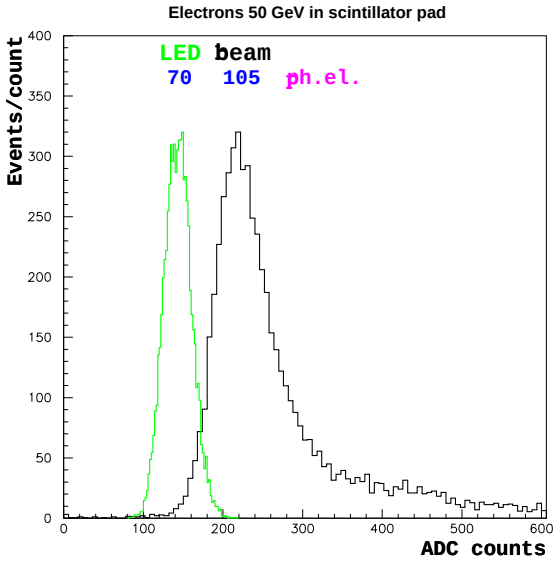

Figure 3.2: *The signal from 50 GeV electrons (acting as MIPs) in a polystyrene scintillator pad of 4 cm×4 cm×15 mm size, that is read-out by 3.5 turns of 1 mm diameter Y11(250)MC S-type fiber, glued according to the "DEEP" groove design and coupled to a photomultiplier with 15% quantum efficiency, is shown. The pedestal is subtracted. The comparison with a LED signal gives ≈105 photoelectrons at the peak.*

to minimize the invisible energy that is lost in the absorber material and that cannot be detected by the ECAL. Some correction can be applied by estimating the energy that has been lost in the absorber through the measurement of the energy that has been deposited in the PS scintillator. In order to optimize the absorber thickness we studied with a stand-alone GEANT3 [22] based simulation program its effect on the main detector performances [3].

The energy that is deposited in the lead absorber has been simulated for electrons with energies of 1 to 50 GeV for various absorber thickness of 1.5 to 3.0 radiation lengths. In order to estimate the error on the energy measurement by the ECAL due to the loss of energy in the absorber, the standard deviation of the energy deposited in the absorber divided by the energy of the incoming electron is shown on the left plot of Figure 3.3 for various absorber thickness. The values should be compared to the design resolution of an ECAL module of $\sigma(E)/E = 10\%/\sqrt{E} \oplus 1\%$. A thickness of 3 X_0 of lead would change the resolution to $\approx 12\%/\sqrt{E}$, if no correction is applied.

In order to apply a correction to the missing energy in ECAL one can estimate the amount of energy that is lost in the absorber by measuring the energy that is deposited in the PS scintillator material. Figure 3.4 shows the correlation between the energy lost in the absorber and the signal of the PS, that can be approximated by a linear function. The resulting error on the ECAL resolution as function of the absorber thickness after correction with the PS signal is shown in the right plot of Figure 3.3. To illustrate more clearly how the PS correction effects the ECAL resolution, an idealistic electromagnetic

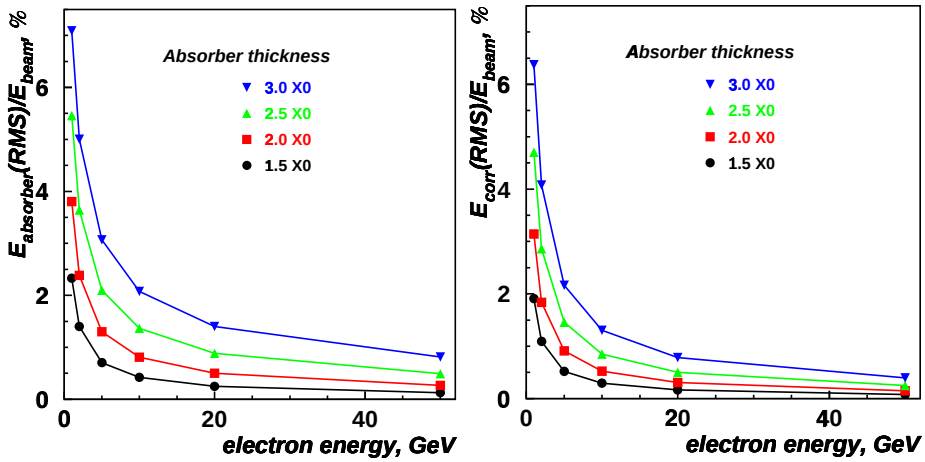

Figure 3.3: *Simulation of the energy lost in lead by electrons of* $1 - 50$ *GeV. On the left plot the relative error on the energy measurement is shown. This should be compared with the design ECAL module resolution of* $10\%/\sqrt{E} \oplus 1\%$. *For the larger thickness values of 2.5-3* X_0 *the effect becomes non negligible. On the right plot is shown the resulting error to the ECAL energy resolution after correction of energy losses in the absorber with the PS signal.*

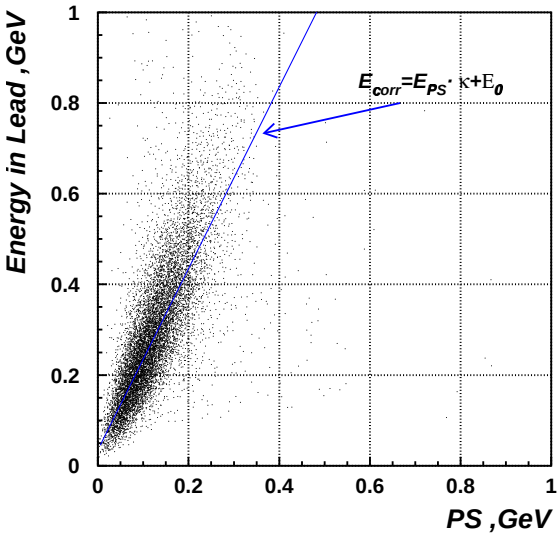

Figure 3.4: *Energy of the electromagnetic shower lost in the lead absorber plotted versus the PS signal. The correlation is approximated by a linear function and is used for correcting the missing energy in ECAL.*

calorimeter with an energy resolution of $2.5\%/\sqrt{E}$ placed behind the PS detector with a 2 X_0 lead absorber, has been included in the simulation. As can be seen from Fig. 3.5 the resolution of the idealistic ECAL is practically recovered at energies above 5-10 GeV after correcting for the energy that is absorbed in the lead of 2 X_0, and the overall effect from the 2 X_0 absorber is not significant with respect to the ECAL design energy resolution of $10\%/\sqrt{E}$.

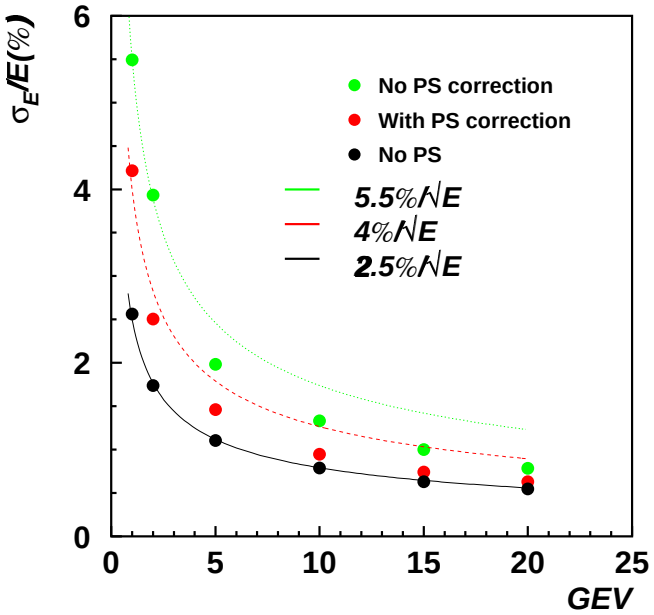

Figure 3.5: *Effect of the lead converter on the resolution of an idealistic ECAL, with and without correcting for the absorbed energy (see text).*

The performance of the preshower system to separate between electrons and pions is expected to improve by increasing the lead absorber thickness. Figure 3.6 shows the pion versus electron rejection of the PS system as function of various absorber thickness for two different energies of the incoming particle. The curves have been obtained by adjusting the threshold on the number of minimum ionizing particles that are detected in the PS scintillator to the energy of the incoming particle, since this improves somewhat the separation capability for particle energies below 10 GeV. It can be seen that the pion rejection factor decreases by about 20% when reducing the absorber thickness from 3 to 2 X_0, for a constant electron inefficiency of 10%.

Energy loss in inactive material between the preshower scintillator and the beginning of the electromagnetic calorimeter could also contribute to performance degradation of ECAL. However, it can be shown [3] that by suitably adjusting the κ-coefficient (see equation in Fig. 3.4) this effect can be compensated without inducing any degradation in ECAL energy resolution.

As baseline solution we have chosen a lead absorber thickness of two radiation lengths for the PS system that allows an efficient e/π separation without compromising the energy resolution of the electromagnetic calorimeter.

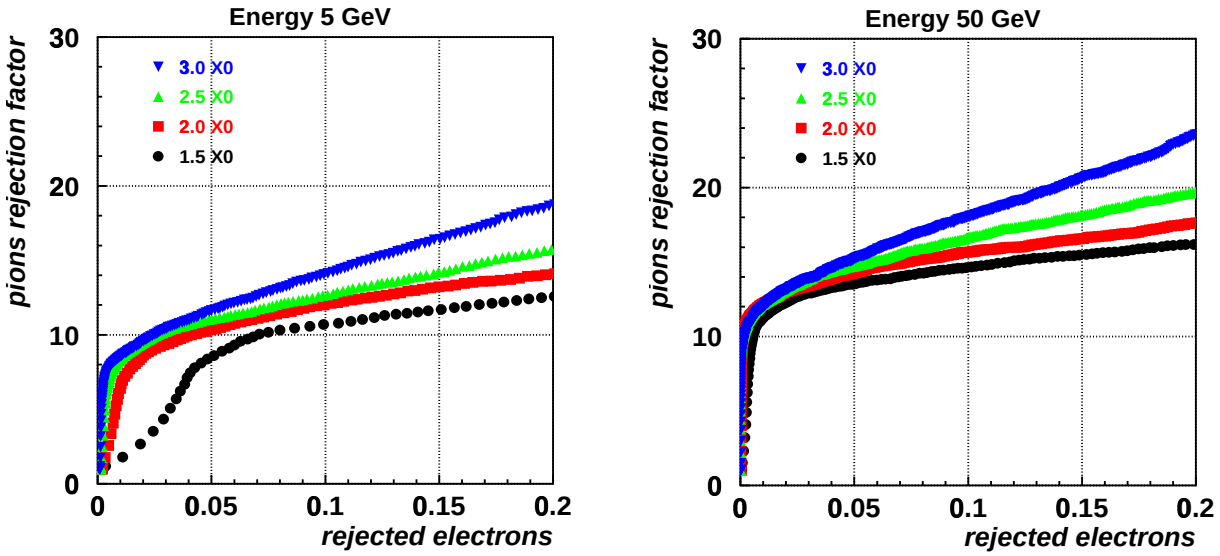

Figure 3.6: *The pion versus electron rejection of the PS system as function of various absorber thickness for two different energies of the incoming particle.*

3.1.4 Performance of the basic design

In order to study technological issues and to test the SPD/PS detector performance in a combined test together with the ECAL and HCAL prototypes, two matrix prototypes were built that consist of a 3×3 inner matrix of 4×4 cm^2 cells and eight surrounding cells of 12×12 cm^2 size, packed in a light-tight black box. The thickness of the box wall was 250 μm that is close to the final design requirements. The two boxes differ from each other just by the thickness and type of the scintillator: 10 mm thick BC-408 scintillator (BICRON) and 15 mm thick polystyrene based cast scintillator (Russia). From the results described in section 3.1.2 about the same light response is expected from both prototypes. Between the first SPD box and the second PS box 1 cm of lead converter material was inserted. The Scintillator pads were wrapped with 150 μm thick TYVEK paper and readout by WLS Y11(250) multi-clad S-type fiber of 1 mm diameter coiled in a "DEEP" groove with 3.5 turns. The fiber was glued into the scintillator by BC-600 optical glue (BICRON). Each end of the WLS fiber was coupled to a 1 mm diameter clear fiber (KURARAY) by an individual optical connector. The length of the clear fibers was 3 meters. The bundle of 34 fibers from each module box was packed into a light-tight black pipe. The other ends of the clear fibers were connected to a 64-anode PMT (R-5900, HAMAMATSU [23]) by means of an optical coupler made of plastic with 64 pairs of drilled holes. The two fiber ends of each cell were connected to the corresponding pixel of the PMT in such a way that they were aligned on the pixel diagonal. The fiber ends were tightly inserted (without glue) into the individual holes and pressed to the cathode window without any grease coupling. The coupler was visually positioned using marks on the PMT that are supplied by the manufacturer. The precision of the coupler alignment with respect to the PMT pixels was ≈0.2 mm.

The response of the scintillator pad detector (SPD) in front of the lead converter to

minimum ionizing particles (MIPs) was measured and compared to the results obtained in section 3.1.2. The light collected for MIPs was estimated with a reference LED as ≈20 photoelectrons for 120×120 mm^2 cells and ≈30 photoelectrons for 40×40 mm^2 ones. The big discrepancy between the previously obtained 105 photoelectrons and the measured 30 photoelectrons can be explained by the following effects. The light losses in the optical connectors are estimated to contribute with a factor ≈0.87±0.03 [24]. We did not do any systematic study of the light losses for the single-fiber connectors used in this test, since we intend to use multi-fiber type connectors in the future design [6]. The light leakage to the neighboring pixels of the MAPMT causes a reduction factor of about 0.8±0.05. This number is expected to improve, as discussed below. The difference in photo-cathode sensitivity at 500 nm for the FEU-85 tube (used in the previous test) and the MAPMT R5900 gives a factor of ≈0.75±0.03. The light attenuation for 3 m of the clear PSM-type fiber [18] corresponds to a factor ≈0.71 at 500 nm, and no clear fiber had been used in the previous test. The anode non-uniformity of ≈12 % for the MAPMT gives an additional uncertainty. The final factor of 0.37 ± 0.05 does not yet include additional losses that are expected from the optical coupler to the PMT, since for practical reasons the coupler was not glued to the fibers so that it could be reused for different prototypes.

A certain amount of cross talk between individual cells is expected due to light leakage from one fiber to a neighboring pixel of the MAPMT, if the fiber to pixel coupling is not ideal. Light that leaves the fiber end with a certain angle to the fiber axis has a chance to propagate along the PMT window and to generate a signal in the neighboring pixel. The amount of such light leakage depends on the precision of the fiber-to-pixel coupling, the distance from the fiber end to the PMT window, and of the thickness of the glass window. The design of the coupler used in the tests was based on a precise matrix of holes drilled in a plastic holder. The light cross talk between cells was determined from the prototype by illuminating one fiber with a blue LED and by measuring the signal on the corresponding pixel and its neighbors. About 20 to 25% of the light emitted by the fiber is shared among the eight neighbors, while no light leakage is seen for pixels that are further away. The photo-statistical fluctuations of the signal that is leaking to the neighboring pixels has no visible correlation with the signal from the central pixel. This fact points out that the cross talk takes place before the multiplication process has started. It was also observed that the average value of the cross talk does not depend on the signal amplitude. Part of the large cross talk results from misalignment of the fiber-to-pixel positioning. An improvement is expected by better positioning the coupler on the PMT window and by controlling the air gap between the fiber and the glass. Further studies to optimize the fiber-to-PMT coupling are foreseen in 2001.

The e/π separation performance of the PS prototype was measured in the X7 test beam at the SPS at CERN with electrons and pions between 10 and 50 GeV/c momentum. The energy deposited in the PS for 50 GeV/c electrons and pions is shown in Fig.3.7. For a threshold of ≈180 ADC counts, that corresponds to 9 MIPs, a pion rejection of 92% is achieved while retaining 95% of the electrons. For 10 GeV/c particles the same e/π separation performance is achieved for a threshold of ≈100 ADC counts (5 MIPS). This performance can be obtained at the trigger level by cutting on the energy that is deposited in the PS detector with a p_T dependent threshold that is set as function of theta. An improved e/π separation can be obtained in the offline analysis if the information from the

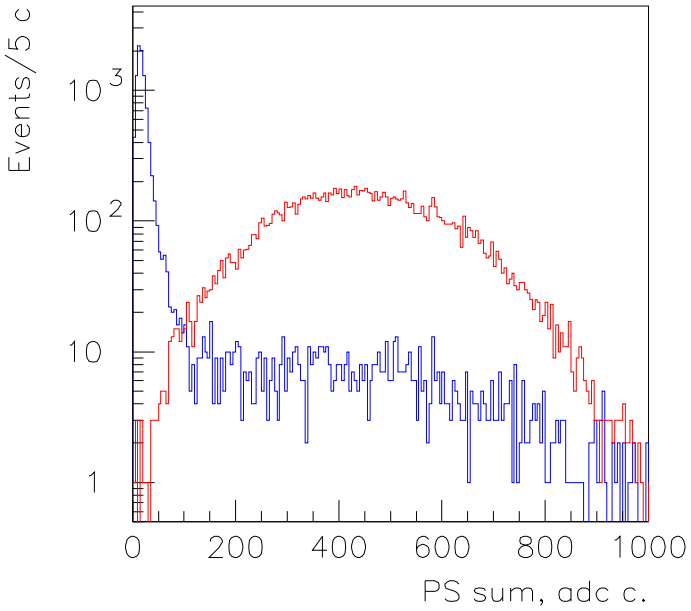

Figure 3.7: *Energy deposition of 50 GeV electrons and pions in the preshower detector.*

ECAL and the momentum of the incoming particle is used in addition to the PS signal. The measurements show that with a threshold of 4 MIPs a pion rejection of 99.6%, 99.6% and 99.7% with an electron retention of 91%, 92% and 97% are achieved for 10 GeV, 20 GeV and 50 GeV particle momentum, respectively.

From measurements with 20 GeV electrons in the combined PS and ECAL test, it is confirmed that the energy resolution of the ECAL does not deteriorate if one corrects for the energy that has been absorbed in the PS lead converter by the energy that has been measured in the PS scintillator [17].

In order to separate photons and electrons at the Level-0 of the ECAL trigger, the scintillator pad detector (SPD) is positioned in front of the lead absorber. Charged particles will deposit energy in the scintillator material while neutrals should not interact. Some processes however can cause a photon to deposit indirectly energy in the scintillator which leads to a miss identification of the photon as an electron. Possible sources are pair production before the SPD due to material from other detector components in front of it, interactions in the scintillator of the SPD that produce charged particles inside the SPD, and backwards moving charged particles (back splash) that are generated in the lead absorber or in the electromagnetic calorimeter. The latter two effects have been studied with the prototype in a tagged photon beam in X7 and compared with simulation (see Figure 3.8). The detailed measurements for photon energies between 20 and 50 GeV show [25] that the probability of photon missidentification due to interactions in the SPD scintillator is (0.8±0.3)%, when applying a threshold of 0.7 MIPs that does not reject any electrons. The probability to pass this threshold due to backwards moving charged particles was measured to be (0.9±0.6)% and (1.4±0.6)% for 20 and 50 GeV photons, respectively. All numbers are in very good agreement with a detailed Monte Carlo simulation study [25].

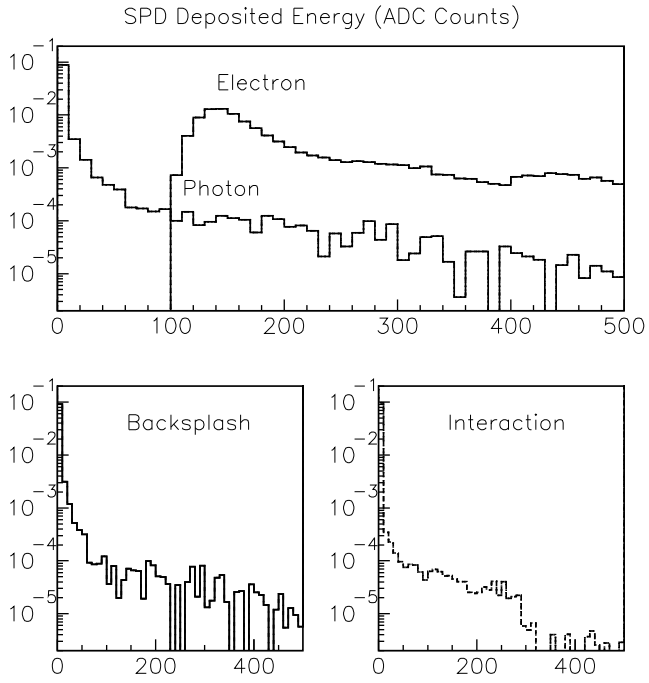

Figure 3.8: *Normalized distribution from test-beam data of deposited energies in the SPD by electrons and 46-48 GeV photons (top), by these photons through backsplash (bottom-left) and by photons through interaction with the SPD (bottom-right). The first bin corresponds to photons with no energy deposition.*

3.1.5 Radiation hardness

The radiation environment of the preshower detector is 2-3 times lower than in the electromagnetic calorimeter, since it does not suffer from the longitudinally growing dose due to the developing electromagnetic shower. Both systems contain essentially the same materials, so one can conclude from the measurements on radiation resistance performed for the ECAL (see sec 3.2.4) that no significant degradation of the PS response is expected over 10 years of operation. In case of an extreme irradiation the very inner part of the detector could be easily replaced, as it is foreseen by the mechanical design [6]. Nevertheless, some additional tests of the radiation hardness of fibers that are bent and glued in the polystyrene scintillator will be undertaken by the end of 2001.

3.2 The electromagnetic calorimeter

3.2.1 Introduction

The requirements to the electromagnetic calorimeter for LHCb are good energy resolution, variable transverse granularity, fast response time, and good reliability in a radiation hostile environment. The experience from other experiments has shown [26, 27, 28] that the "shashlik" technology can combine these features at a reasonable cost. The energy resolution of the HERA-B calorimeter modules with similar design to the LHCb modules was measured with an electron beam [29] to be

$$\frac{\sigma_E}{E} = \frac{9.5\%}{\sqrt{E}} \oplus 1\% \quad (E \text{ in GeV}) \,, \tag{3.1}$$

which satisfies the design energy resolution of the LHCb calorimeter.

Various simulation studies and beam tests with "shashlik" prototypes were undertaken in order to optimize the design of a module for a good transverse uniformity in the response at a reduced cost, and to verify the performance of the fast optical components for radiation levels that are expected at LHC.

For a given cell size and sampling fraction the energy resolution of a module, and to some extent the spatial resolution, are determined by the uniformity in response. The transverse uniformity of a "shashlik" module is depending on two dominant effects, the light reflection efficiency from the edges of each tile (the so-called global uniformity), and the position and density of fibers with respect to the ionising particles (the local or inter-fiber uniformity). The tile edge coverage and the fiber density have been optimized by measuring the uniformity in response of various prototypes and by comparing the results with detailed simulation studies [30]. Furthermore, the transverse and longitudinal uniformity in response can also be affected by radiation damage of the scintillator and fiber material. We measured the degradation in light yield of the scintillator tiles and fibers due to radiation, and we simulated the effect of such degradation on the energy resolution of the ECAL modules [31].

3.2.2 Optimization of the tile-edge coverage

In order to choose the tile-edge coverage that provides the best light reflection efficiency, $\approx 5{\times}5$ cm^2 tiles with blackened, aluminized and white painted edges were studied, by comparing their response to a ^{90}Sr source that was positioned at the tile center and close to the tile edge. The light was read out via fibers that penetrate the tile similarly to the final module design [4]. For tiles that were treated with three different techniques on their edges, the table 3.1 shows the response to the radioactive source at the tile center and the difference in response between the center and the edge, thus comparing the global non-uniformity and the corresponding degradation of the mean light path that is induced by the tile-edge reflection inefficiency. These results agree well with Monte Carlo simulations that predict 2, 5 and 7 cm mean light path for black, aluminized and white tile edges, respectively.

For the final design the white paint will be replaced by another technique that also produces a diffuse reflecting surface, by treating chemically the edge surface with the

Table 3.1: *The global non-uniformity that is induced by the tile-edge reflection inefficiency. Shown are the response to a ^{90}Sr source at the tile center and the difference in response between the center and the edge of the tile for blackened, aluminized and white painted edges. Measured was the PM current depending on the source position over the tile surface.*

edge coverage type	response at tile center, $[nA]$	center-edge difference, [%]
blackened	48	19
aluminized	112	7
white diffused (BC-622A)	134	4

so-called DMA method. It has been shown that the chemical treatment has an increased reflection efficiency and is more cost effective as compared to the white paint.

3.2.3 Optimization of the fiber density

Dedicated simulation studies of light propagation in the scintillator tile with wavelength-shifting fiber readout illustrate the interplay between the tile transparency and the fiber density on the local uniformity of response. Table 3.2 shows the local uniformity that has been obtained from simulation of a $\approx 12\times12$ cm^2 scintillator tile with three different fiber densities of 144, 100 and 64 fibers per tile, and three different mean light paths of $\lambda_{Sci} = 15$ cm, 25 cm and 50 cm. The overall uniformity over the whole tile has been parameterized by the following function:

$$f(x) = a \times \left[1 - A_{global} \cdot \left(\frac{x - x_0}{l_0/2}\right)^2\right] \times \left[1 - A_{local} \cdot \cos\left\{\frac{2\pi}{d} \cdot (x - x_0)\right\}\right] \qquad (3.2)$$

where x_0 is the center of the cell, l_0 the cell size, d the inter-fiber distance, a a normalization factor, and A_{global} and A_{local} are the values that determine the global and local non-uniformity, respectively. As expected, both an increased fiber density and an increased mean light path improve the local uniformity of response.

Table 3.2: *Scintillator transparency and fiber density impact on the local uniformity of the response to MIPs, as studied with Monte Carlo. Shown is the value of the A_{local} coefficient from the parameterization in eq. 3.2. Options with* 144, 100 *and* 64 *fibers per module, and $\lambda_{Sci} = 15$ cm, 25 cm and 50 cm are considered.*

	Fibers per tile		
Mean light path, λ_{Sci}	144	100	64
15 *cm*	0.0035(5)	0.0091(4)	0.0132(3)
25 *cm*	0.0005(5)	0.0051(4)	0.0089(3)
50 *cm*	0.0004(4)	0.0022(3)	0.0063(3)

Table 3.3: *Response non-uniformity of modules with* 144, 100 *and* 64 *fibers per module, as measured with MIP and electron beams. Global and local non-uniformity effects are expressed in terms of* A_{global} *and* A_{local} *coefficients from the parameterization in eq. 3.2 correspondingly. Implied is the integration over the effect along the y-direction.*

	144 fibers	100 fibers	64 fibers
MIP beam			
light yield, $[a.u.]$	1.20	1.00	0.74
global non-uniformity, A_{global}	0.06(1)	0.03(1)	0.01(1)
local non-uniformity, A_{local}	0.004(1)	0.009(1)	0.012(1)
e^- beam			
light yield, $[a.u.]$	1.27	1.00	0.70
global non-uniformity, A_{global}	0.03(1)	0.02(1)	0.02(1)
local non-uniformity, A_{local}	0.003(1)	0.005(1)	0.007(1)

However, the fiber density does not only influence the local but also the global uniformity, as can be seen from measurements of $\approx 12\times12$ cm^2 big "shashlik" modules with different fiber densities of 144, 100 and 64 fibers per module, that have been tested with minimum ionising particles (MIPs) and 50 GeV electrons at the CERN X7 SPS test beam. The results are summarized in Table 3.3 and show, that the local uniformity improves with growing fiber density, while the global uniformity degrades. The effect on the global uniformity can be understood by the fact that the reflective edges are screened from the light that is produced in the center of the tile by the fibers that are penetrating the tile. Therefore there must be a compromise in the choice of the fiber density for improving the local uniformity without degrading too much the global uniformity.

The results obtained for the local uniformity with MIPs is in very good agreement with the simulation results given in table 3.2, for a mean light path of $\lambda_{Sci} = 15$ cm. Figure 3.9 shows the local uniformity as function of the fiber density, measured with 50 GeV electrons that enter the ECAL modules perpendicular to their front surface. The value of 0.7% that is obtained for 64 fibers per module becomes comparable with the design value for the constant term of 0.8% of the ECAL energy resolution. However, the effect of non-uniformity and in particular of the local non-uniformity is expected to be strongly smeared when particles penetrate at an angle that is not exactly perpendicular to the calorimeter front surface. Simulation studies show that the local uniformity is improving by a factor of three for angles that are typical for particles entering the calorimeter in the outer section of the detector.

Taking into account these results, and in view of reducing the size of the fiber bundle as well as the cost of the detector, we have chosen as baseline design a fiber density of 144 fibers per inner- and middle-section module and 64 fibers for the outer-section module. The reduction from 144 to 64 fibers leads to a smaller sized fiber bundle for the outer-section module and thus moderates the requirements to the photocathode uniformity of the PMT. This is not an issue for the middle- and inner-section modules with 144 fibers, since they contain several cells which brings the number of fibers per tube to 16 and 36

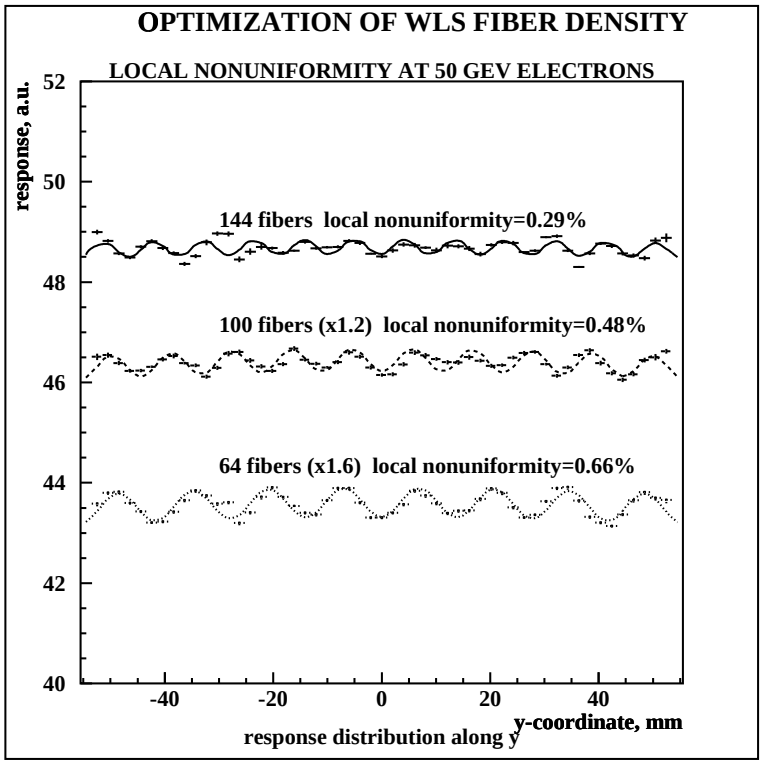

Figure 3.9: *The local uniformity measured for three modules with* 64, 100 *and* 144 *fibers per module correspondingly, with* 50 *GeV electrons at X*7 *beam at CERN. Global type uniformity corrections are taken into account on the plot. The curves are the results of the fit.*

fibers, respectively.

3.2.4 Detector performance under irradiation

We performed detailed measurements and simulation studies in order to determine the degradation of the ECAL resolution due to radiation damage of the optical components of the "shashlik" module [31], when operated under LHC conditions.

The expected annual radiation dose at the shower maximum for the ECAL modules closest to the beam pipe is 0.25 Mrad, assuming a luminosity of 2×10^{32} cm^{-2}s^{-1} and 10^7 s per nominal year. As can be seen from the left plot of Figure 3.10, the dose is a steep function of the distance from the beam pipe, and varies over the active calorimeter surface by two orders of magnitude. The longitudinal dose profile for the innermost cell is plotted on the right plot of Figure 3.10, where the contributions from the electromagnetic and hadronic components of the shower are shown separately. The radiation mostly affects a relatively small part of the calorimeter in the vicinity of the shower maximum. The middle and outer section modules do not suffer from such a high radiation, where the maximum dose reaches only about 0.02 Mrad per year of LHCb operation. The radiation doses are obtained by summing energy releases calculated with the LHCb GEANT3 based

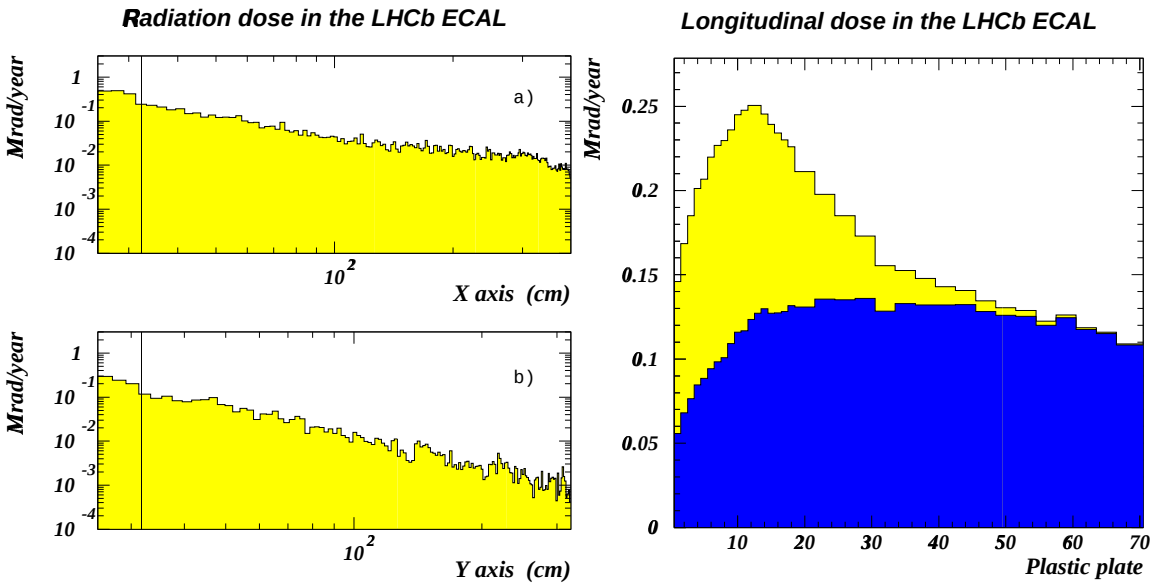

Figure 3.10: *Left plot: the expected annual radiation dose distribution along the x-axis at y=0 (a) and along the y-axis at x=0 (b). The vertical lines indicate the innermost position of the active calorimeter volume. Right plot: The longitudinal dose profile for the innermost module. The contributions from the electromagnetic (grey) and hadronic (black) components of the shower are shown separately.*

SICB simulation program, that uses the GEISHA package. This simulation is in good agreement with a MARS calculation [32] that was done in one xy-plane at the z-position between ECAL and HCAL.

The radiation can affect the quality of the optical components made of plastic materials, namely the scintillating tiles and the WLS fibers. Both, light yield and transmission through the tiles and fibers may decrease with increasing dose. We have irradiated at the LEP Injector Linac (LIL) at CERN the optical components that we foresee to use in the inner section ECAL modules, namely 40×40 mm^2 scintillating tiles made of PSM-115 plastic and Y11-200(MS) fibers from KURARAY, with electrons of 500 MeV energy. In view of the low energy, and in order to obtain a longitudinal dose profile as close as possible to the one expected under LHC running conditions, special modules were formed consisting of 20 layers of 6 mm thick lead plates and 4 mm thick scintillating tiles. These modules were irradiated with approximately 10 rad/s to a total dose of 5 Mrad at the shower maximum. This should be compared to an expected rate of 0.05 rad/s and a maximum dose of 2.5 Mrad over 10 years of LHCb operation.

The left plot of Figure 3.11 shows the measured degradation in light yield and transmission for irradiated scintillating tiles (that are readout with non-irradiated fibers) as function of the distance to the phtomultiplier tube. In order to study the effect of annealing, the measurements were repeated several times between 7 hours and 2000 hours after the irradiation was stopped. One can clearly see that some annealing effect is seen up to 50 hours after irradiation. On the right plot of Figure 3.11 is shown the degradation of the WLS fibers as function of the distance to the phtomultiplier tube, again repeating

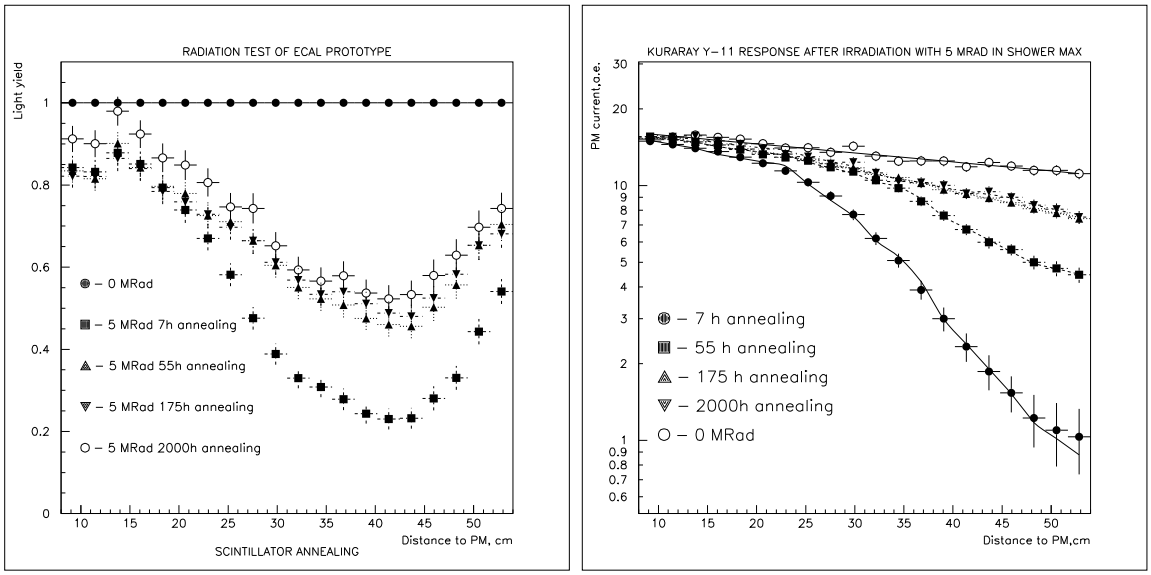

Figure 3.11: *Scintillator (left) and WLS fiber (right) degradation and annealing effect after irradiation at LIL up to 5 Mrad dose at the shower maximum (the shower maximum position corresponds to distance to PMT of 42 cm). Shown is the light yield (scintillator) and PMT current (fibers) vs. the distance to the PMT, that has been repeatedly measured after the irradiation was terminated.*

the measurements several times after irradiation. The subsequent annealing improves the light attenuation by up to 40% and 70% within the first 50 hours and 175 hours, respectively. No further improvement is observed afterwards.

In order to determine the performance degradation of the ECAL module due to the observed degradation of the optical components, a detailed simulation study was performed. The energy response of an ECAL module was simulated using the expected longitudinal dose profile (Fig. 3.10) and the measured degradation of the scintillating tiles and WLS fibers according to Figure 3.11. Three effects on the module performance are shown separately in Figure 3.12. The so-called peak damage is the loss of light collection efficiency of a module due to radiation damage, that amounts to $\approx$75% for a total accumulated dose of 2 Mrad. This is not a critical item since one collects about 1000 photoelectrons per GeV of deposited energy in a non-irradiated ECAL module. Also shown is the degradation of the energy resolution as function of the accumulated dose for different electron energies between 5 GeV and 100 GeV. The constant term that is induced due to a given irradiation dose is shown separately for doses between 0.5 Mrad and 5 Mrad. The line in the plot corresponds to a degradation of the constant term of 1.5% that is reached at a dose of 2.2 Mrad.

Taking into account an expected annual radiation dose at the shower maximum for the modules closest to the beam pipe of 0.25 Mrad, we conclude from the measurements that the ECAL can be operated under LHCb conditions for about eight years, degrading the constant term of the energy resolution from 0.8% to an acceptable 1.5%. This estimate is somewhat conservative and some better annealing might be expected, taking into account

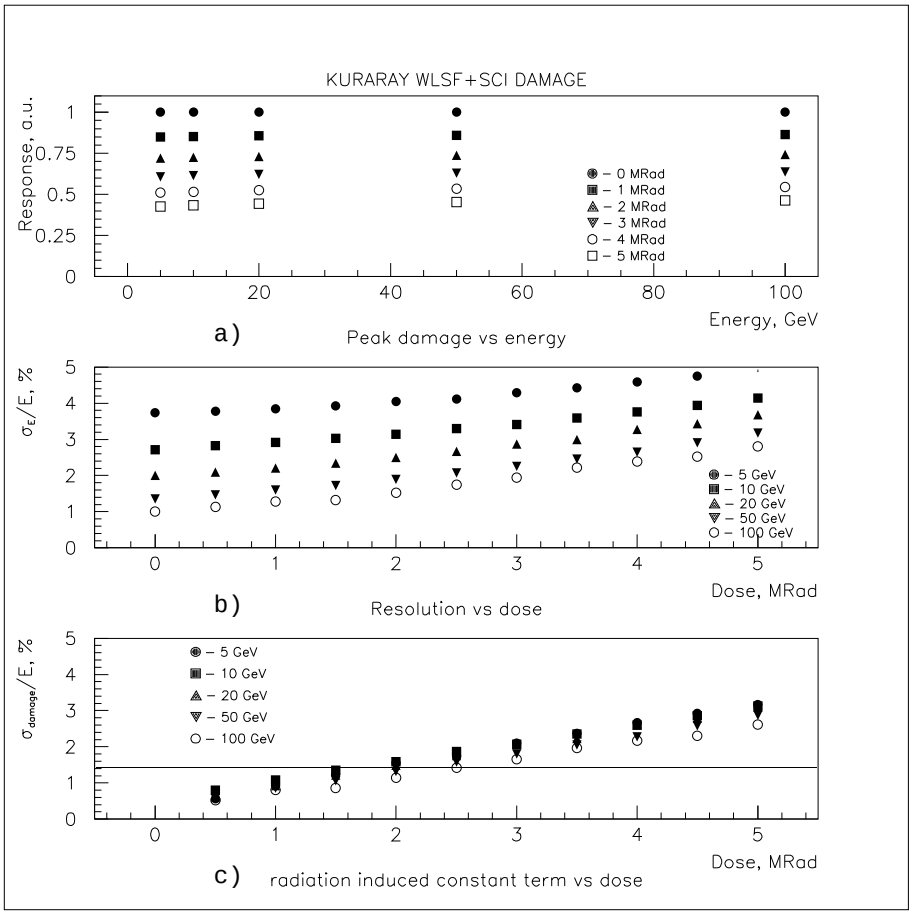

Figure 3.12: *Simulation studies of the radiation induced module performance degradation, using Y11-(200)MS fibers and PSM-115 scintillating tiles. The longitudinal dose profile from Figure 3.10 is assumed. Shown are the peak damage versus energy for various accumulated doses (a); the energy resolution degradation for various energies (b); the constant term degradation for various energies (c). The horizontal line corresponds to a constant term of 1.5%.*

the 200 times higher dose rate that was obtained at LIL in comparison to the one foreseen at LHCb. However, taking into account the simulation uncertainties on the expected radiation doses at the LHC, we have designed the ECAL detector such that the inner most modules closest to the beam pipe could be replaced after several years of operation, if this should become necessary (see section 5.2).

3.3 The hadronic calorimeter

3.3.1 Introduction

The main purpose of the hadron calorimeter (HCAL) is to provide data for the L0 hadron trigger. The required energy resolution of $80\%/\sqrt{E}$ is quite moderate, however the detector has to be fast in order to measure the particles transverse energy at a 40 MHz bunch crossing rate.

In view of choosing a fast fiber that allows to readout the HCAL (and the ECAL) within the required 25 ns, the timing properties of different fiber types have been studied with a special setup in the X7 test-beam line and compared to measurements using a N_2 UV laser [21].

In order to optimize the basic HCAL design and to measure its performance, a total of six prototypes have been constructed from 1997 till 1999 [33]. They differ by their cell sizes of 8×8 cm^2 and 16×16 cm^2, by their depth of 7.3 and 5.6 interaction lengths (λ_I), by their light collection scheme with one and two sampling regions in depth, and by their fiber type using Pol.Hi.Tech.(S250) and Bicron BCF-92 wavelength shifting (WLS) fibers. Many detailed measurements have been performed with the different prototypes at the X7 test beam [34]. Part of the results have been obtained in a combined run with SPD/PS, ECAL and HCAL, reading out the ECAL and HCAL with the fast 25 ns sampling electronics (see section 3.4).

In the following we will discuss those measurements that summarize the performance of the basic design, and we will in particular compare the results for the 7.3 λ_I and 5.6 λ_I long prototypes. Due to the stringent space requirements along the beam axis in the LHCb experimental hall and in order to be cost effective, a reduced HCAL length is preferred if the detector performance is not compromised.

We finally discuss the effect of irradiation on the HCAL performance, that has been determined from measurements of the degradation in light yield of the optical components due to radiation [35], and from simulation of the detector response when taking into account this degradation [36].

3.3.2 Choice of wavelength-shifting fibers

The pulse-shape properties of different wavelength-shifting fibers have been measured with a special setup that allowed to readout light from a 16×8 cm^2 big scintillating tile that was either produced by 80 GeV electrons converting in a lead absorber or by injecting the light from a N_2 UV laser. It was shown that the two methods are equivalent, and the pulse shapes measured on a total of six different fiber types could be compared.

Figure 3.13 shows the measured pulse shapes for three BICRON fibers of type BCF-92, BCF-99-29A and BCF-91A, for the Pol.Hi.Tech.(S250) fiber and for two KURARAY fibers of type Y-11(MS250) and Y-11(M200). The shortest pulse is obtained from the BCF-92 fiber with a FWHM of 9 ns. The currently not manufactured BCF-99-26A type is slightly wider with 12 ns FWHM. Two types of fiber have almost equal pulse shapes, that is Pol.Hi.Tech.(S250) and Y-11(MS250) with a width that is 1.7 times larger than the one of BCF-92. The fiber Y-11(M200) has 18 ns FWHM, e.g. twice as wide as BCF-92,

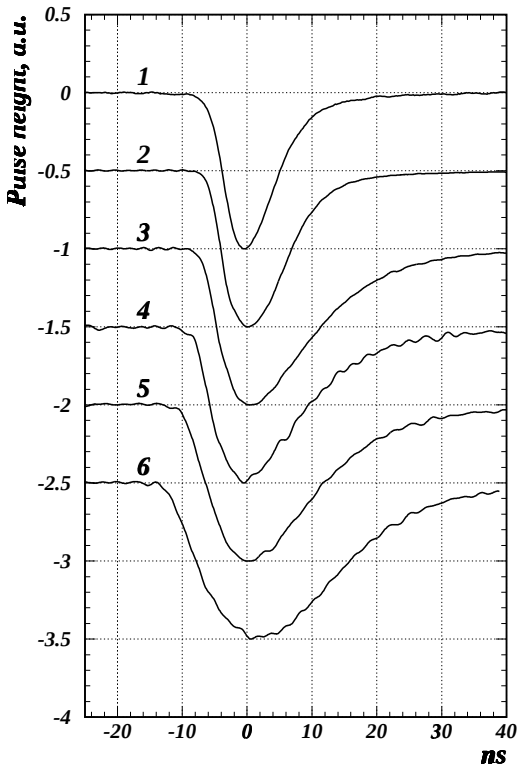

Figure 3.13: *The recorded pulse shapes for different WLS fibers: 1 - BCF-92; 2 - BCF-99-29A; 3 - Pol.Hi.Tech.(S250); 4 - Y-11(MS250); 5 - Y-11(M200); 6 - BCF-91A.*

while the BCF-91A fiber has the largest width of 23 ns FWHM, in accordance with the technical data given by BICRON [19].

Table 3.4: *The fiber decay time extracted from a fit to the pulse-shape measurements.*

Fiber type	Decay time
BICRON BCF-92	2.4 $\pm$ 0.4
BICRON BCF-99-29A	3.5 $\pm$ 0.4
Pol.Hi.Tech. (S250)	7.3 $\pm$ 1.1
KURARAY Y-11 (MS250)	7.2 $\pm$ 1.1
KURARAY Y-11 (M200)	8.8 $\pm$ 1.5
BICRON BCF-91A	10.8 $\pm$ 2.3

The exponential decay time of the fibers was determined by fitting the measured signal shapes by an appropriate function [21], and care was taken to de-convolute the response time of the PMT FEU-115M photomultiplier tube [37] that was used for readout, and the

decay time of the scintillating tile that was measured to be (1.8±0.3) ns. The Table 3.4 summarizes the decay times that have been obtained for the different fiber types. At present the preferred choice for the baseline design is the fastest BCF-92 fiber for the outer section of the HCAL, and the more radiation resistant Y-11(MS250) fiber for the inner section.

3.3.3 Performance of the basic design and choice of the detector length

The performance of the HCAL design has been determined by measuring the linearity of response and the energy resolution of the HCAL as function of the angle and of the position of the incoming particles. The results from the test-beam data and from simulation studies have been compared for the 7.3 λ_I and 5.6 λ_I long prototypes.

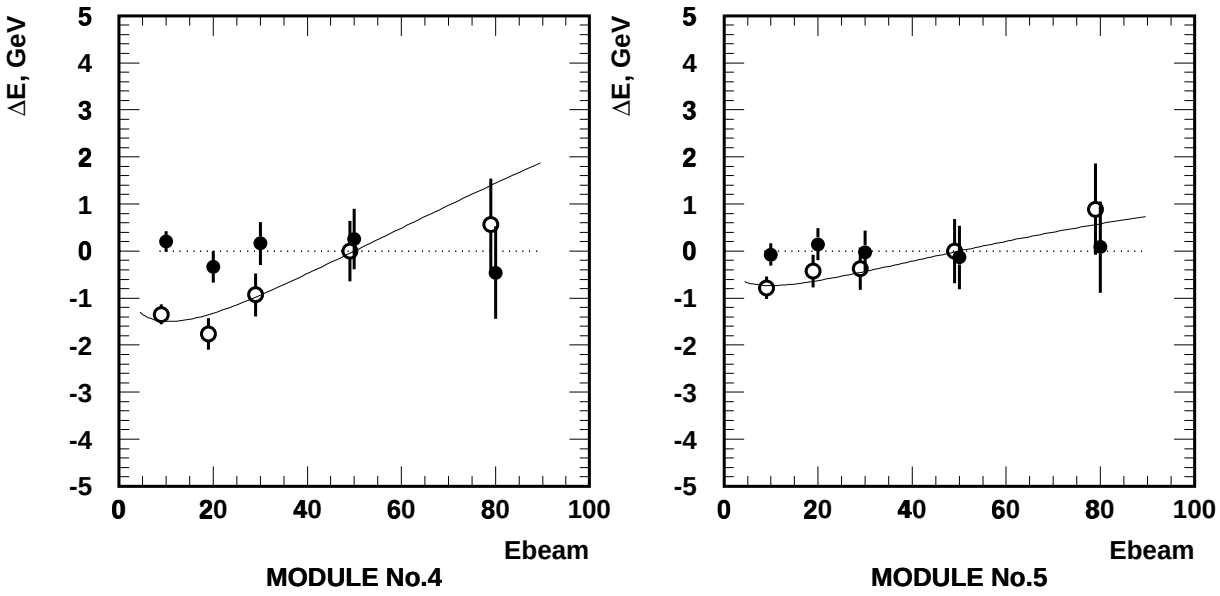

Figure 3.14: *The difference between the mean measured energy and the beam energy (calibration at 50 GeV). Open circles — raw data before correction. The curve is a fit of a correction function to the points (see text). The black circles are the residual of the fit. Left figure without compensation, right figure with compensation for light attenuation. The corrections become smaller but remain non-zero that is accounted for by a smooth logarithmic rise of the π^0 fraction in the shower. The data was taken at 9^0 of incident beam.*

In a non-compensating iron/scintillating-tile hadron calorimeter one expects a non-linearity in the response to pions as function of their energy. Since the fraction of electromagnetic energy in the shower is increasing logarithmically with energy, the relative response to pions is expected to slowly rise with energy. Another factor that can strongly affect the linearity is the light attenuation in the fibers that collect the light from several scintillating tiles while running in direction of the shower development over the full detector depth. Further non-linearity can be generated due to longitudinal shower leakage

and due to Cerenkov light that can be produced in the light mixer situated at the end of the module. The deviation from the linearity of the calorimeter response measured with the prototype for hadron beam energies between 10 and 80 GeV is shown by the open circles in the left plot of Figure 3.14. The curve is a fit to the data taking into account the effects of non-compensation and of light attenuation in the fibers [34]. The black points show the residual of the fit. In the right plot of Figure 3.14 it is shown that the effect of light attenuation in the fiber can be reduced when compensating the increase in light yield with depth, by reducing the optical contact between fibers and scintillating tiles by a few percent at the corresponding depth. The remaining non-linearity is in very good agreement with results that are obtained from a simulation study [34]. For trigger purposes the measured non-linearity is not a central issue, and we therefore have not included a compensation of the light yield in depth in our present baseline design.

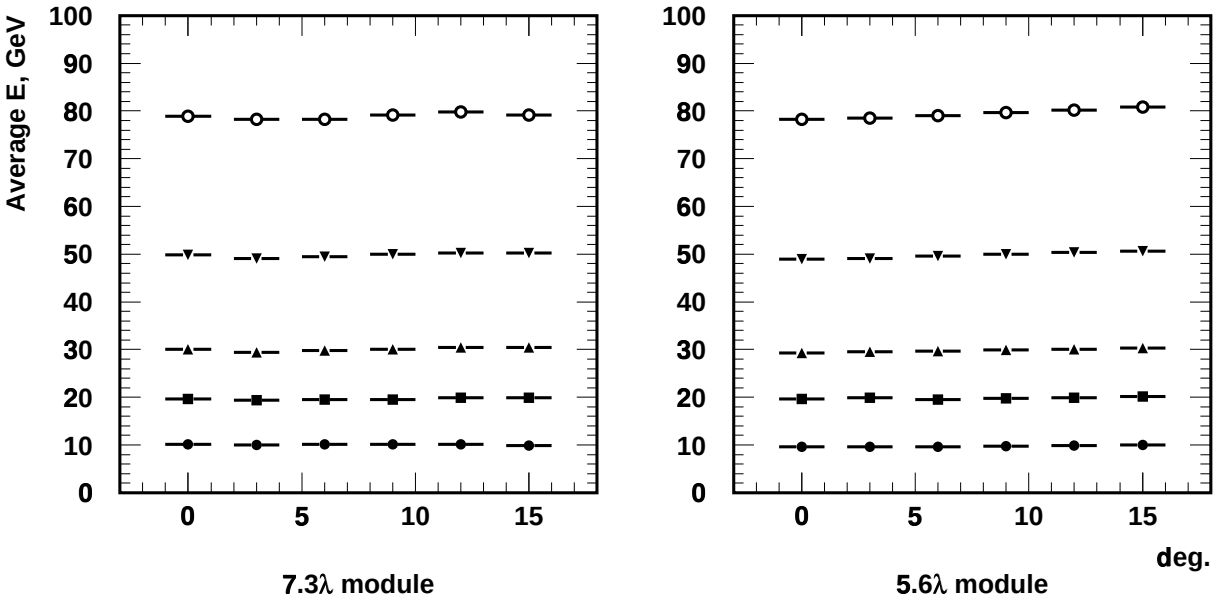

Figure 3.15: *The angular dependence of the response at different energies. On the x-axis is plotted the angle between the beam line and a line that is perpendicular to the HCAL front face.*

The dependence of the HCAL response on the angle of the incoming particle has been studied by rotating the prototype between 0^o and 15^o around a vertical axis that roughly traverses the HCAL at the average shower maximum. Figure 3.15 shows a comparison of the angular dependence of the response for the 7.3 λ_I and 5.6 λ_I long prototypes for pion energies between 10 GeV and 80 GeV. A very high degree of uniformity is seen for all energies. The short prototype shows some $\approx$3% leakage for 80 GeV pions. It should be noted however, that this effect will reduce substantially when taking into account the 1.2 λ_I additional interaction length that will be added due to the ECAL in front of the HCAL. From a scan with the particle beam across the prototype front surface the uniformity in response is measured to be well within $\pm$3%.

The energy dependence of the resolution for a sampling hadron calorimeter is described

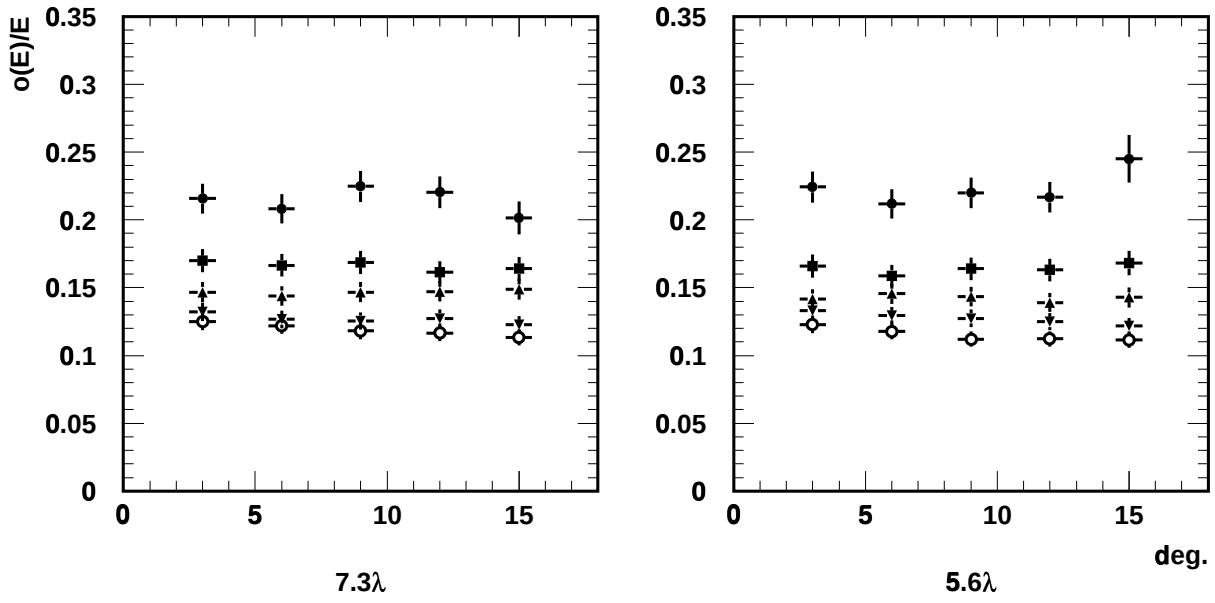

Figure 3.16: *The angular dependence of the HCAL resolution for two prototype thickness. Each set of points correspond to the beam energy of: 10, 20, 30, 50 and 80 GeV (from top to the bottom).*

by two parameters, the stochastic and the constant term. The first reflects the statistical fluctuation in the energy deposition by hadronic showers in the scintillating tiles. The second one is defined by intrinsic features of the calorimeter, like e/π ratio, inter-calibration, non-uniformity in the light collection for different fibers in the cell, non-linear response due to shower fluctuations in depth, energy leakage and cracks. A comparative study of the two prototype modules with different length has shown that their energy resolution is equal within errors. The angular dependence of the resolution is shown in Figure 3.16. A good uniformity is obtained within the experimental errors.

In conclusion from the results, and taking into account the advantage of a relatively short HCAL in the final design in view of the restricted space in depth and a reduced cost, we decided to built a 5.6 λ_I deep hadron calorimeter, keeping in mind that a 1.2 λ_I ECAL is positioned in front of it.

An analysis of the performance of the 5.6 λ_I prototype from data that were obtained in the combined test run using the 40 MHz readout electronics, has been compared in detail with simulation results using different software packages for the simulation of the hadronic shower development. The energy response to 50 GeV pions is shown by the hatched histogram in the left plot of Figure 3.17. The tail towards low energies due to leakage of the shower is well seen. However, this tail is not a concern for the hadron trigger performance since it only introduces some minor inefficiency for high E_T signal events but does not affect the rejection of low E_T minimum-bias events. The black dots on the histogram show the result of a Monte Carlo simulation that is in remarkable agreement with the data, when using the GEANT (MICAP+FLUKA) interface.

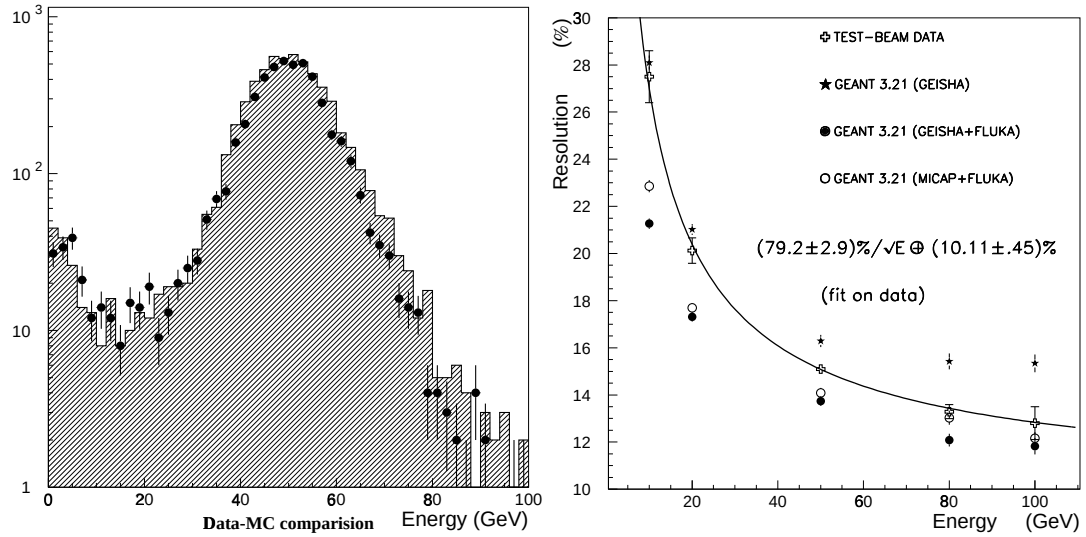

Figure 3.17: *Left: energy response for* 50 *GeV pions form test-beam data (hatched) and from simulation (dots). Right: HCAL Energy resolution, both for data and for simulation with three different hadronic interfaces.*

The energy resolution has been determined by fitting the energy spectrum with a gaussian distribution around $\pm 2.5\ \sigma$. The resolution extracted from data is shown in the right plot of Figure 3.17. The data have been fitted by the quadratic sum of the stochastic and constant term that result in $\sigma(E)/E = (79.2 \pm 2.9)\%/\sqrt{E} \oplus (10.11 \pm 0.45)\%$. A detailed comparison of different simulation packages for hadronic shower developments [36] is shown in the same plot. It can be seen that GEANT (GEISHA) overestimates the constant term although it provides a good description of the low-energy sector, GEANT (GEISHA+FLUKA) fails to reproduce a realistic sampling term and underestimates the constant term, while the best global agreement is provided by the GEANT (MICAP+FLUKA) interface, specially at high energies. The latter simulation package is used to study the performance of the hadron calorimeter under irradiation.

3.3.4 Detector performance under irradiation

The effect of irradiation on the HCAL energy resolution has been determined from simulation, using test-bench measurements of the optical components that have been irradiated in a hadron beam with the expected radiation dose.

The expected annual radiation doses for HCAL cells closest and second closest to the beam pipe are shown as function of the longitudinal segmentation in Figure 3.18. The highest dose is reached in the very front part of the innermost cells and reaches a maximum of 50 Krad per year, which translates to a maximum of 0.5 Mrad in ten years of operation. For cells that are second closest to the beam pipe the dose is already down by more than a factor of two.

In order to determine the effect of such radiation doses on the optical components due to hadron showers, scintillating tiles and fibers of different type have been irradi-

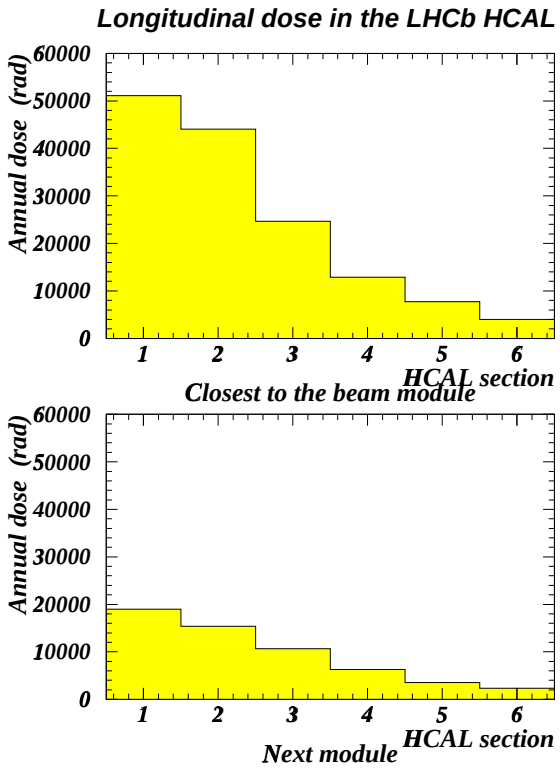

Figure 3.18: *Longitudinal radiation profiles for the innermost HCAL modules after one nominal year of operation. Each longitudinal section measures 195 mm.*

ated in the vicinity of the internal target station of the Serpukhov 70 GeV proton synchrotron [35]. In the following we will concentrate on the PSM-115 scintillating tile and the KURARAY-Y11 fiber, that are the baseline option for the innermost HCAL cells. Samples of scintillating tiles were irradiated over 25 days with an average rate of 70 Krad per day with total doses ranging between 80 Krad and 1500 Krad. The light yield of irradiated and non-irradiated tiles was measured with a special scanning system using a Sr^{90} source. The light yield of irradiated samples relative to non-irradiated tiles is shown in the left plot of Figure 3.19. The plot on the right shows the attenuation functions for non-irradiated and irradiated fibers that have been extracted from various radiation dose measurements with fibers of type KURARAY-Y11, assuming a 70% reflective mirror at the end of the fiber. One observes extra losses in light yield due to radiation damages of up to 20% for the tiles and of up to 15% for the fibers, both corresponding to a total dose of 0.5 Mrad. In contrast to the radiation tests with electrons (section 3.2.4), no annealing after irradiation with hadrons has been observed.

Using the attenuation functions that have been extracted from the test-bench measurements, the energy response of the HCAL has been simulated in order to study the radiation-damage effects on the energy resolution and efficiency. In Figure 3.20 the energy spectrum for 80 GeV pions for a non-irradiated detector is compared to an irradiated one for a total radiation dose of 0.5 Mrad and 1.0 Mrad. For a 0.5 Mrad dose the resolution for showers developing in the innermost modules is only slightly deteriorated by a 6% spread

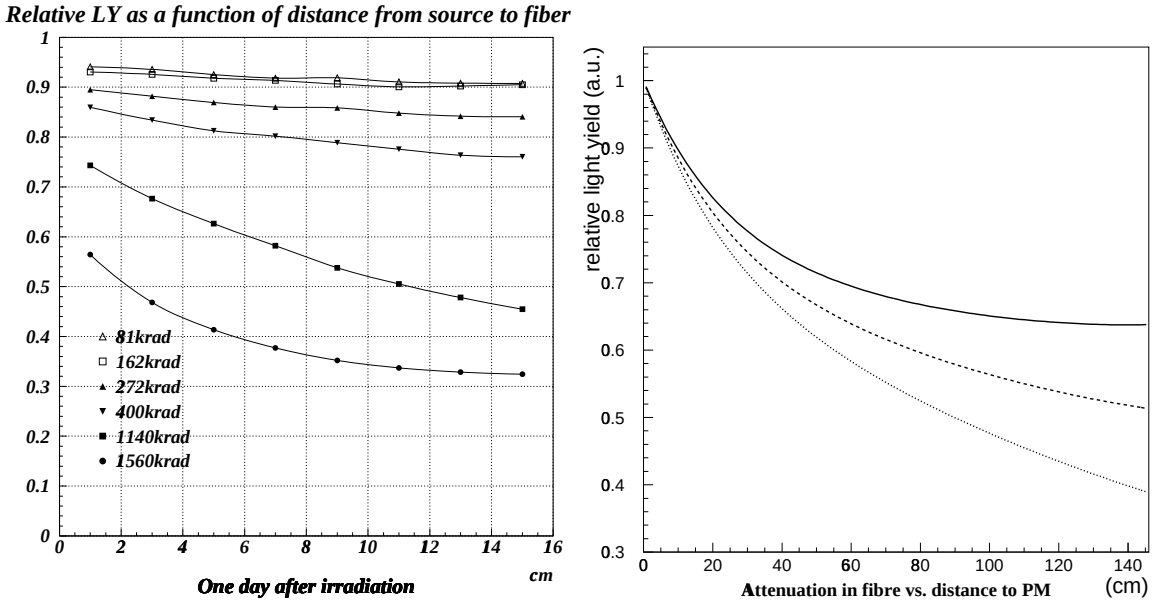

Figure 3.19: *Left: The relative light yield of a scintillating tile after irradiation to the one before irradiation for different accumulated doses. Right: The attenuation functions along a Y11 fiber. The solid line is for a non-irradiated fiber, the dashed lines correspond (in decreasing order) to the expected damage loss for a 10-year equivalent radiation dose, for 50 Krad/year and 100 Krad/year, respectively.*

that increases the 10% constant term to ≈12%. The deterioration on the next-to-central modules is negligible. To be conservative, and in order to take into account possible uncertainties in the determination of the expected radiation, the deterioration for a 1.0 Mrad total dose over ten years has been simulated, and shows an increase of the constant term to about 15%. In order to quantify the effect of radiation on the HCAL efficiency, one can define inefficiency as the fraction of events with an HCAL energy readout below 60% of the deposited energy (corresponding to low-energy tails below 2.5 σ for 80 GeV pions). An inefficiency of ≈8% for a non-irradiated module increases slightly to ≈9% and ≈11% for a total radiation dose of 0.5 Mrad and 1.0 Mrad, respectively.

From these studies we are confident, that the radiation resistance of the designed detector is sufficient to operate even the innermost HCAL cells over the 10 years of LHCb operation without any relevant performance degradation.

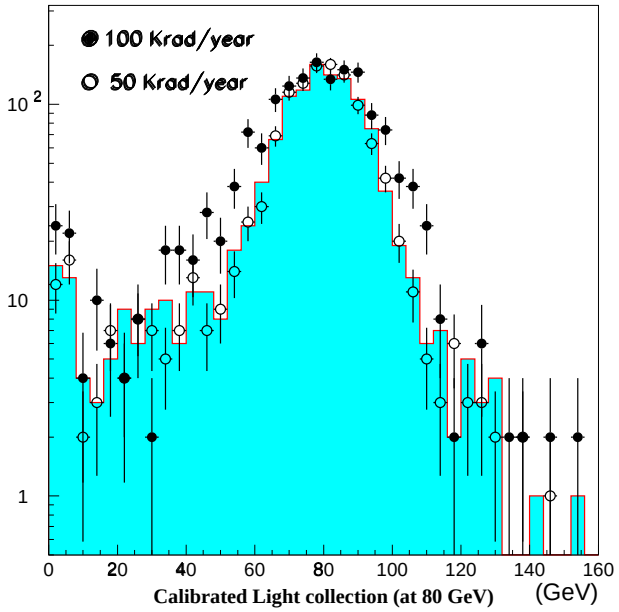

Figure 3.20: *Simulated HCAL performances for 80 GeV pions, after 10 years of operation. The histogram represents non-irradiated conditions, the white dots correspond to a total dose of 0.5 Mrad, the black dots to a total dose of 1.0 Mrad.*

3.4 Electronics

3.4.1 ECAL/HCAL front-end chip and front-end card

The design of the ECAL/HCAL electronics is described in section 5.4 and in [12] together with a detailed description of the tests. After a series of prototype iterations, a new version of the ECAL/HCAL front-end chip that includes a buffer amplifier and an integrator with a 2 pF feedback capacitor (for details see Figures 5.24 and 5.26), was produced in August 1999. This chip was used in the last test beam period of 1999. The performance of this chip is summarized in Table 3.5.

	Simulation Results	Test Bench Results
Dynamic range	1.4 V	> 1.4 V
Non linearity	0.5%	$< 1\%$ over the whole dynamic range
Residue after 25 ns	$< 0.5\%$	$< 1\%$
RMS noise after subtraction	1 ADC count (i.e. 250 μV)	1.2 ADC counts (i.e. 300 μV)
Power consumption	40 $mW/channel$	38 $mW/channel$
Open-loop gain of integrator	~ 60 dB	~ 60 dB
gm (input PMOS) of integrator	34 mA/V	18 mA/V
Fall time	3 μs	2 μs
Rise time	2.5 ns	5 ns with a 8 pF parasitic capacitance at the integrator input
Input impedance of integrator	190 Ω	270 Ω

Table 3.5: *Test bench measurements.*

As can be seen, the functioning is satisfactory. The linearity is good, the rise time of the chip is small with respect to the one of the integrated pulse. The noise level is slightly higher than foreseen and is degraded further when the chip is integrated in the card, as will be discussed below. A further prototype has therefore been ordered with a higher feedback capacitor of 4 pF. First measurements (June 2000) have shown that, as expected, the noise is reduced by a factor of two. Of course the charge gain of the amplifier is also reduced by a factor of two, however even in this case, the maximum current required from the PM for a pulse corresponding to the highest ADC count is 20 mA, which is not too demanding for the PM linearity.

A prototype of the front-end card has also been built for the summer of 1999. It includes the main functionalities foreseen in the final card except the trigger computation which will be studied in dedicated prototypes built in 2000. The card had 16 channels and was assembled in 6U size. The card schematic can be seen in Fig. 3.21 and a photograph of the prototype in Fig. 3.22.

The card also included some testing facilities which will not be implemented in the final card, such as the possibility to spy the direct ADC results before subtraction of

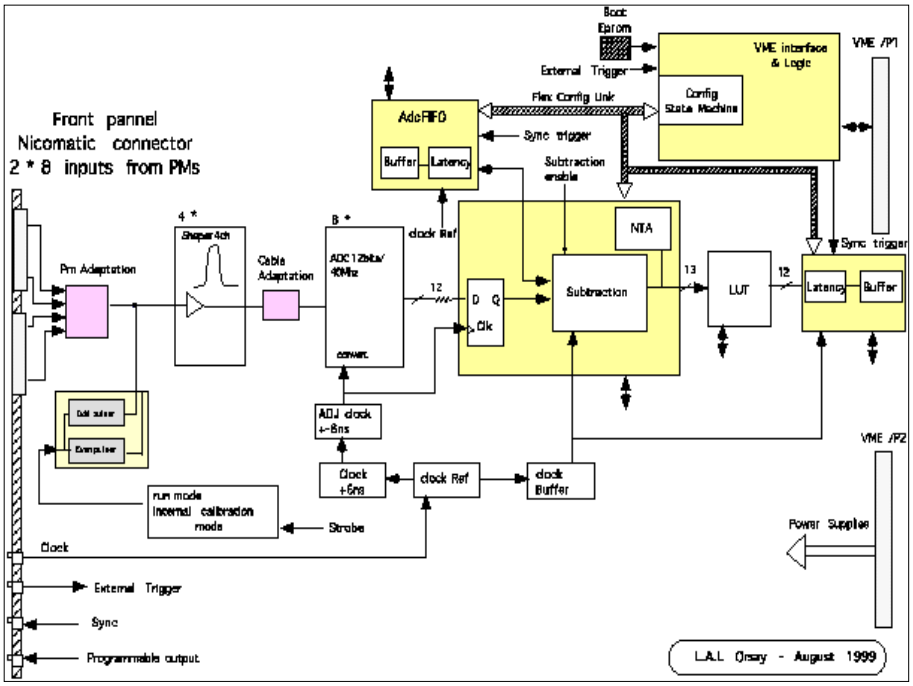

Figure 3.21: *Schematics of the prototype of the front-end board (FEB).*

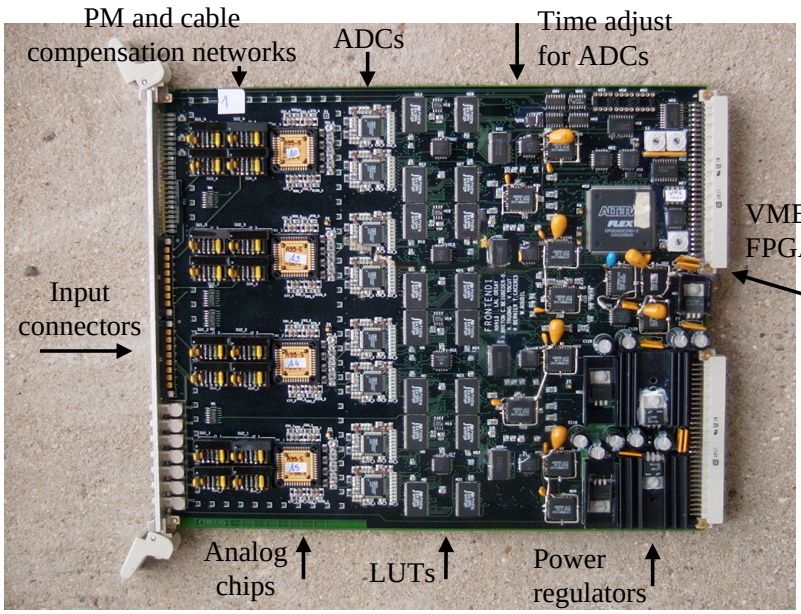

Figure 3.22: *Top layer of the prototype FEB.*

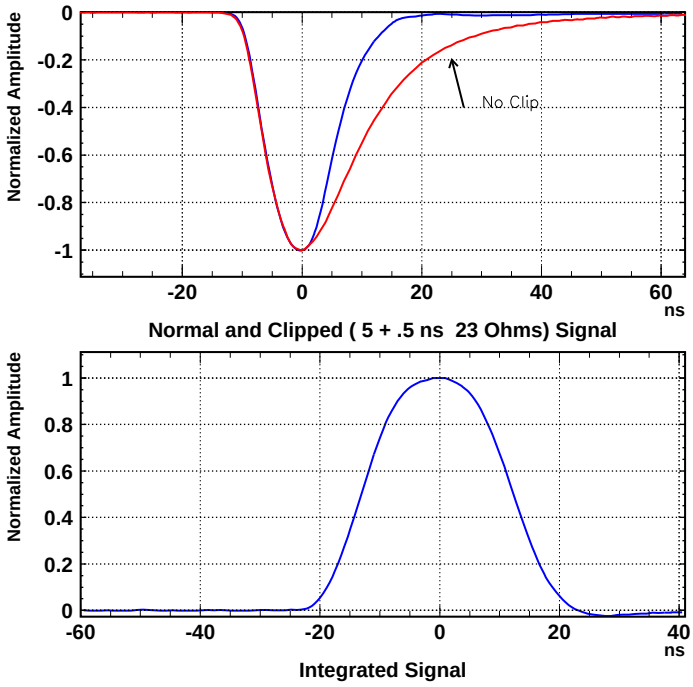

Figure 3.23: *80 GeV HCAL signals. The upper figure shows the PM signal before and after clipping, the lower one shows the same signal at the output of the integrator.*

the preceding pulse. In the prototype the derandomiser buffer after the trigger, which is normally used to store events to be readout, is used to copy N successive samples for each trigger. In this way it is possible to check how a large energy pulse influences successive samples.

The card was first used in test-bench measurements to study noise level and crosstalks. From a study of the noise in each channel and of the noise of the sum of all 16 channels, the incoherent noise and the coherent noise across the card was obtained. The values measured are respectively 1.6 and 0.5 ADC counts. Measurements were also done where the subtraction of the preceding pulse was performed not by the FPGA on the card but by software after data logging. In this way the sample number used for subtraction and therefore the effective integration time could be varied. Thus the noise before the integrator (essentially due to the buffer amplifier and usually called parallel noise) and the noise after the integrator (essentially the ADC input noise and usually called series noise) could be separated. The values obtained are 1.3 ADC counts (for 25 ns effective integration time) for the parallel noise and 0.5 ADC count for the series noise. A sizeable improvement of the parallel noise is expected with the new chip. The impact of the amplifier noise on the physics performance has been studied by simulation [15], and a noise of 1.3 counts typically contributes to the π^0 mass resolution at the level of about 30% of the resolution from the calorimeter energy and position accuracy. At this level the impact is therefore negligible. Crosstalks between channels were found to be typically less than 0.5%, except for one combination where it is 1.5%. The cause is understood and

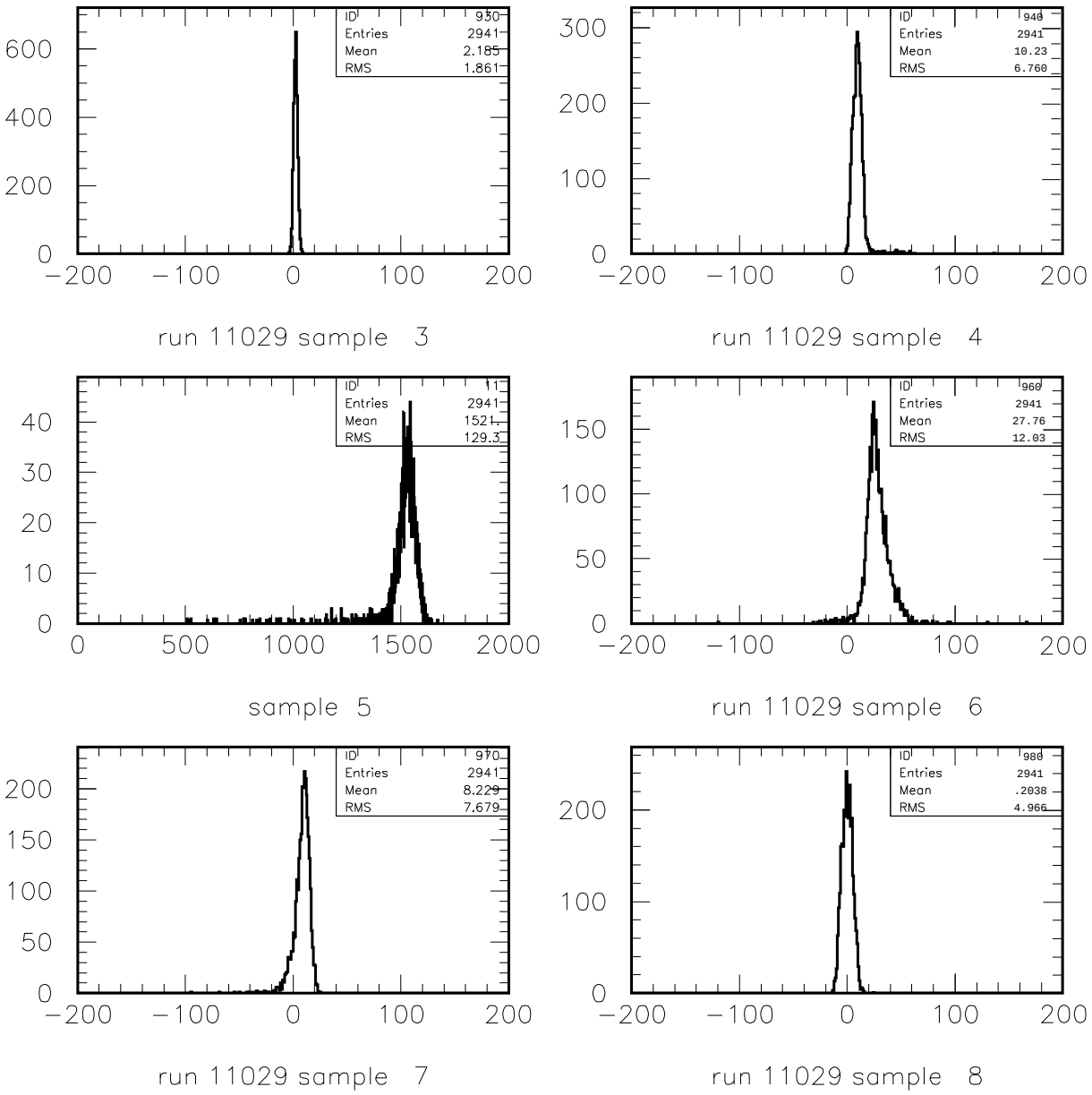

Figure 3.24: *Pulse-height spectrum of 50 GeV electrons measured in 6 successive ADC samples. Sample 5 is centered at the maximum of the integrated pulse. The horizontal scale is in ADC counts. Note the different horizontal scale for sample 5.*

corrective measures will be implemented reducing all crosstalks to a level of 0.3% or less.

The card was also used in beam tests with HCAL and ECAL signals. On Fig. 3.23 are shown an average PM HCAL pulse (averaged over 1000 measurements on a digital scope) and the resulting integrated pulse. One can notice the flat maximum stable within 1% over ± 2 ns and the small residual at ± 25 ns. Pulse-height spectra obtained with 50 GeV electrons are shown on Fig. 3.24. The sample on which the pulse is centered is sample 5. It can be seen that on average 0.7% and 2% of the pulse are measured respectively in sample 4 and 6 with fluctuations due to time jitter and photo-electron statistics. This

satisfies our requirement of independent pulse measurement every 25 ns.

3.4.2 Preshower front-end chip prototype

The main challenge of the PS and SPD electronics is to cope with the fluctuating pulseshape caused by the small number of photoelectrons produced by a MIP (about 25). This pulseshape was therefore studied with signals produced in a PS/SPD prototype by cosmic rays or test-beam particles, and compared to a simulation program which includes effects of photon creation in the coiled WLS fiber, photon propagation and attenuation, and photoelectron generation in the PM [38].

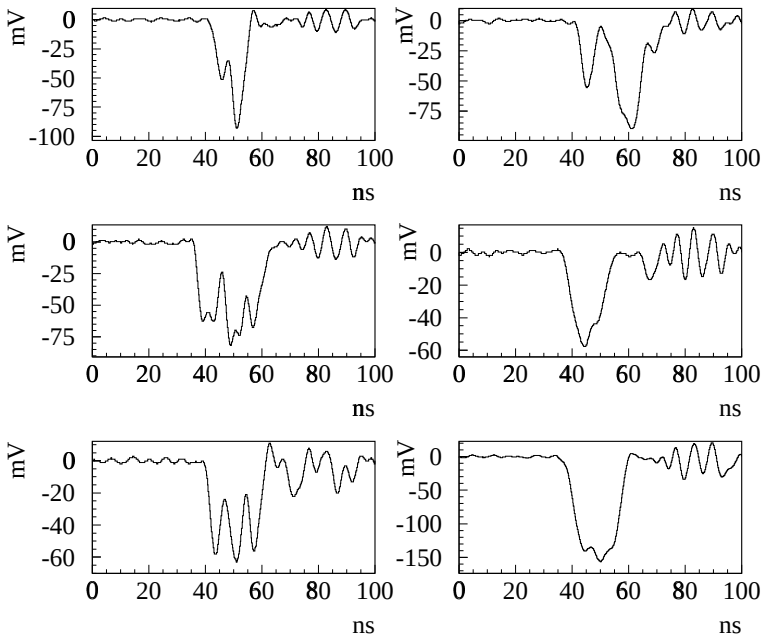

Figure 3.25: *Various 1 MIP signals in a preshower cell.*

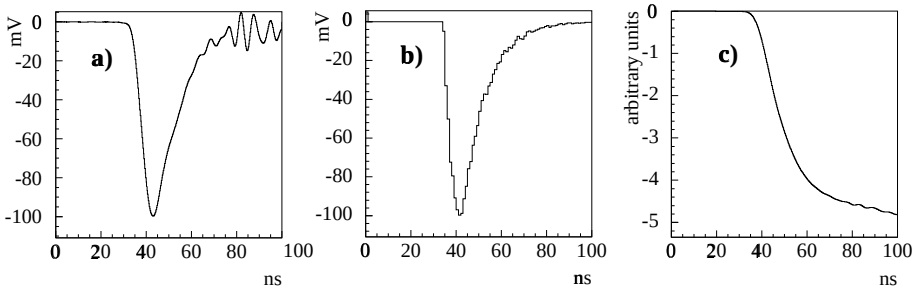

Figure 3.26: *Average 1 MIP signal for cosmic rays (a) and from simulation (b), and the integrated signal for cosmic rays (c). The oscillation between 70 and 90 ns is a parasitic pickup that should be neglected.*

Typical MIP signals are shown on Figures 3.26 and 3.25. After integration over 25 ns, 85% of the total charge of the pulse is collected. In the case of a 5 MIPs signal produced by high energy electrons in the prototype PS counter, Figure 3.27 shows that this fraction has a fluctuation of 4%. Therefore, with such an integration a measurement of the PS signal can be done with sufficient accuracy compared with the fluctuation on the number of MIPs produced by electrons in the PS counter.

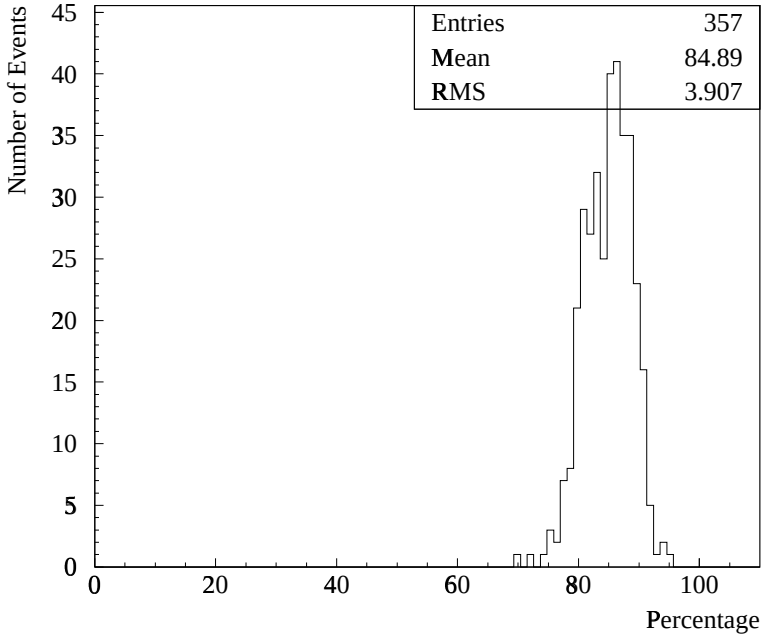

Figure 3.27: *Fraction of a 5 MIPs signal after 25 ns.*

The design of the preshower-amplifier integrator is described in section 5.5.2 and in [39]. Because of the requirement of maximizing the integration time, the solution adopted consist in connecting alternatively, every 25 ns, two integrators for each channel and to reset one when the other is active (for the schematics see Fig. 5.28). A first working prototype of one channel of the PS front-end chip was obtained in spring 2000. The output noise level is 1 mV i.e. 1 ADC count of the foreseen 10 bits ADC. The pedestals and gains of the two integrators are slightly different, as expected. The pedestals are 10 and 20 mV, respectively. After subtraction of the pedestal the deviation from linearity of the system is less than 1% over the full 1 Volt ADC range. All these values agree with specifications. A digital-scope picture of a pulse-generator input pulse and of the corresponding output pulse are shown on the left of Fig. 3.28.

The chip was connected with the ADC, pipeline, and buffer system of a spare front-end card of the ECAL/HCAL. In this way a readout of successive samples of the chip could be performed while sending at the chip input pulses from a preshower prototype counter connected to a multianode photomultiplier. An example of the average of 50 pulses is shown on the right of Fig. 3.28. As expected (see section 5.5.1) the sample following the main one is about 20% of the main sample signal. More precise measurements will be done in the coming year and further prototypes with 8 channels per chip will be ordered.

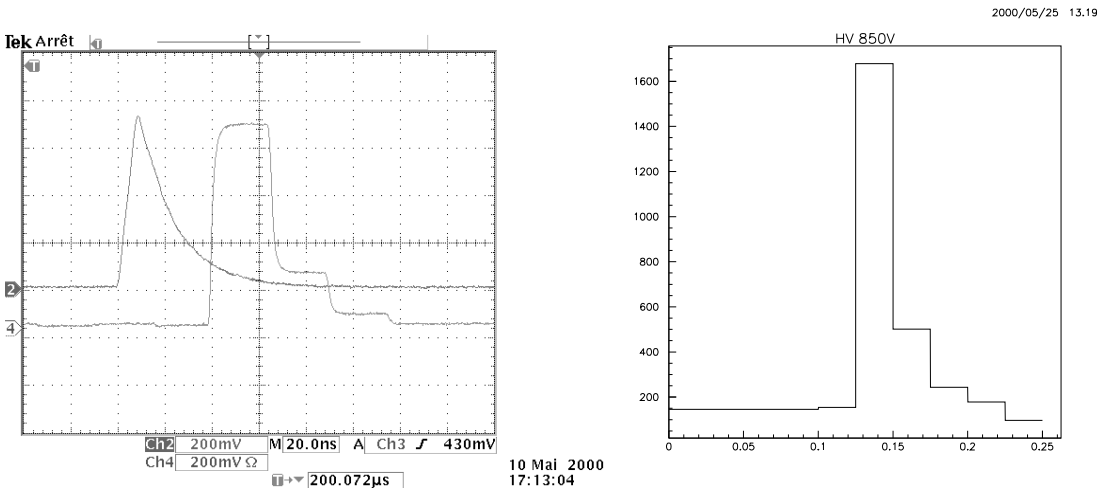

Figure 3.28: *Left: Input test pulse and output of preshower front-end chip. Right: Successive ADC samples of an average preshower pulse. The horizontal scale is in µs.*

Chapter 4 Physics Performance

The physics simulations have been performed in the general framework of the SICB software (SICBMC v231), which is a GEANT3 based Monte Carlo program able to simulate events and their background up to digitisations in the LHCb detector. It includes all secondary interaction processes, with thresholds of 1 MeV for electrons/photons and 10 MeV for hadrons. Proton-proton interactions at $\sqrt{s}$ =14 TeV are simulated using the PYTHIA event generator version 6.1 [40]. A multiple-interaction model is used, with varying impact parameter and running p_T cut-off, tuned [41] to reproduce existing low-energy data. The parton distributions are taken from CTEQ4L. Note that there has been an important evolution in the tuning of these variables since the technical proposal, which affects detailed comparisons of the trigger and physics efficiencies.

The digitisation results (SICBDST v232r2) were used as input to the simulation of the calorimeter trigger logic, in order to measure its performance. For the simulation of the offline analysis of physics channels, the programme which performs the reconstruction of the various particle showers in the calorimeter system should be considered as a preliminary version of a realistic data analysis software. A number of algorithms need in depth study and much evolution is foreseen. Some results of the performance evaluations may change as the software gets more refined. These modifications should in general improve the final performance of the experiment.

4.1 Performance of the Level 0 calorimeter triggers

The calorimeter triggers and their implementation are described in detail in several LHCb notes [11, 42, 43, 44]. The general principle consists in identifying high transverse energy hadron, electron, or photon candidates from B hadrons in the calorimeter system and to tune the rate of these triggers applying suitable E_T thresholds. In this chapter a short description of the trigger logic is given before discussing the simulation results.

4.1.1 Structure of the trigger

The basic scheme is illustrated on Fig. 4.1. The successive steps are :

- The result of digitisation in each cell of ECAL and HCAL is converted in transverse energy using a look-up table.
- A sum on every 2 $\times$ 2 cluster of cells is performed.

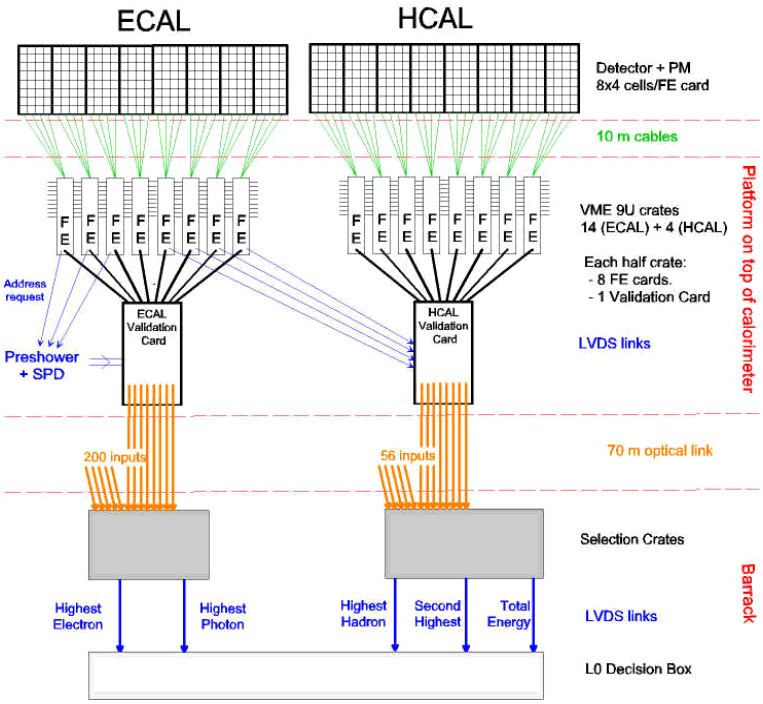

Figure 4.1: *Global view of the Level 0 calorimeter triggers.*

- The highest sum on each front-end board is selected for further processing. For ECAL clusters, the associated preshower and SPD information is used to validate them as electron or photon candidates. For HCAL clusters, the associated electromagnetic transverse energy is added.

- The highest E_T electron, photon and hadron candidates are selected and transmitted to the Level 0 decision unit which applies the proper thresholds and performs the combinations giving the global Level 0 decision.

4.1.2 Performance results

The results of Level 0 trigger simulations can be found in [45]. On all figures are shown as function of the E_T cut the efficiency for the selected channel (full circles, left scale), and the rejection factor of the minimum bias events (open circles, right scale). The efficiency is measured on events where the decay products are in the spectrometer acceptance.

The performance of the hadron trigger has been investigated on the $B_d^0 \to \pi^+\pi^-$ and $B_s^0 \to D_s^{\mp}K^{\pm}$ channels. The efficiency curves of Fig. 4.2 reflect the B-meson decay kinematics. Assuming that this trigger is given the bandwidth foreseen in the technical proposal, a threshold at 3.4 GeV is needed to suppress minimum bias events by a factor 16. This will accept 68% of the first channel, and 42% of the second. For the same rejection, the corresponding signal efficiencies were 65% and 35% in the technical proposal.

In the case of the electron trigger, a rejection factor of 100 is obtained for an E_T threshold around 2.4 GeV (see Fig. 4.3). This accepts about a quarter of the inclusive B_d^0

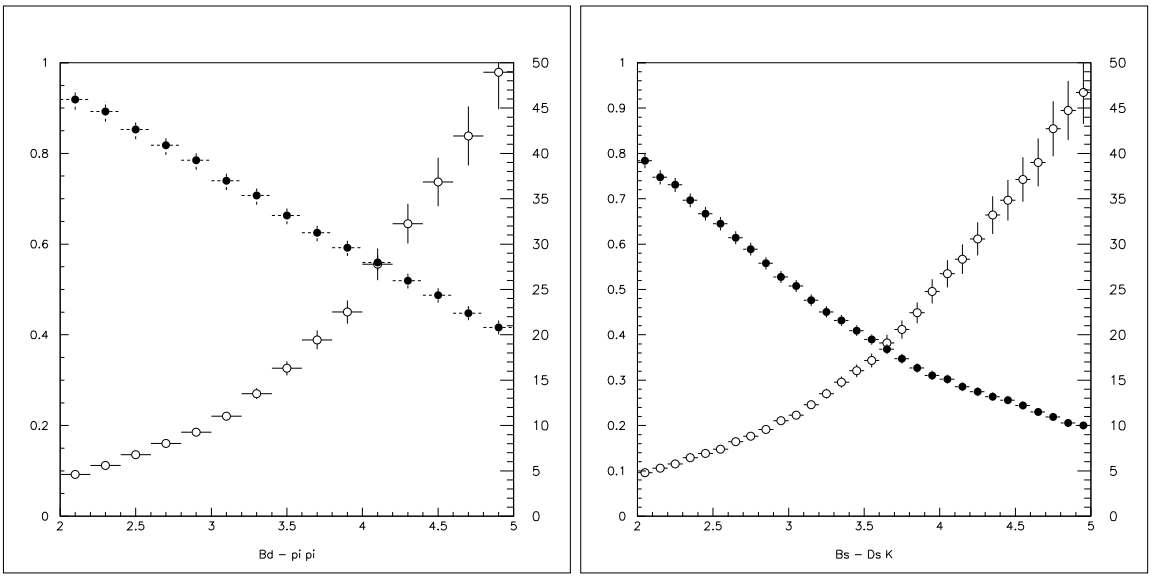

Figure 4.2: *Efficiency for the $B_d^0 \to \pi^+\pi^-$ (left) and $B_s^0 \to D_s^{\mp}K^{\pm}$ (right) for the hadron trigger as function of the E_T threshold in GeV. The efficiency (full points) is given on the left scale while the minimum bias rejection (open points) is given on the right scale.*

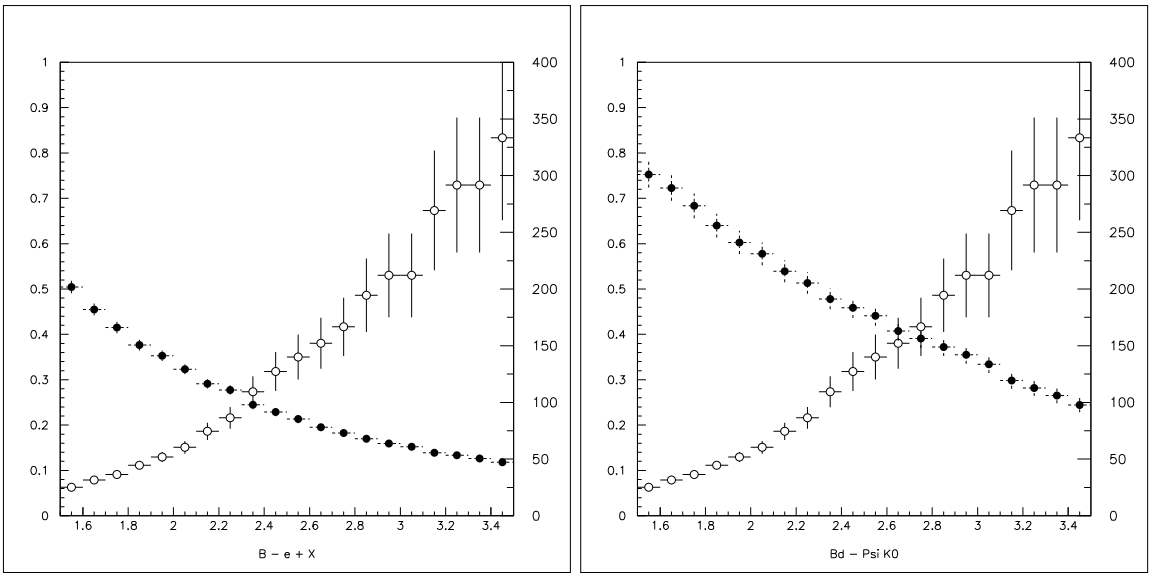

Figure 4.3: *Efficiency for $B_d^0 \to e^+\nu_e X$ (left) and $B_d^0 \to J/\Psi K_S^0$ (right) for the electron trigger as function of the E_T threshold in GeV. The efficiency (full points) is given on the left scale while the minimum bias rejection (open points) is given on the right scale.*

semileptonic electron decays, and about 50% of the $J/\psi K^0_S$ decays of the B^0_d, when J/ψ gives an electron pair, again slightly better than the technical proposal values.

A photon trigger may be useful for the study of specific physics channels. Figure 4.4 shows the effect on the efficiency for $B^0_d \to K^*\gamma$ events. An E_T threshold around 3.8 GeV will limit its bandwidth to 1/400 of the minimum bias, and will increase the Level 0 trigger efficiency from 47% to 58% for this channel [45]. Being quite efficient for the events in which the decay kinematics has given a large transverse momentum to the photon, this trigger will be needed to record the majority of events selected by kinematics cuts at the analysis stage.

In summary, the trigger performance studies have essentially confirmed the early evaluations of the technical proposal.

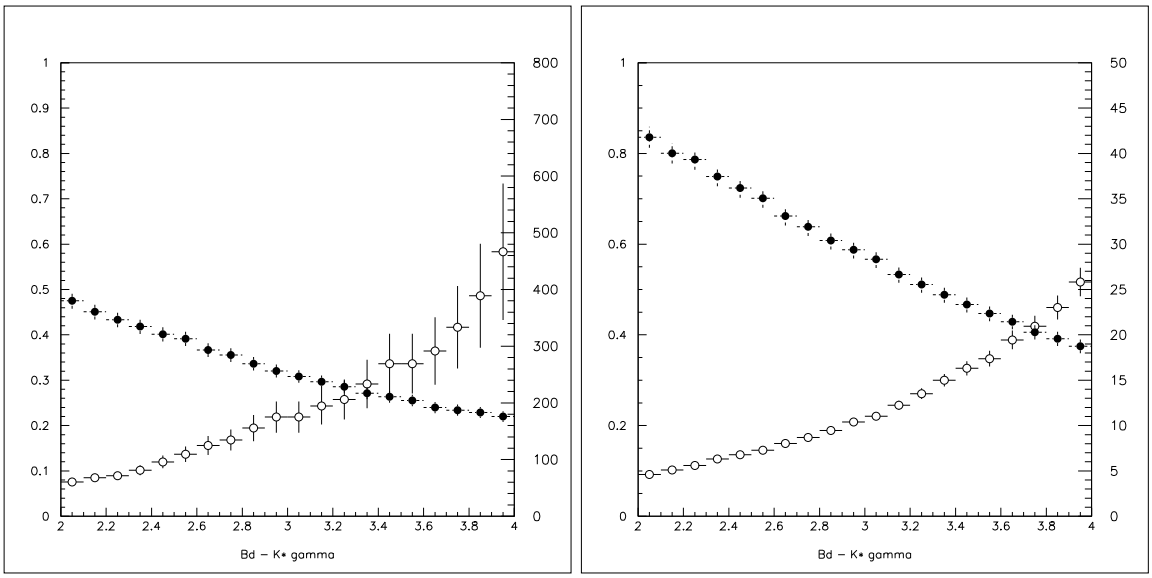

Figure 4.4: *Efficiency for $B^0_d \to K^*\gamma$ events for the photon trigger (left) and the hadron trigger (right) as function of the E_T threshold in GeV. The efficiency (full points) is given on the left scale while the minimum bias rejection (open points) is given on the right scale.*

4.2 Reconstruction of final states containing a π^0

The ability to perform physics analysis of decay channels containing a π^0 in the final state is essential for a broad coverage of CP-violation physics, and a constrained determination of the parameters which describe it. Two channels of particular interest and different kinematics characteristics have been simulated [2] in order to evaluate the potential given by the electromagnetic calorimeter. Studies are still preliminary, and with foreseen improved reconstruction algorithms a substantial improvement in efficiency is expected.

4.2.1 $B_d^0 \to \pi^+\pi^-\pi^0$

This channel is dominated by the two body $\rho\pi$ decays. Of particular importance are the regions of interference between $\rho^0\pi^0$ and $\rho^+\pi^-$ modes.

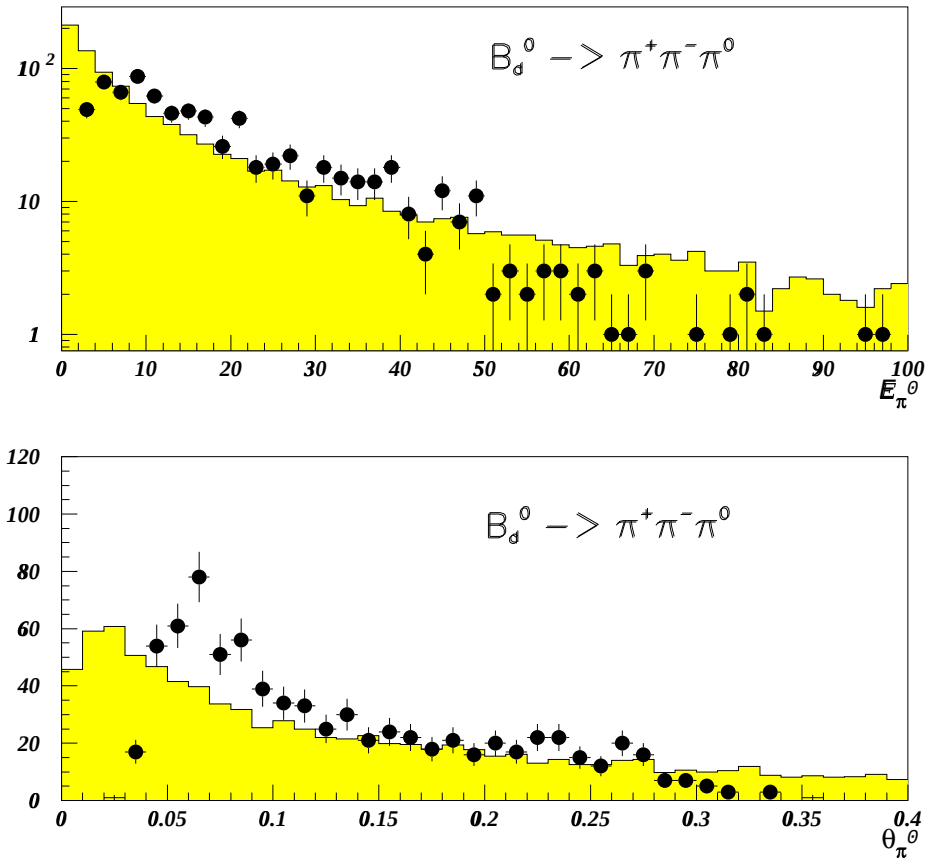

Figure 4.5: *Energy E_{π^0} [GeV] and emission angle θ_{π^0} [rad] of the π^0 mesons from $B_d^0 \to \pi^+\pi^-\pi^0$ events. The solid symbols are the distribution of the reconstructed quantities, while the shaded histograms represent the generated distributions scaled down by a factor 10.*

Fig. 4.5 shows the π^0 angular and energy distribution of the generated and reconstructed events. At the generation level B mesons emitted in a 400 mrad cone around the beam axis have been selected. The reconstruction requires that the charged pions momenta are measured in the tracker and that both photons from the π^0 are separately reconstructed in the calorimeter. No kinematical cuts have been applied at this stage. As can be seen, the π^0 reconstruction efficiency is low above 50 GeV and under 3 GeV, but is rather smooth between these limits. Further developments of the reconstruction algorithms may improve this efficiency particularly in the high energy region, where the

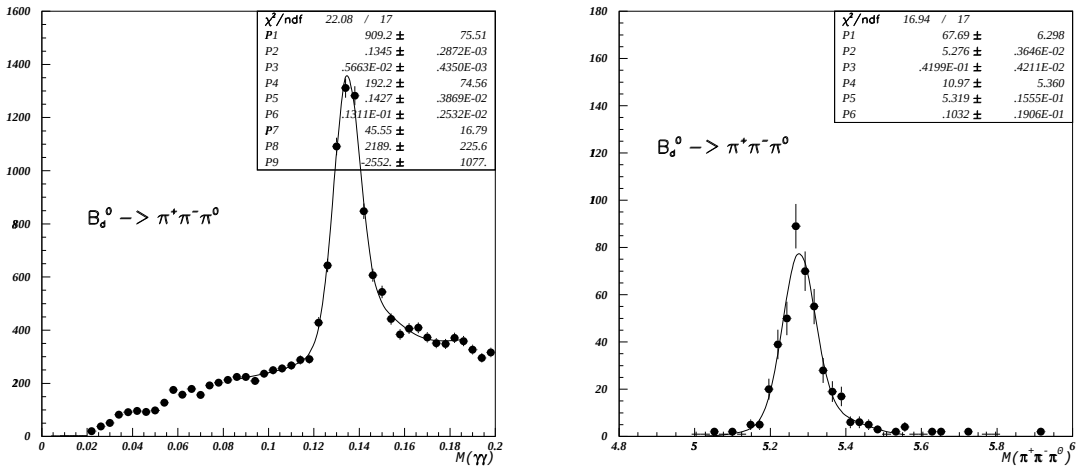

Figure 4.6: *Left: Reconstructed invariant mass for π^0 candidates in $B_d^0 \to \pi^+\pi^-\pi^0$ events. Right: Reconstructed invariant mass of $\pi^+\pi^-\pi^0$ for $B_d^0 \to \pi^+\pi^-\pi^0$ candidates. A 3σ cut on the π^0 mass has been applied.*

decrease of efficiency is due to merging photons. The 2γ mass spectrum is shown on the left of Fig. 4.6.

The combinatorial background resulting from the association of all photons detected in the events is included. The π^0-mass resolution of 5.7 MeV does not include a contribution from electronics noise, which however should be negligible [15]. The reconstructed B_d^0 invariant-mass spectrum (right of Fig. 4.6) has a resolution of 42 MeV, which reduces to 35 MeV when the π^0 mass constraint is imposed.

The Dalitz plot for reconstructed $B_d^0 \to \pi^+\pi^-\pi^0$ decays is shown on Fig. 4.7. The bottom left corner corresponding to very low energy π^0 is strongly depopulated. Otherwise the ρ bands and interference regions are clearly visible.

With an estimated branching ratio of the order of 5×10^{-5}, this channel would yield, according to this analysis, slightly over 100 events per year. This is 5 times less than the $\pi^+\pi^-$ channel yield which has a 10 times smaller branching ratio. There are two main loss causes: a factor 3 comes from photon conversion between the interaction point and the calorimeter, and a factor 9 is due to photon isolation and energy cuts. The possible recovery of photons converted downstream of the magnet and the development of analysis improvements using softer cuts are likely to substantially increase the efficiency for this channel.

4.2.2 $B_d^0 \to \overline{D^0} K^{*0}$

A constrained determination of the angle γ of the unitarity triangle has been discussed in the technical proposal. It proceeds through the measurement of the decay rates of the following channels:

- $B_d^0 \to \overline{D^0} K^{*0}$

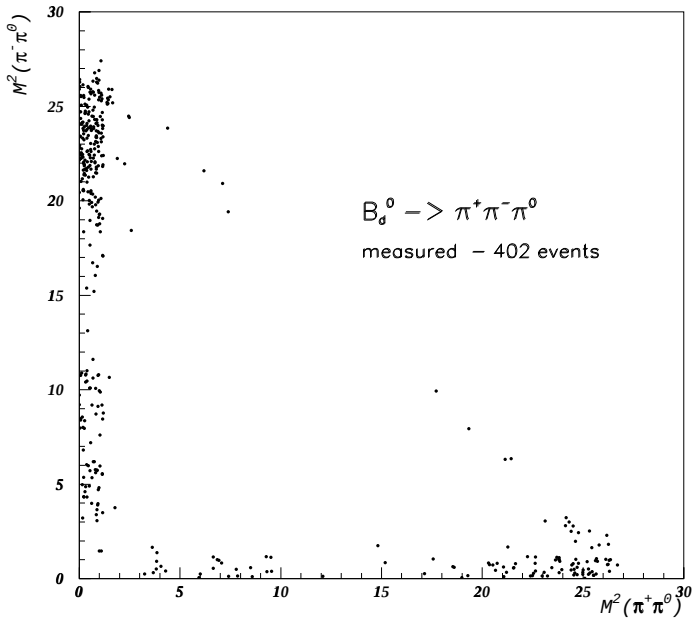

Figure 4.7: *The Dalitz plot for reconstructed $B_d^0 \to \pi^+\pi^-\pi^0$ decays after LHCb acceptance cuts and kinematics cuts.*

- $B_d^0 \to D^0 K^{*0}$
- $B_d^0 \to D^1 K^{*0}$

and charge conjugate channels, with D^1 being the CP=+1 eigenstate of the neutral D meson.

The final states considered in the technical proposal are only those consisting of four charged particles, in which the D^0 ($\overline{D^0}$) decays into $K^-\pi^+$ ($K^+\pi^-$). The estimated visible branching fractions are quite low, and the accuracy of the measurement will be limited by statistics. The possibility of an appreciable statistical improvement using the large branching ratio of the decay of the D^0 ($\overline{D^0}$) into $K^-\pi^+\pi^0$ ($K^+\pi^-\pi^0$) has therefore been considered. The channel $\overline{D^0}K^{*0}$ has been simulated and its reconstruction has been studied.

One starts from a set of events for which the four charged tracks from the decay are reconstructed in the spectrometer. The π^0 spectrum is softer than that of the $B_d^0 \to \pi^+\pi^-\pi^0$ channel studied above. The $\gamma\gamma$ mass spectrum shown on Fig. 4.8 exhibits a high mass tail due to pile up of neighboring tracks with one of the photons. The main π^0 mass peak has a good resolution equal to 6.7 MeV. The D^0 mass resolution is reduced from 18.6 MeV to 13.2 MeV when the π^0 mass constraint is imposed (Fig. 4.9). The reconstruction of the B_d^0 mass from the measured momenta of all particles gives a mass resolution of 29.4 MeV. When a kinematics fit is performed, with the π^0 and D^0 masses imposed, the B_d^0 mass resolution becomes 12.2 MeV (Fig. 4.10). This consid-

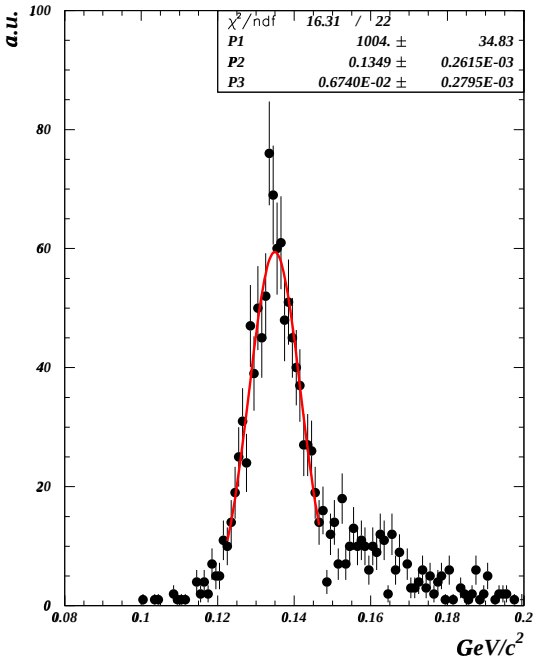

Figure 4.8: *Reconstructed invariant mass for π^0 mesons from $B_d^0 \to \overline{D^0}K^{*0}$ decays.*

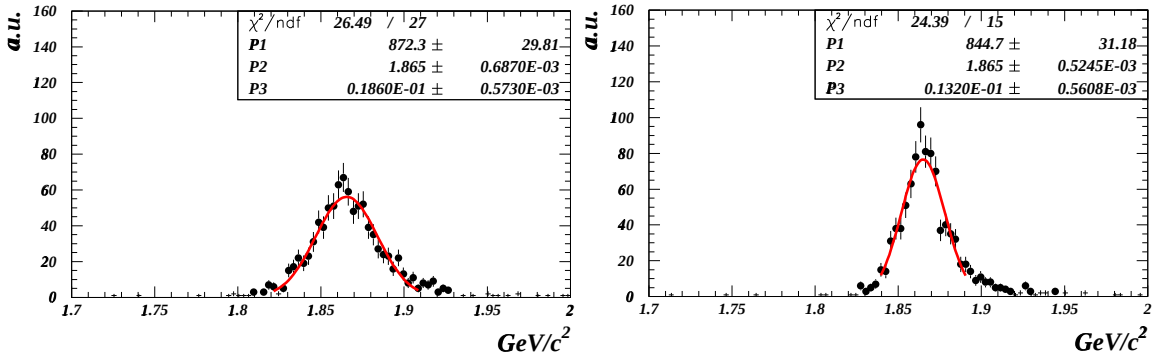

Figure 4.9: *Reconstructed invariant mass of the $K^-\pi^+\pi^0$ system after a 2σ cut on the π^0 mass. The left plot is obtained with measured momenta. The right plot is obtained after a kinematics fit with a π^0 mass constraint.*

erable reduction of the B_d^0 peak width will produce a corresponding improvement of the signal to background ratio, which will ultimately govern the usefulness of this analysis. The background study requires the generation of a very large initial sample of events and has not been performed yet.

For the set of events considered above, the π^0 reconstruction and the kinematics cuts applied give a reduction in efficiency by a factor of 11, which again includes a loss factor of about 3 due to photon conversions. With comparable trigger and charged particle reconstruction efficiency for the channels without or with the π^0, one expects the latter to yield

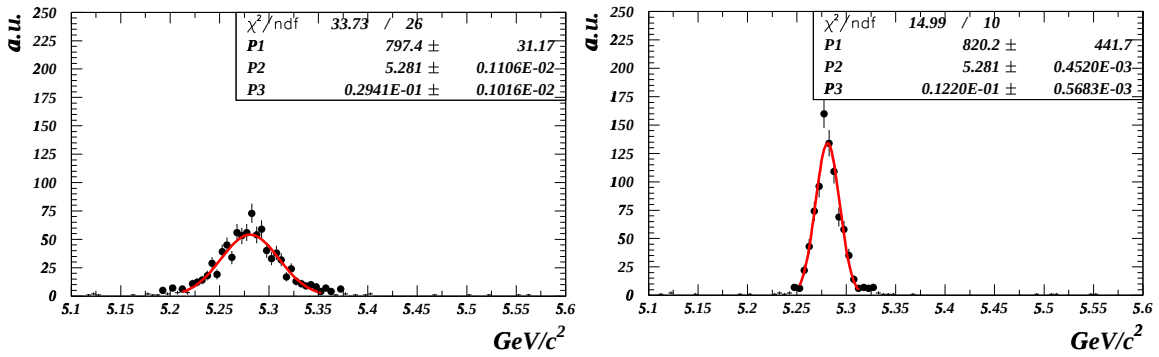

Figure 4.10: *Reconstructed invariant mass of the B_d^0 meson after a 3σ cut on the D^0 mass. The left plot is obtained with the measured momenta. The right plot is obtained after a kinematics fit with π^0 and D^0 mass constraints.*

approximately 1/3 of the event number of the former. The recovery of some converted π^0 photons may substantially increase this number. If the signal to background ratio turns out to be comparable in the two channels, the π^0 reconstruction will appreciably improve the measurement of the unitarity angle γ.

Chapter 5 Technical Design

The LHCb calorimeter system consists of three subdetector components, the scintillator-lead preshower detector (PS), the "shashlik"-type electromagnetic calorimeter (ECAL), and the scintillating tile hadron calorimeter (HCAL). It is the special feature of this calorimeter system that all subdetectors have a similar technology with scintillating tiles as active material that are readout via wavelength-shifting fibers, and using lead or steel plates as absorber material. The optics of each subdetector are optimized for fast signal transmission and are readout in one bunch crossing of 25 ns. The similar technology of all subdetectors allows to use an identical 40 MHz readout electronics for ECAL and HCAL and a very similar electronics for the preshower detector.

As can be seen from Figure 5.1, the calorimeter system starts at z=12.3 m from the interaction point and occupies a total available space of 2.69 m along the beam pipe, between the first and second muon chamber. All three subdetectors can be retracted perpendicular to the beam axis from their data-taking position into a garage position in order to allow access to each individual detector. The preshower detector is hanging from the top and can be opened perpendicular to the beam axis by sliding away curtain-like strips. The ECAL and HCAL detectors are split in two halves and positioned on platforms that can move apart on a rail system. The front-end readout electronics are positioned on platforms on top of the calorimeters such, that the preshower and ECAL crates move out together with the ECAL detector and the HCAL crates accordingly with the HCAL detector when the calorimeter system is opened up.

The detector acceptance and lateral segmentation of the three subdetectors are matched geometrically in a pseudo projective way to facilitate the combination of the information from corresponding readout cells in the trigger processors. The projectivity requirements are determined by the typical shower maximum z-position of electromagnetic showers in ECAL and of hadronic showers in HCAL.

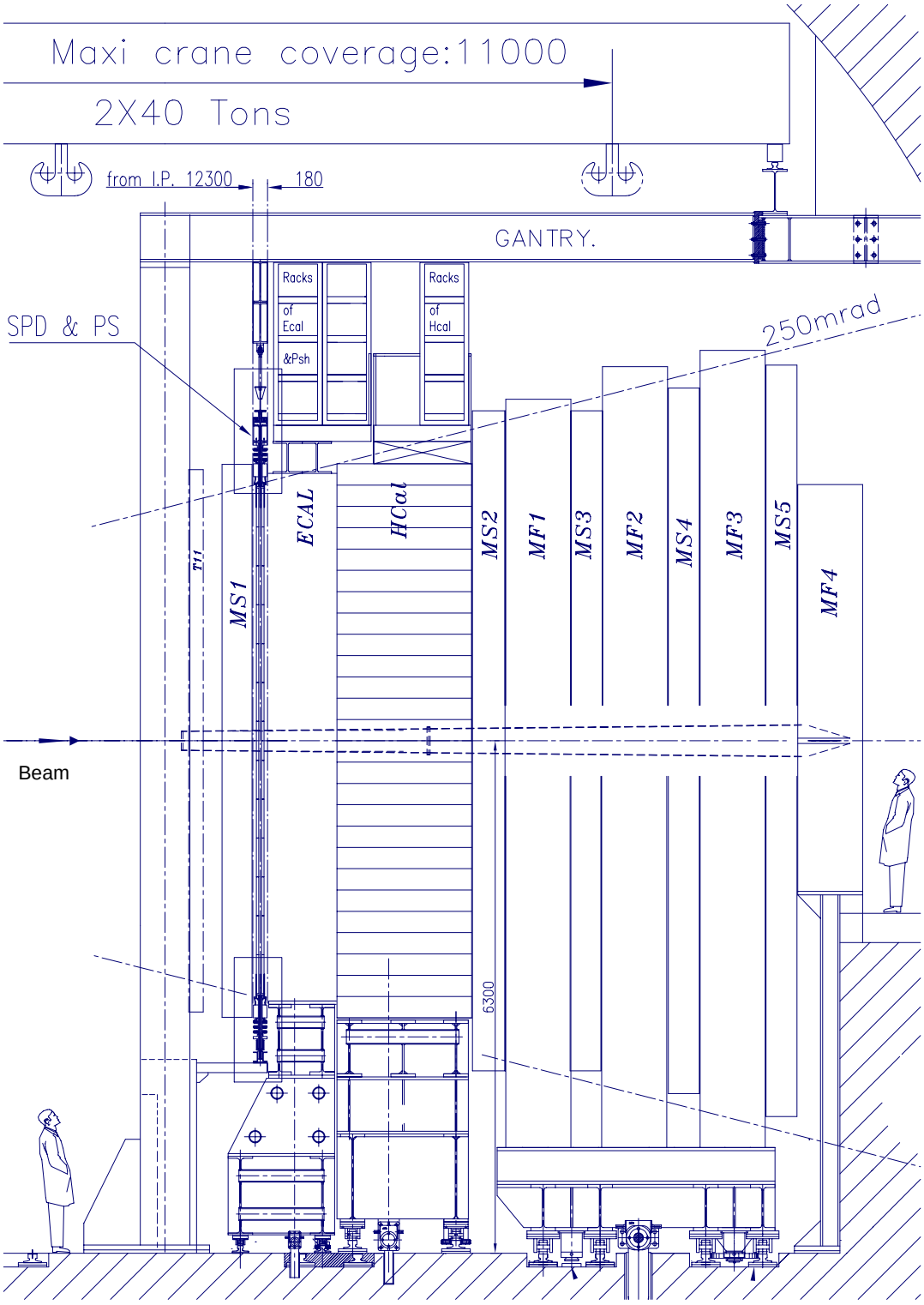

Figure 5.1: *Integration of the calorimeter system in the LHCb detector. The other subsystems are shown schematically only.*

5.1 The pad/preshower detector

5.1.1 Overview

The pad/preshower (SPD/PS) detector uses scintillator pad readout by wavelength-shifting (WLS) fibers that are coupled to multi-anode photomultiplier tubes (MAPMT) via clear plastic fibers. The specific features of the SPD/PS detector are the rather high granularity in the inner part of the detector, and the use of 64 channel photomultiplier tubes with small pixel dimension of 2 mm × 2 mm. The choice of a MAPMT allowed to design a fast, multi-channel pad detector with a reduced cost per channel.

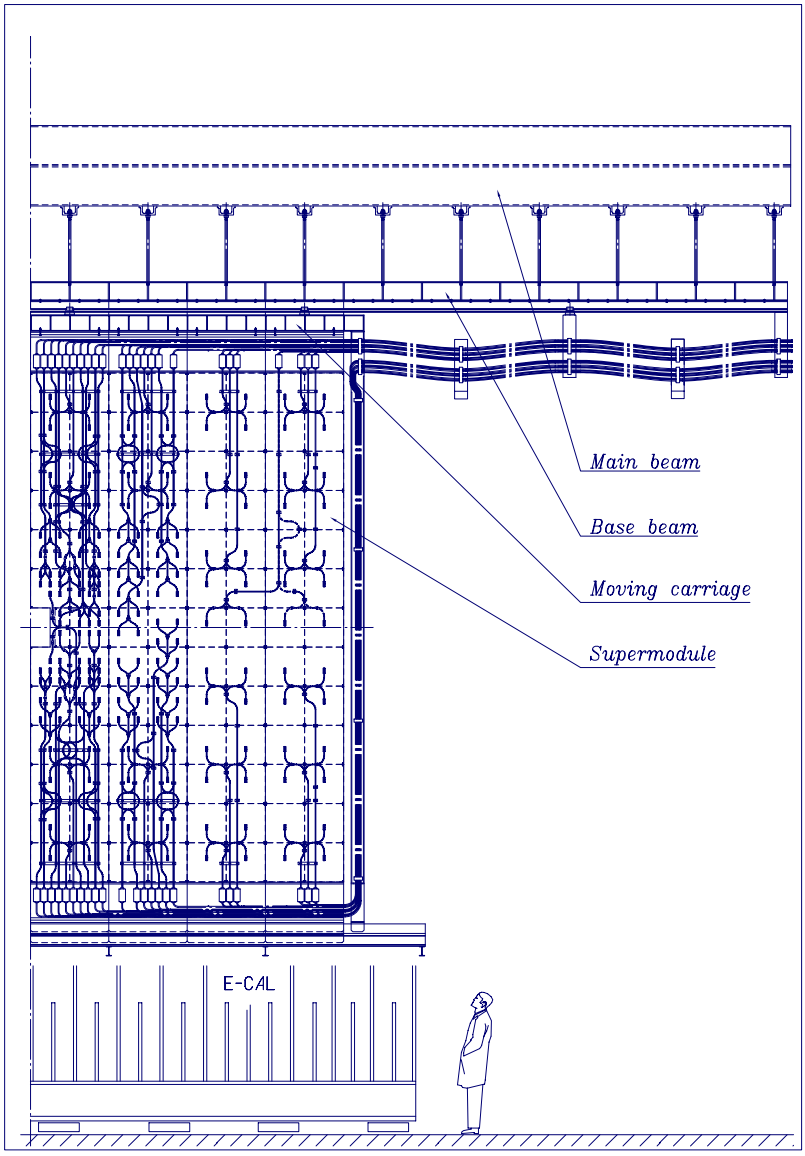

Figure 5.2: *The layout of one half of the SPD/PS detector. The optical and signal cable routing is shown.*

The layout of the SPD/PS detector is shown in Fig. 5.2. It consists of a lead converter

that is sandwiched between two almost identical planes of rectangular scintillator pads of high granularity with a total of 11904 detection channels. The sensitive area of the detector is 7.6 m in width and 6.2 m in height. Due to the projectivity requirements, all dimensions of the SPD plane are smaller than those of the PS by ≈0.45%. The detector planes are divided into two parts, each of them can slide independently on horizontal rails to the left and right side in order to allow service and maintenance works. The lead converter in between the SPD and PS detector planes has a thickness of ≈2 X_0 (12 mm), and is not movable. The distance along the beam axis between the centers of the PS and the SPD scintillator planes is 56 mm.

The arrangement of cells is a one to one projective correspondence with the ECAL segmentation. Therefore each PS and SPD plane is subdivided into inner, middle and outer sections with approximately 4×4, 6×6 and 12×12 cm^2 cell dimensions (see Table 5.1). The scintillator thickness is 15 mm.

Table 5.1: *Basic geometrical parameters of SPD/PS planes.*

Region	Dimensions of SPD (cm)	Dimensions of PS (cm)	SPD cell size (mm)	PS cell size (mm)	Number of cells (PS+SPD)
Inner	190.5 x 143	191.4x 143.5	39.66	39.84	1472 x 2 = 2944
Middle	381 x 238	382.7 x 239	59.5	59.76	1792 x 2 = 3584
Outer	762 x 619	765.5 x 622	119	119.5	2688 x 2 = 5376

The cells are packed in ≈48×48 cm^2 boxes (detector units) that are joined into supermodules. Each supermodule has a width of ≈96 cm, a height of ≈6.5 m and consists of detector units that form 13 rows and 2 columns.

The space reserved for the SPD/PS detector between the first muon chamber and the electromagnetic calorimeter is 180 mm only, and made the conceptual and technical design a challenge. In the following we discuss the design of the scintillator cells and of the fiber system, the design and assembly of the detector unit and of the supermodules, the installation of the overall pad/preshower detector, the calibration system, and the quality control procedures [6].

5.1.2 Design of the scintillator cells and the wavelength-shifting fiber system

The granularity of the SPD/PS detector is determined by the segmentation of the ECAL and the projectivity requirements. Therefore the SPD/PS scintillator planes are subdivided into three regions: inner, middle and outer, each having a different pad size. The scintillator size of the SPD is identical to the one of the PS, and the cell size differs only by the thickness of the scintillator-pad wrapping paper and by the thickness of the detector-unit walls.

Figure 5.3 shows the geometry of an individual scintillator pad with the WLS fiber layout. The basic plastic component is polystyrene to which primary and secondary wavelength shifting dopants (PTP, 1.5% and POPOP, 0.04%) are added. The square structure

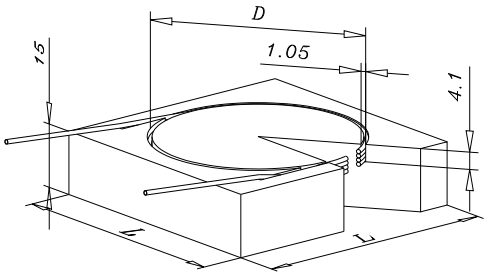

Region	L,mm (SPD)	L,mm (PS)	D,mm
inner	39.2	39.5	37
middle	59.0	59.4	56
outer	118.4	119.1	110

Figure 5.3: *Scintillator cell design.*

of a pad is cut out from a 15 mm thick scintillator plate, and the scintillator surface is polished to reach the necessary optical quality. In order to maximize the light collection efficiency, WLS fibers are coiled and placed into a ring groove that is milled in the body of the cell using a CNC machine. The cross section of the groove has a rectangular form with 4.1 mm in depth and 1.1 mm in width. The groove is filled with 3.5 loops of WLS-fiber. The number of loops was chosen to achieve an overall optimization of the light collection efficiency [17] and the duration of the time response [39]. Two additional grooves are milled to the scintillator to allow the WLS fiber to enter and exit the plate. The fiber is glued inside the groove by BC-600 glue from BICRON [19] using a dedicated semi-automatic device that provides a winding of the fiber and a uniform glue filling along the groove.

The present baseline option in the fiber choice is the 1.0 mm diameter Y11(250) multi-cladding S-type WLS fiber from KURARAY [18] as a reasonable compromise between light output and durability. The S-type fiber is easier to bend and more resistant to cracking [20], that is very important for the pad design, in particular for the smallest pads in the inner region. Before being inserted into the groove, the WLS fibers are cut off to the proper length according to the diameter of the circular groove. Then the fiber is glued into the scintillator and the pad is wrapped with 0.15 mm thick TYVEK or Teflon tape in order to improve the light reflection and to minimize the dead space between adjacent pads.

Light produced by an ionising particle inside the scintillator is absorbed by the WLS fiber and the re-emitted green light is guided by total internal reflection to the photo-multiplier tube (PMT). Each single scintillator pad will be individually read out from both ends of the WLS fiber. The WLS fiber is long enough to extract the light from a cell out of the detector unit box. For the further transportation of the light to the pixels of the multi-anode PMT, a long clear fiber will be coupled to the WLS fiber by optical connectors that are described in detail in [6]. The length of clear fibers varies from 0.7

to 3.5 m, however all the fibers that are connected to a particular PMT have the same length in accordance with the front-end electronics specification [13, 14]. The clear fiber allows to transport the scintillator light from the SPD/PS planes over a few meters to the multi-anode PMT without significant attenuation.

5.1.3 Design and assembly of a detector unit

The scintillator cells are grouped into self-supporting detector units that will be packed inside a square 476 mm × 476 mm (SPD) and 478 mm × 478 mm (PS) box, yielding a total of 26 boxes per supermodule. Since there are three sections with different cell sizes for the SPD/PS planes, the boxes will be filled with a different number of pads with sizes that add up to 119 mm for the SPD to 119.5 mm for the PS planes.

A special technology of box manufacturing was developed in order to obtain stiff boxes with a minimum amount of material between the adjacent cells of neighboring boxes. The mechanical structure of the box is shown in Fig. 5.4. The frame of the monolithic box is manufactured using carbon-fiber reinforced plastic (CFRP) with a thickness of the lateral wall of 0.25 mm. This fabrication method was developed in INR and consists of one cycle of polymerization process with defined curing parameters. Two prototypes of SPD/PS detector units were assembled using boxes that were made entirely from CFRP, and that were successfully tested during 1999 beam tests [17]. For reasons of cost, only the lateral walls of the box will be made from CFRP, while the top and bottom covers are made from ≈2 mm thick aluminium or plastic plates. The assembly elements are made from plastic too and are glued to the lateral walls. The bottom cover is glued to the CFRP frame by epoxy and the top one is fixed by screws (Fig. 5.4). On the top cover there are output plastic ports disposed to allow the fiber bundles to exit the box. They are made from plastic using a cheap pressure die-casting technology. A light-emission diode power-supply connector for the calibration system (see section 5.1.6) is also fixed on the surface of the top cover.

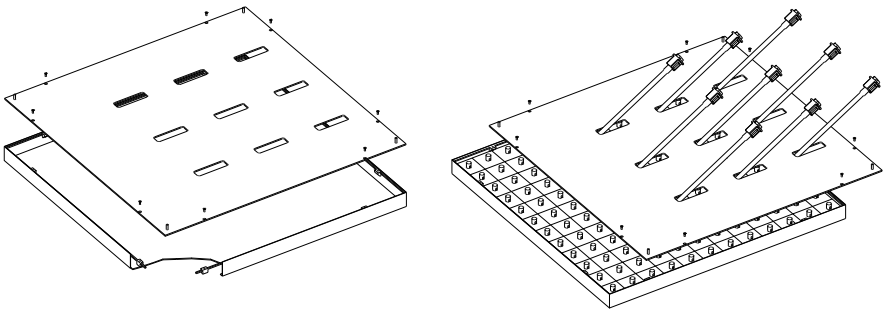

Figure 5.4: *Design of the module box.*

The cell/fiber layout inside the box is designed such that all WLS fibers in one detector unit have identical length. All cells in a detector unit are grouped in matrices of 4×4 cells, and the fibers from each matrix are collected in one bundle that ends in one optical connector. The routing of fibers inside a box from one matrix is shown in Fig. 5.5. The

bending diameter exceeds 100mm. To minimize the light losses from the cell to the optical connector, as an option, one could replace one part of the WLS fiber of ≈50 cm length by a clear fiber that is spliced to the WLS fiber. In this case the length of the WLS fiber extending out of the scintillator would reduce to less then 10 cm. The decision on this option will be done after testing prototypes in the years 2000-2001.

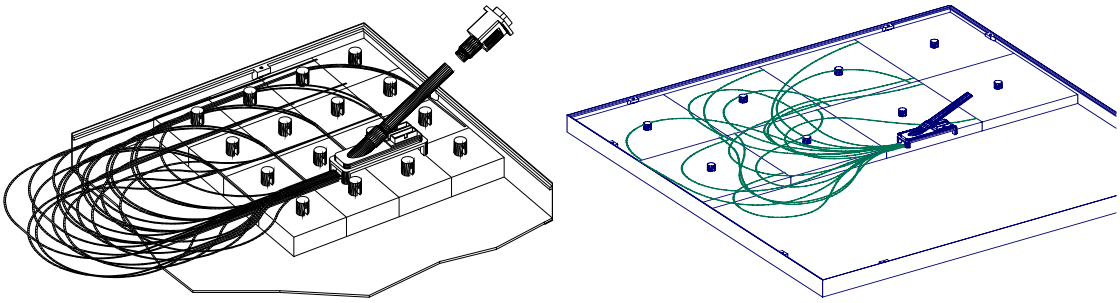

Figure 5.5: *Fibres routing inside the inner (left) and the outer (right) module box with pads.*

The module assembly procedure is as follows: the scintillator pads with glued WLS fibers are placed into the box after quality control tests. The fiber ends are grouped by 32, inserted into a light-tight flexible tube and gathered to an optical connector. The fiber ends will then be inserted and glued into the optical connector, before being cut and polished. Depending on the number of scintillator cells inside a unit, the boxes are equipped with one (outer region), four (middle region) or nine (inner region) output port(s) and light connector(s).

The detector units are designed to be mounted on a supermodule support plate with screws, prior to lifting them to the operation position.

5.1.4 Design and assembly of a supermodule

The supermodules of the SPD/PS planes have identical design. Each supermodule consists of 26 detector units mounted on a long aluminium strip in two columns. The photomultiplier tubes are disposed on both, top and bottom ends of the supermodule support outside the detector acceptance.

The detector units are connected to the PMTs by optical cables that consist of bundles of 32 clear fibers, enclosed in a light-tight plastic tube. Depending on the position of the detector units inside the supermodule, the length of clear cables varies from 0.7 to 3.5 m. Care is taken that the cables going to the same PMT are of equal length. The trace scheme of optical cables is shown in Fig. 5.2.

One end of the cable is equipped with an optical connector that is plugged to the connector of the detector unit. The other end of the optical cable is grouped by four fiber ends and gathered to one PMT by means of a photo-tube coupler that is shown in Fig. 5.6. The fibers are inserted into the corresponding holes of the optical coupler that holds the fiber ends in contact with the window of the multi-anode photomultiplier. After gluing the fibers to the coupler, the fiber ends are machined and polished. The holes are

organised in a precise matrix to fit to the PMT window in such a way, that the two fiber ends of one cell are aligned properly to the diagonal of the corresponding pixel of the compact multi-anode photomultiplier tube (MAPMT) R5900-M64. This 12-stage tube is manufactured by Hamamatsu [23] and has a bialkali photocatode that is segmented in 64 pixels of 2×2 mm^2 each. The precise alignment of the coupler matrix relative to the pixels of the MAPMT is accomplished by using reference marks on the tube and a dedicated alignment tool, that is under development.

The coupler holder and PMT-cookie assembly are disposed within a housing box (see Fig. 5.7) that provides mechanical protection, light-tightness, and shielding of electrical and magnetic fields. The final design of the PMT housing will be chosen in accordance with the electronic-card dimensions, the available space, and the required magnetic-field protection. The details of different PMT-housing variants are discussed in [6].

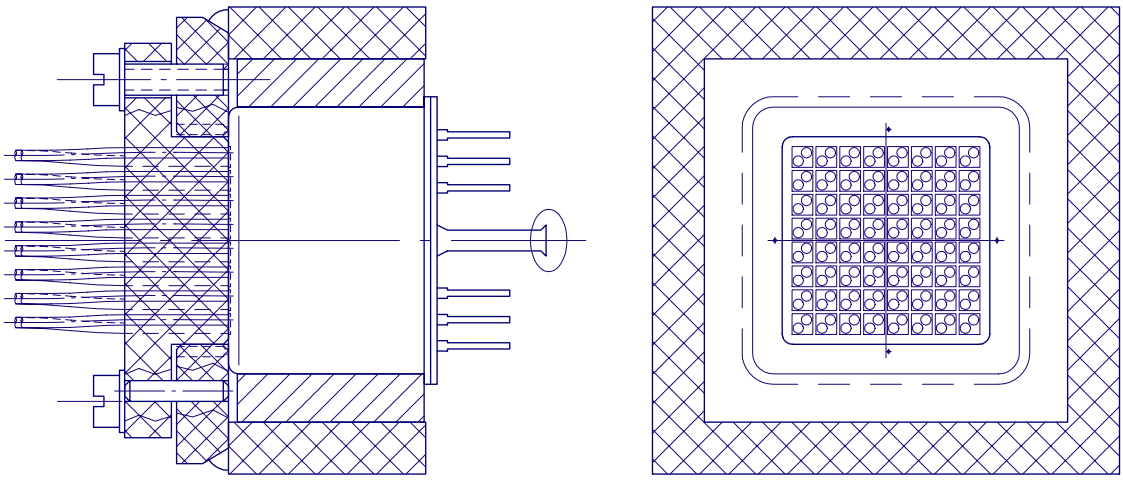

Figure 5.6: *View of fibers-to-PMT optical coupler.*

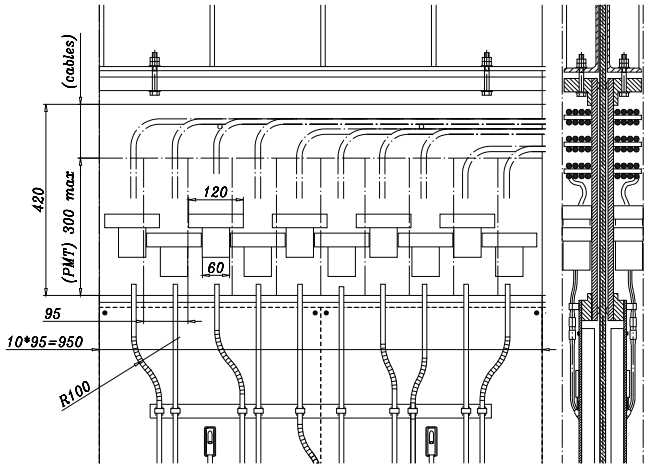

Figure 5.7: *A possible layout for the photomultiplier tubes.*

The assembly of supermodules is organized in such a way that a maximum of operations (i.e. the mechanical assembly, the cabling and the control) can be realized at an installation area, leaving only the connection of signal cables to be done after the supermodule has been installed at its position of operation on the detector support. The assembly, transportation and installation of the supermodules is done with a special support cradle. All stages of assembly of a supermodule are discussed in detail in [6]. It is assumed that all stages of the assembly can be performed in close proximity to the LHCb experimental zone with accessibility to a crane. The space requirements to the assembly area are 12×10 m^2, and the estimated time for both, the lead and supermodules assembly is 4 months.

5.1.5 Installation of the detector

The assembly of the SPD/PS detector starts with the installation of the lead converter, that will be mounted on the base support beam (see Fig. 5.2). The lead converter wall is constructed from eight independent strips that are 12 mm thick, 1 m wide and 7.9 m long. From both sides 0.5 mm thick stainless steel sheets are glued onto the lead under pressure. The manufacturing tolerance for the thickness of the lead sheets is typically 0.1 mm. The strip size is chosen for a convenient manufacturing and to allow the assembly by crane inside the experimental hall.

Before transportation to the operational zone the lead strip is secured on a support cradle. It then is lifted by a crane and transported to the place of installation, where the I-beam on top of the lead strip is fixed to the base support beam by bolts (left side of Fig 5.8). On the base support beam there is a set of tuning bolts that are connected with the main beam to correct for possible deformations. To avoid the swing-effect, the bottom ends of strips are inserted between two channel beams disposed at the bottom of the support frame. After the channel beams have been bolted to the I-beam, the support cradle is dismounted from the lead strip and may be used for installation of the next strip. After installation, all lead strips are joined together with a flat hinge. The rails are mounted on the structure channels on top of the lead strips.

The procedure to assemble the supermodules is very similar to the one described above for the lead converter. Before the installation, a support cradle will be temporarily attached to the supermodule support in order to allow the supermodules to be moved to the operation position (right side of Fig 5.8). The supermodules are mounted on separate moving carriages that are installed on rails disposed along the base beam, and that can be moved in the horizontal direction. After assembly, the detector parts can be rolled to their final position. The routing of the signal cables is made flexible to allow the detector to move without disconnecting any cables. When the SPD/PS detector is installed in its working position, the surrounding space is rather limited so that only the perimeter of the support frame can be reached during short access periods. Therefore during repair or maintenance interventions each half of the detector will be moved into a garage position along the main support beam.

The detailed dimensions and weights of the preshower components that have to be installed are summarized in Table 5.2. The total weight of scintillator material to be mounted on the SPD/PS planes is $\approx$1'500 kg, and the total area to be covered by scin-

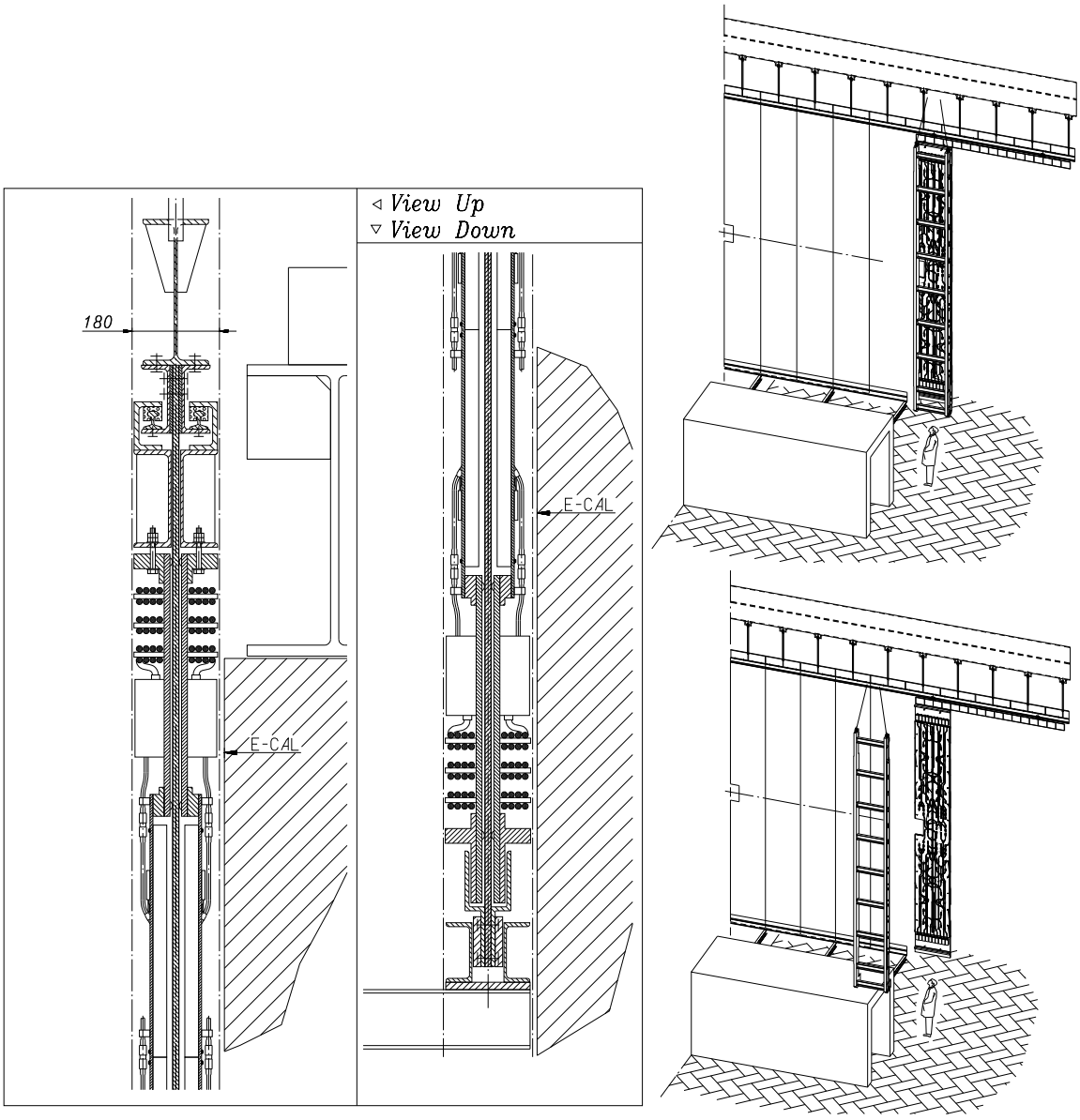

Figure 5.8: *Figure on left: Upper and lower parts of SPD/PS detector along the beam axis. Figure on right: Assembly of SPD/PS detector.*

tillator cells for both SPD/PS planes is ≈94 m^2. A square hole of 48×48 cm^2 will be introduced in the central part of the detector to accommodate the beam pipe. The total weight of the 12 mm thick lead converter fixed in between the PS and SPD planes is about 8'200 kg. In comparison, the weight of the movable (one half) detector plane, is ≈1'600 kg.

5.1.6 The calibration system

Several options for calibrating and monitoring the SPD/PS system are still under consideration and are discussed in detail in [6]. Important tasks of the calibration system are

Table 5.2: *Main parameters of mechanical structure.*

Structure	Material	Z-X Cross-section	Y-Length	Weight,kg
Detector + Support				**19,570**
Main Support Beams	Steel	200 cm^2	19 m	2,900
Base Beam	Steel	90 cm^2	19 m	1,300
Lead wall	Lead	12 $mm \times 7.9$ m	7.7 m	8,200
$4 \times 1/2$ detector		2×7 $cm \times 7.7$ m	7.6 m	6,320
lower support beam	Steel	124 cm^2	9 m	850
1/2 Detector		7 $cm \times 7.7$ m	3.8 m	**1,580**
Carriage	Steel	24 cm^2	4.5 m	80
4 supermodules		7 $cm \times 7.7$ m	4×96 cm	4×374
Supermodule		7 $cm \times 7.7$ m	96 cm	**374**
Support Strip	Al	6 $mm \times 6.7$ m	96 cm	106
PMTs Support Plates	Steel	225 cm^2	96 cm	164
2×13 detector units				26×4
Whole Scintillator	Sci	2×15 $mm \times 6.2$ m	7.6 m	**1,500**

to provide a precise timing reference for the inter-channel synchronization and to monitor the stability of the photomultipliers. Among the different systems based on laser, UV lamp and LEDs, the latter looks most attractive due to its high modularity, lack of moving parts and high performance.

In order to provide a relative synchronization of all channels, a fast LED response is needed to reproduce a typical particle signal in the fast electronic chain. Two different LED monitoring systems are under investigation for the preshower detector. One system is based on the prototype designed for the ALICE PHOS detector [46]. Each cell is illuminated by one LED with the control unit located in a rack on top of the detector, and with the LED driver printer circuit board (PCB) positioned near to the detector unit. The control unit and LED driver are connected by a flat cable thus minimizing the number of cables to the movable detector wall. The ALICE prototype was designed to be used with slow electronics and would need modifications to the output chains of the driver. The other solution would use a single LED to illuminate a number of cells. In this case the LED and the light mixer are installed on the support structure outside the detector unit. Clear fibers from the light mixer go into the detector-unit box where the second light mixer redistributes the light to the particular cells. The number of cells for half of the SPD/PS wall is 2976. If the driver has 64 outputs, then the mean number of channels fired by one LED is less than 50.

In order to monitor the stability of the photomultipliers it is essential to control their gain by sending a fixed proportion of light to each photocathode. The current mapping of the optical cables from the PS and SPD to the MAPMT does not leave any free channels for calibration purposes. Fortunately one does not need to illuminate the MAPMT pads individually. A global illumination can be performed by passing a few clear fibers through

a light diffusion box (one per PMT) that is equipped with a green emitting LED. The fibers are illuminated either by equipping every diffusion box with its own light pulser, or by distributing light pulses from one common light source through clear optical fibers. In the latter case monitoring of the light source itself could be done in a simple way with a PIN photo-diode.

The width of the LED signal spectrum, that is defined by the photostatistics, provides an absolute scale for the detector response and can be used to control the linearity of the readout chains.

5.1.7 The quality control

In order to guarantee the same quality of all preshower cells and to identify a degradation in quality at the earliest possible production level, it is foreseen to monitor the quality of all SPD/PS subcomponents at every step of fabrication. This starts from the analysis of raw materials up to the final certification of each scintillator cell before assembly. A detailed list of all stages and appropriate procedures that are foreseen to monitor the cells production is given in [6].

The plastic scintillator material will be delivered from one manufacturer in a few ingots. To monitor the light output from different ingots, small samples of scintillator of fixed dimensions ($\approx$1 cm^3) are cut out, polished and tested with a radioactive source. The transparency of the scintillator and the purity of the raw material are measured on a few cells or for specimens from the same ingot, using chemical analysis techniques.

After the mechanical processing and polishing of the scintillator, each cell is visually inspected to exclude samples with cracks and scratches, and the dimensions are checked to be within the tolerance of $\pm$0.1 mm (3σ).

All fibers must pass an optical test to reject those that could be damaged during transportation or unpacking. The optical tests must be fast, reliable and easy to handle. Therefore it is intended to use LED in conjunction with PIN diodes to measure the transparency of fibers. Similar devices called "optical power meters" (OPM) are routinely used to check out optical cables and connectors for optical networks. They are portable, can be used in situ, and provide a typical accuracy of 3% for a relative comparison. This system could also be used to verify the quality of gluing the fibers into the scintillator groove by injecting blue light into the scintillator cell in sequence from a number of fixed points and reading the light output with the fiber.

Since the quality of light coupling is of great importance when grouping and feeding fibers from 16 tiles (4x4 cell) to the same optical connector, a visual inspection of the optical connectors is foreseen. Furthermore a special cutting and polishing device has been designed to ensure high quality surfaces and therefore a good contact between fibers and connectors.

Once a cell has passed all tests, it is wrapped using white reflective paper (TYVEK) and assembled in a detector unit. It is scanned with a radioactive source to measure the absolute light yield and the homogenity in light yield. The level of cross talks will be measured as well to check for possible light leakage between tiles. A few detector units will be tested in a beam of minimum ionising particles to get a direct comparison with test data from the laboratory.

5.2 The electromagnetic calorimeter

5.2.1 Overview

The LHCb electromagnetic calorimeter (ECAL) uses the "shashlik" technology. It is built from individual modules that are made from lead absorber plates inter spaced with scintillator tiles as active material. Wavelength-shifting (WLS) fibers penetrate the lead/scintillator stack through holes, and are readout at the back of the sampling structure by photomultipliers.

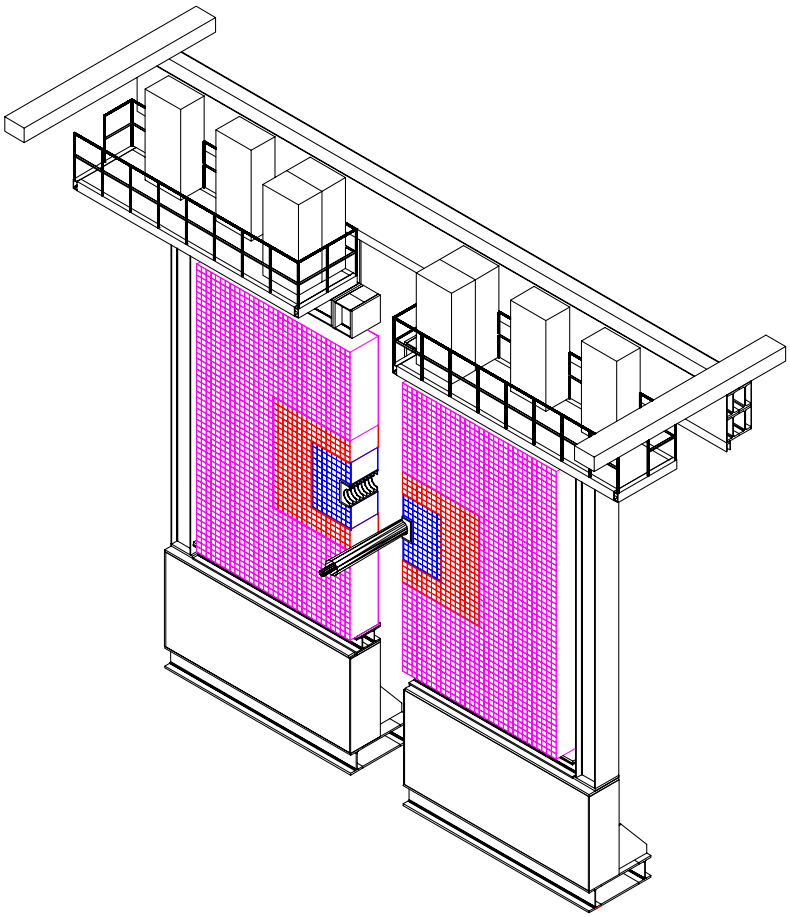

Figure 5.9: *The electromagnetic calorimeter 3d-view from behind the detector towards the interaction point. Shown are the three sections of the calorimeter, the ECAL main platform, and the electronics platform with the racks on the top of the calorimeter wall. Around the beam pipe is drawn the inner supporting frame. One of two ECAL platforms is partially moved out.*

The ECAL structure is segmented into three sections with one type of module per section. The lateral dimensions of the three sections are ±970 mm, ±1939 mm and ±3878 mm in x and ±727 mm, ±1212 mm and ±3151 mm in y for the inner, middle and outer section, respectively. All three types of module have an identical square size

of 121.2 mm, but differ by the number of readout cells. The ECAL section closest to the beam pipe consists of 167 modules containing 9 cells each, the middle section has 448 modules containing 4 cells each, and the 2688 outer-section modules are made from a single cell. The detector is built in two separate halves from individual modules that are positioned in layers on two movable platforms and fixed to a surrounding frame. A global view of the ECAL structure is shown in Figure 5.9. The ECAL starts at z=12.49 m from the interaction point with a total depth along z of 835 mm. The overall dimension of the active area is x=7.8 m and y=6.3 m.

In the following the construction of the ECAL is discussed [4], describing the engineering design of modules, their construction and assembly, and the installation of the ECAL detector in the experimental zone.

5.2.2 Design of modules

The three types of module that build up the inner, middle and outer sections of the ECAL detector have a very similar basic design, as shown in Figure 5.10. All module types have lead absorber plates of identical size, but they differ by the number of cells and therefore by the number of scintillating tiles per module, as well as by the fiber density. A module for the outer section consists of one single square cell of dimension 121.2 mm with 64 fibers running through the lead/scintillator stack. The middle section is made from modules that contain four square cells of dimension 60.6 mm, and the inner section from modules that have nine cells of 40.4 mm size. Both, the middle section and inner section modules are readout through 144 fibers per module.

Each module is constructed from alternating layers of 2 mm thick lead, 120 μ thick white reflecting paper (TYVEK) and 4 mm thick scintillating tiles. In total, there are 66 lead/scintillator layers resulting in a total depth of 25 X_0.

The lead plates are produced using the die-stamping technology. Independent of the module type, all converter plates have identical dimension and differ only by the number of holes that are needed for the traversing fibers. Since the fiber density is the same for the inner and middle module type, only two types of punching dies have to be manufactured.

A scintillating tile is produced of polystyrene-based PSM-115 scintillator with 2.5% p-terphenyl and 0.01% of POPOP admixtures. The concentration of scintillating dopants is chosen such that the scintillation light is almost saturated, and is tuned for the scintillator emission spectrum to match the absorption spectrum of the WLS fiber. The scintillating tile production employs the high pressure injection molding technique. The tile edges are treated chemically to be mat and thus to provide a diffuse reflection in order to improve the light collection efficiency, the transverse uniformity [30], and to prevent tile-to-tile light cross talk.

The light from a scintillation tile is re-emitted and transported by 1.2 mm diameter wavelength shifting (WLS) fibers that penetrate the entire module, and is then read out with a photomultiplier tube (PMT). WLS fibers doped with fast shifter have been chosen as baseline solution. Such fibers are commercially available and are produced by Bicron, Kuraray and Pol.Hi.Tech. We are planning to use more radiation hard [31] fibers for the inner- and perhaps for the middle-section modules than for the modules belonging to the outer section. The choice of fiber will be made in 2001. The fibers belonging to each

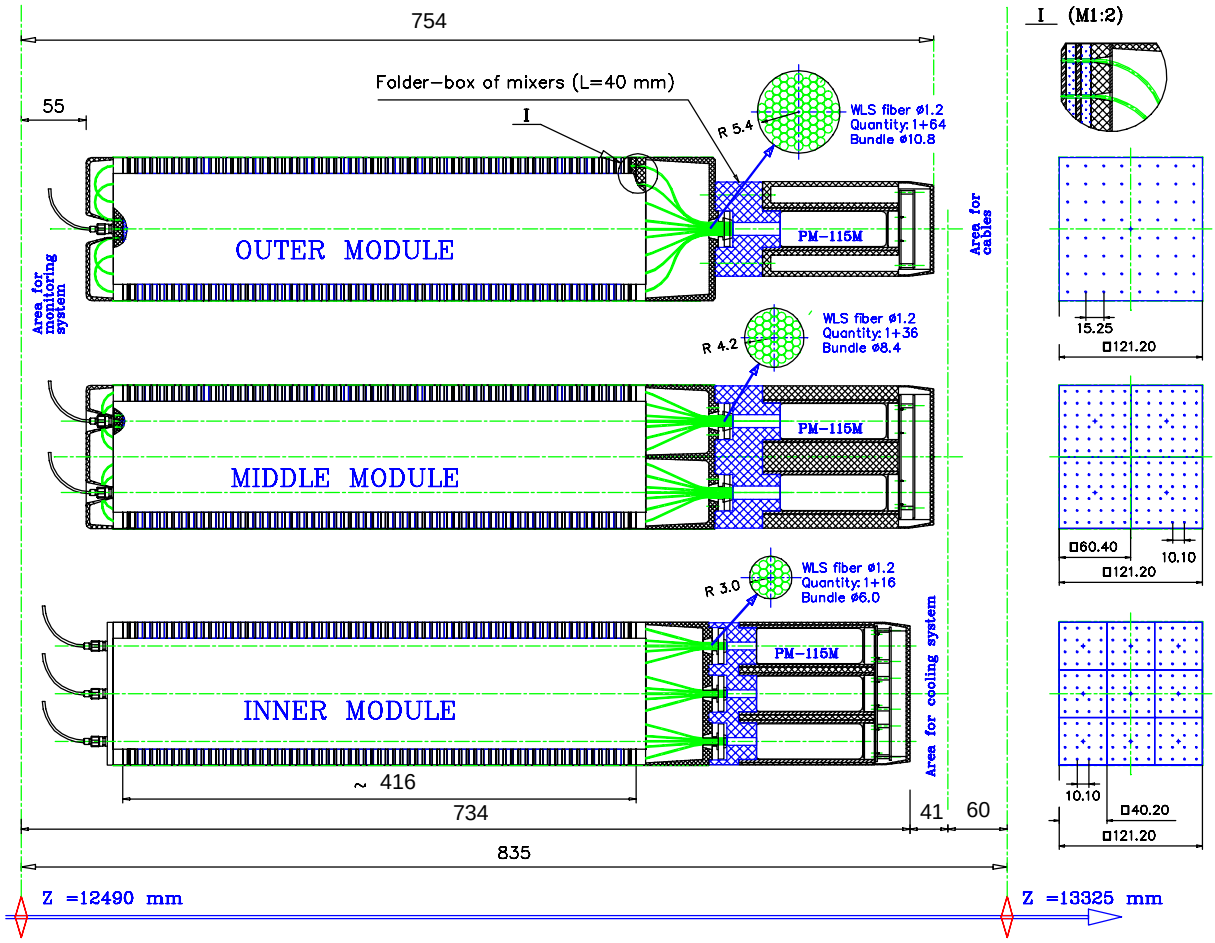

Figure 5.10: *The electromagnetic calorimeter modules for the inner, middle and outer sections. At the monitoring side are shown the transport fibers, connectors, WLS fiber loops (if any) and plastic covers. At the read-out side are shown the fiber bundles, the light mixers, and the PMTs and their bases. As an example the FEU-115M tube is shown. Also shown is the area for splitters, the space for the cooling system and cabling, and the related mechanics. For more details see the text.*

Table 5.3: *Number of fibers per bundle (1 fiber in the bundle is a clear fiber for monitoring) and fiber bundle size.*

	# of fibers in bundle	Bundle diameter, ⊘, $[mm]$
Inner section	$1+16$	6.0
Middle section	$1+36$	8.4
Outer section	$1+64$	10.8

calorimeter cell are bundled at the end of the module and polished. The number of fibers per bundle as well as the size of the fiber bundle is shown in Table 5.3. It has been shown [30], that the reduced fiber density in the outer section modules does not compromise the detector performance. This allows to keep the diameter of all fiber bundles below 11 mm which has some impact on the choice of the photomultiplier tube, as will be discussed below.

WLS fibers that penetrate the lead/scintillator stack are bent with different curvature at the front of the stack, where fiber loops are made, and at the rear of the stack, where the fibers are formed to a bundle. Bending of the fiber at small curvature radii leads to light loss both, due to mechanical degradation because of fiber cracking and due to the change of the light reflection angle governed by the geometrical optics. The latter effect depends on the bending radius that has been studied and optimized by simulation [4]. For the middle and outer section modules a straightforward fiber bending with the radius as small as 15 mm would lead to mechanical fiber damage. In order to avoid such damage, a special technique of fiber bending under high temperature air has been elaborated and successfully applied for the HERA-B and PHENIX electromagnetic calorimeter modules. For the inner section modules the bending radius at the front of the stack is very small. To avoid the risk of mechanical damage the fibers are cut, polished, and the fiber ends are coated with an aluminium mirror.

Table 5.4: *The requirements to the PMT's for ECAL.*

Item	Parameter
Tube length	not more than 75 mm
Photocathode diameter	more than 15 mm
Gain	5×10^4
Quantum efficiency at 490 nm	more than 12 %
Linearity for 20 mA peak current	better than 2 %
Cathode uniformity within 1 cm^2	better than 5 %
Pulse FWHM	less than 10 ns
Long term stability	better than 2 % per 100 hours
Short term stability for $I_A < 20\mu A$	better than 2 %

To reduce the contribution from the photomultiplier cathode non-uniformity to the constant term of the energy resolution, a quadrangular prism light mixer made from polystyrene will be inserted between the end of the fiber bundle and the PMT. The importance and performance of a light mixer was studied with Monte Carlo by simulating the response to a minimum-ionizing particle (MIP) that generates light in a scintillating tile and that is absorbed, re-emitted and transported by the WLS fibers. The non-uniformity of the photocathode was assumed to be 20%. It is shown [4], that the light that is produced in the scintillating tile by the MIP produces blue light that is distributed over all the fibers, and that the fiber closest to the MIP transmits only about 15% of the total light. Therefore the response non-uniformity to a MIP signal is as small as ≈2% without using a light mixer. The simulation shows that the use of a light mixer with a

length of about 3 cm will keep the non-uniformity small with respect to the constant term of the designed energy resolution of 0.8%.

The size of the fiber bundles (Table 5.3) and of the light mixer determines the requirements to the size of the photmultiplier-tube window and to the photocathode uniformity. A large variety of photomultiplier tubes (PMT) from various manufacturers is under test [47] and several tubes have been identified as candidates that fulfill the necessary requirements. Table 5.4 summarizes the specifications for the PMT to be used on the ECAL modules.

5.2.3 Assembly of modules

In order to profit from past experience, the LHCb calorimeter modules will be manufactured at the same production plant in Vladimir where the HERA-B and PHENIX calorimeter modules have been produced. The module assembly is illustrated in Figures 5.11 and 5.12 for the most complicated case of an inner module. It starts from the lead/scintillator stack assembly in the vertical position using well-like tooling as shown in Figure 5.11a. Then the assembled stack is pressed with a force of 500 kg. This procedure is repeated 5 times to reduce to a minimum possible deformations of the structure. Then the stainless steel side tapes of 100 μ thickness are welded to the steel matrix plate.

In the following the WLS and calibration fibers are inserted into the stack structure (Figure 5.11b). At this stage the fibers for outer- and middle-section modules that will form a loop, are already prepared with the thermo-technique. In order to form a fiber bundle the fiber housing is mounted and the fibers are fixed with the tongs (Figure 5.12a). A hot wire cut of fiber ends ensures the fibers to be co-linear and perpendicular to the cut.

Finally the photomultiplier read-out system is mounted (Figure 5.12b). The PMT is placed in the housing with insertion of a 2.5 mm thick steel screen and a μ-metal protection that shields against the magnetic stray field. Depending on the position, and in the worst case, a stray field of approximately 130 Gauss along z and of less than 5 Gauss in x and y is expected in the present design [48]. The PMT base plate is not shown in the figure. To guarantee the light isolation a module end-cup cover is mounted with an aluminium inclusion in the plastic cover that improves the heat dissipation.

From past experience one can expect that as many as ten modules per day could be produced. The production rate for inner section type modules is twice as low, but their amount of 176 is small as compared to the total number of 3312 modules.

5.2.4 Quality control of modules

An important issue in the construction of ECAL modules is the quality control. Already at the production level one has to make sure that the calorimeter modules are manufactured with similar response and with the designed performance. This implies a detailed control at each step of the module production, starting from the input control of raw material up to characteristics studies of the assembled module. A detailed description of the quality control procedure can be found in [49], and only a short summary is given in the following.

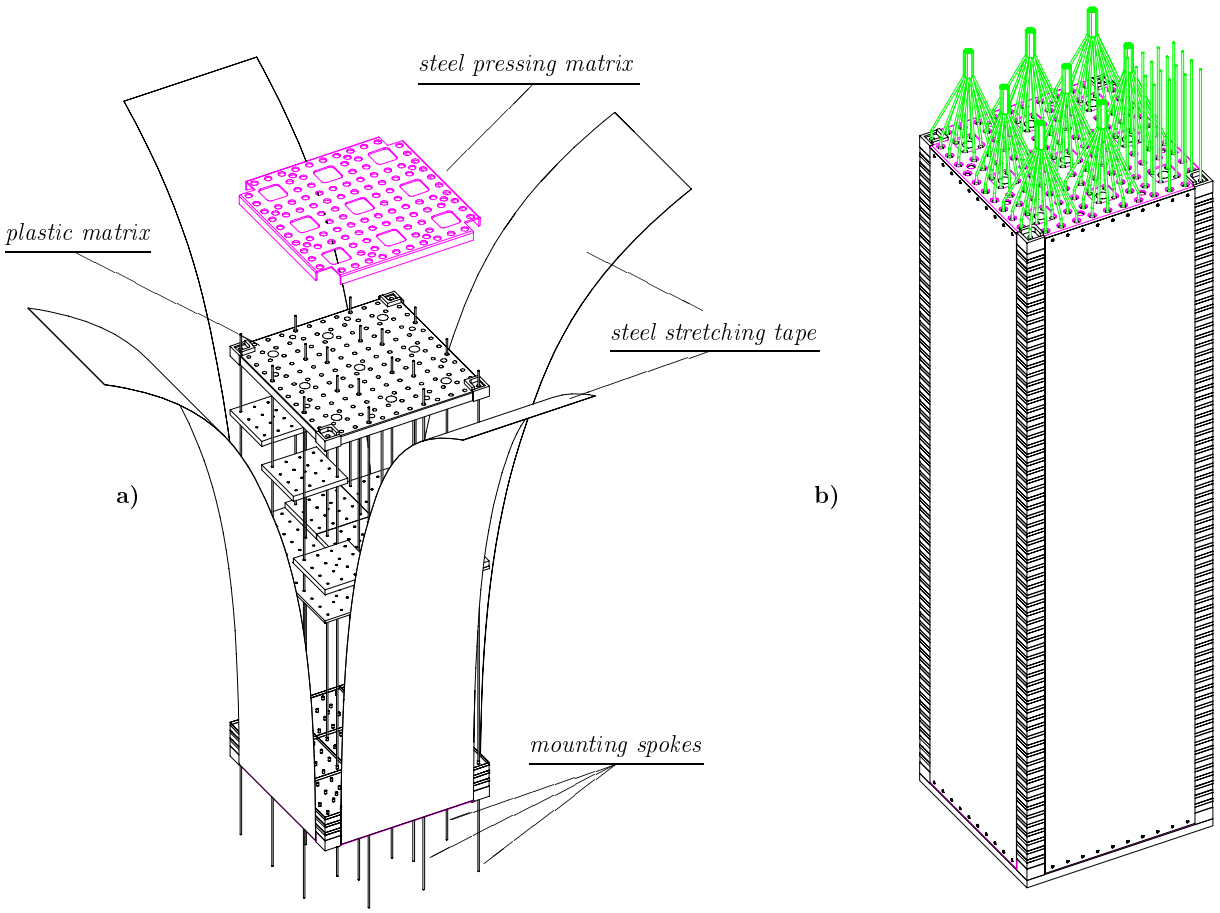

Figure 5.11: *Assembly of the inner section module: shown are a) the Pb/Sc stack during assembly, and b) the assembled stack with welded tape and inserted fibers. For more details see the text.*

The raw material quality control mainly covers the control of polystyrene-based PSM-115 plastic and p-terphenyl. An IR-spectroscopy, the study of transparency for blue (420 nm) light with a spectrophotometer, a gas and liquid chromatography and chemical methods have been developed to control the raw material quality.

In order to measure the scintillator tile quality along with the transparency measurements with the spectrophotometer, a special "hedgehog" test is extensively used. This test studies the tile response to the signal that is induced by a radioactive source. The signal is read out via WLS fibers in the ordinary way with a PMT. The "hedgehog" test is also used to control the quality of tile edge coating.

The final control of the lead/scintillator stack and the fully assembled module is performed with cosmic particles. The modules are tested one by one, placing them in a horizontal position and using the same calibrated PMT for all of them. It has been shown that as many as ten modules can be tested in this way per day with one setup, so that all produced modules can undergo such a cosmic test. In addition, the performance of a small sample of all modules is going to be checked using test beam.

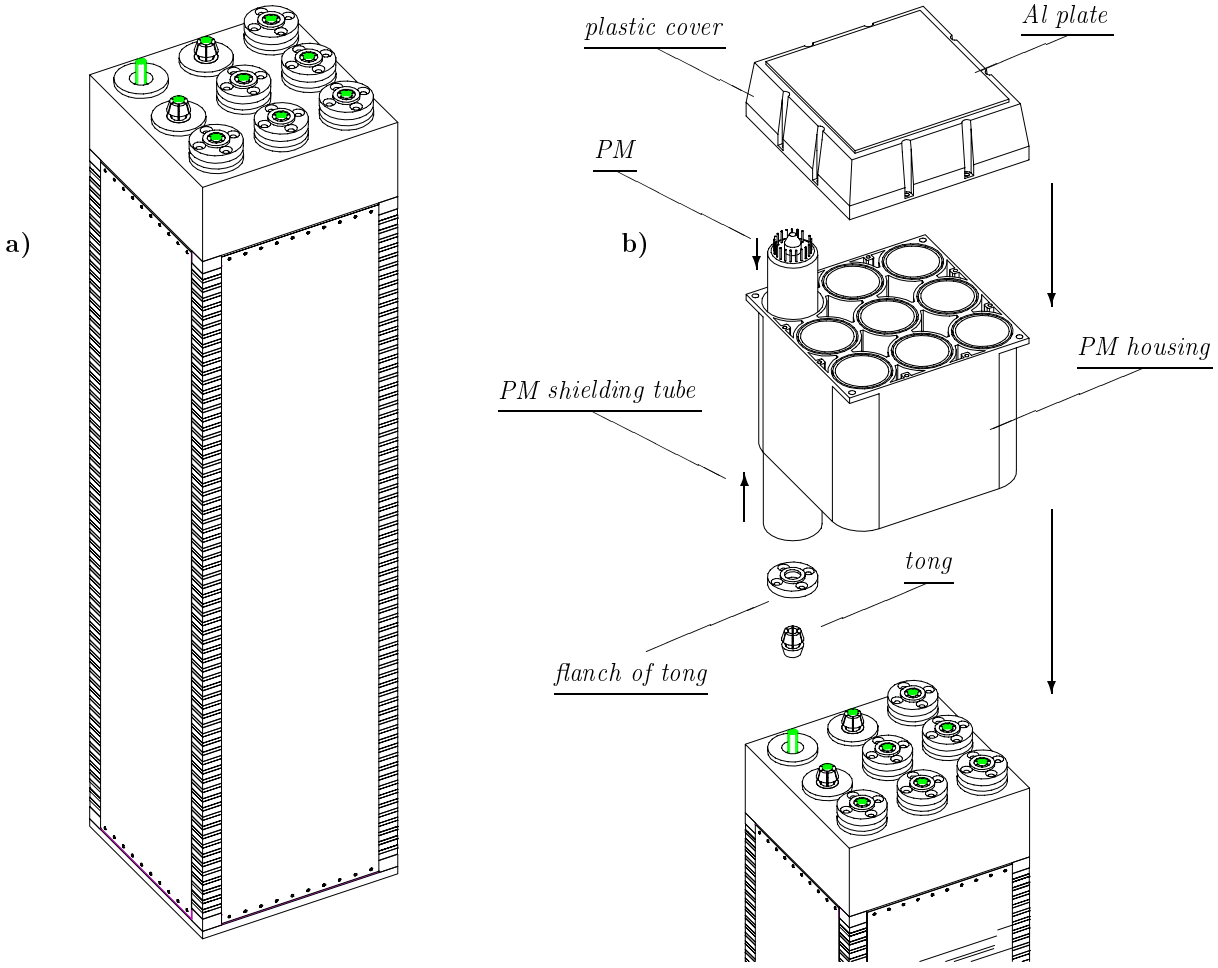

Figure 5.12: *Assembly of the inner section module: shown are a) the assembled stack with 6 from 9 formed fiber bundles, and b) the read-out part assembly. For more details see the text.*

5.2.5 Installation of the ECAL

The design of the overall electromagnetic calorimeter structure is shown in Figure 5.13 and is dicussed in detail in [4].

The weight of an individual module is about 30 kg. The lead/scintillator stack weights about 27.5 kg, and the read-out part (PMT, resistive divider, etc.) plus housing contributes with 2 kg. Therefore the modules can be stacked without use of a crane on top of each other on two movable platforms. The platforms can slide out perpendicular to the beam axis for installing the ECAL, and to allow access to the front and back of the modules as well as to the beam pipe.

When installing the modules on each platform they are grouped together in two horizontal rows that are surrounded by a 250 micron thick stainless steel band. The band is attached to the side-frame and can be stretched to ensure a precise positioning of better than 1 mm and a dense packing of the modules. This system is illustrated in a side drawing of Figure 5.13. It insures a stable overall structure without the need of any frame

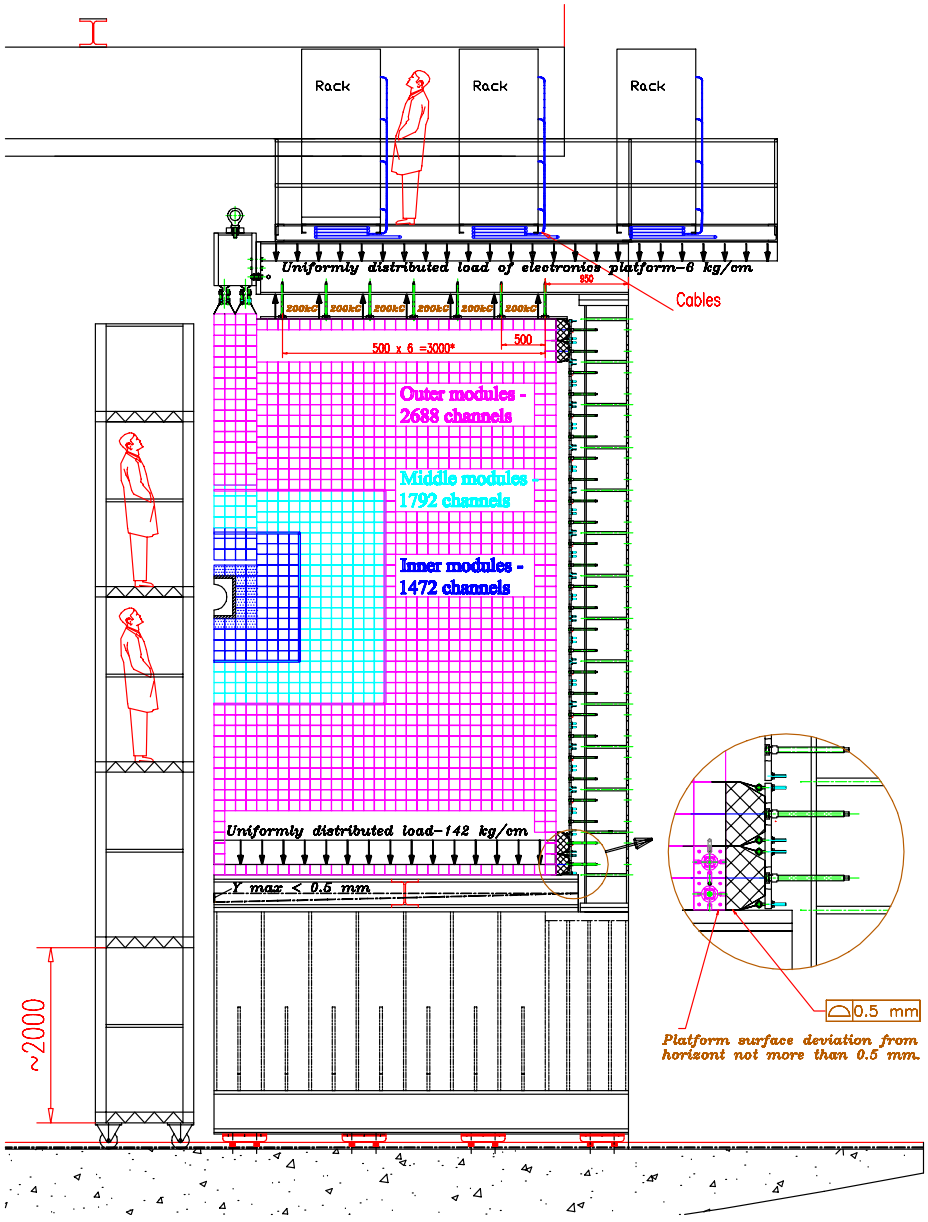

Figure 5.13: *Front view of one of the two platforms of the electromagnetic calorimeter that is moved into the garage position. Shown are the three sections of the calorimeter,the main platform, the main and small inner frames, the electronics platform on the top of the calorimeter wall, and the movable tubular scaffolding. In an enlarged side drawing the mechanics used to tension and precisely position the double-row module structures is shown. Arrows indicate the static load. For more details see the text.*

structure in the inner side of each calorimeter half that would seriously compromise the ECAL performance. The first four columns of modules, that are positioned at the inner side of each half and above the beam axis, are grouped together in double-column stainless-steel bands that are supported from the top. This will allow the replacement of the inner-most modules close to the beam pipe after several years of irradiation, if this should become necessary.

A plate positioned at the top of the ECAL will provide a uniformly distributed load of 1.4 tons onto the modules from the top. A connection to the rail system that supports the preshower detector will ensure the perpendicular stability of the system. The integrated load on each platform is 51 tons.

5.2.6 The calibration system

Even though the final calibration of the ECAL will be done with particles [16], it is foreseen to equip the ECAL with a calibration system that sends a signal directly to the photomultipliers in order to allow for an inter-calibration of the modules readout at the 10% level.

The calibration signal will be initialized either by a 10 ns pulse from a laser, or by a system of $\approx$180 green light emission diodes (LED), that will be placed on the top of the ECAL wall. The signal will be distributed to the front side of the modules with a system of splitters similar to that described in [50], and sent by clear fibers through the modules to the PM. The LED based system will require a one-level 1:40 signal splitting with $\approx$180 splitting units. Thus one LED serves 4 modules in the inner section, 9 modules in the middle section, and 32 modules in the outer section. Alternatively the laser based solution requires a 3-level splitting and $\approx$160 splitters of three different types.

The calibration signal is then delivered via clear optical fibers of 1.0 mm diameter to the front side of each module. The light is transmitted from the transport fiber to another clear fiber with 1.2 mm diameter that penetrates each cell at the cell center via an optical connector and that is bundled in front of the PMT together with the other WLS fibers.

5.3 The hadron calorimeter

5.3.1 Overview

The LHCb hadron calorimeter (HCAL) is a sampling device made out of steel and scintillating tiles, as absorber and active material respectively. The special feature of this sampling structure is the orientation of the scintillating tiles that are running parallel to the beam axis. Wavelength shifting (WLS) fibers are running along the edges of the scintillator tiles that are staggered in depth. Readout cells of different size are defined by grouping together different sets of fibers onto one photomultiplier tube that is fixed to the rear side of the sampling structure. The HCAL is segmented into two sections with square cells of size 131.3 mm and 262.6 mm. The lateral dimensions of the two sections are $\pm$2101 mm and $\pm$4202 mm in x and $\pm$1838 mm and $\pm$3414 mm in y for the inner and outer section, respectively. The optics is designed such that the two different cell sizes can be realized with an absorber structure that is identical over the whole HCAL.

The absorber structure is self supporting and is made from laminate steel plates of various dimensions that are glued together. The periodic structure of the system allows the construction of a large detector by assembling smaller modules. The overall HCAL structure builds up as a wall positioned at a distance from the interaction point of Z=13.33 m with dimensions of y=8.4 m in height, x=6.8 m in width and z=1.65 m in depth. The structure is divided along x into two symmetric parts that are positioned on movable platforms, to allow access to the detector. Each half is built from 26 modules that are piled up on top of each other in the final installation phase. To facilitate the construction of modules, each module is sub divided into eight sub modules that have a manageable size for being assembled from the individual absorber plates. A total of 416 submodules have to be produced to form 52 modules that will built up the two halves of the HCAL structure.

The mechanical structure is completely independent from the optical instrumentation. Therefore, a module that is robust and manageable in size and weight can be shipped from its place of production near to its final destination before being equipped with scintillators and fibers.

In the following the construction of the HCAL is discussed [7], describing the design and assembly of submodules, the construction of modules, the optics instrumentation of modules and the installation of the overall HCAL.

5.3.2 Design and assembly of submodules

The absorber structure of a submodule is a laminate of steel plates with a repetition of identical periods of 20 mm thickness. One period consists of two 6 mm thick master plates with a length of 1283 mm and a width of 260 mm that are glued in two layers to eight 4 mm thick spacers of 256.6 mm width and variable length. The tolerance requirements to the thickness of the low carbon laminate steel of type Fe-360 is $\pm$0.05 mm. In between the spacers a space of 200 mm is left for each of the four scintillating tiles per layer that are inserted at a later stage. The layout of one period is shown in Figure 5.14.

In the design of the master and spacer plates care has been taken to minimize the

number of plates with different shape and dimension in order to reduce the amount of tooling that is needed for their production. The preferred production technology for all plates is die stamping. The most demanding tool is the die for producing the relatively long and thick master plates. Only one die has to be manufactured since one single type of master plate is used for the whole HCAL structure. The number of small dies for spacer plate production is also minimized using four identical plates per period for the central ones.

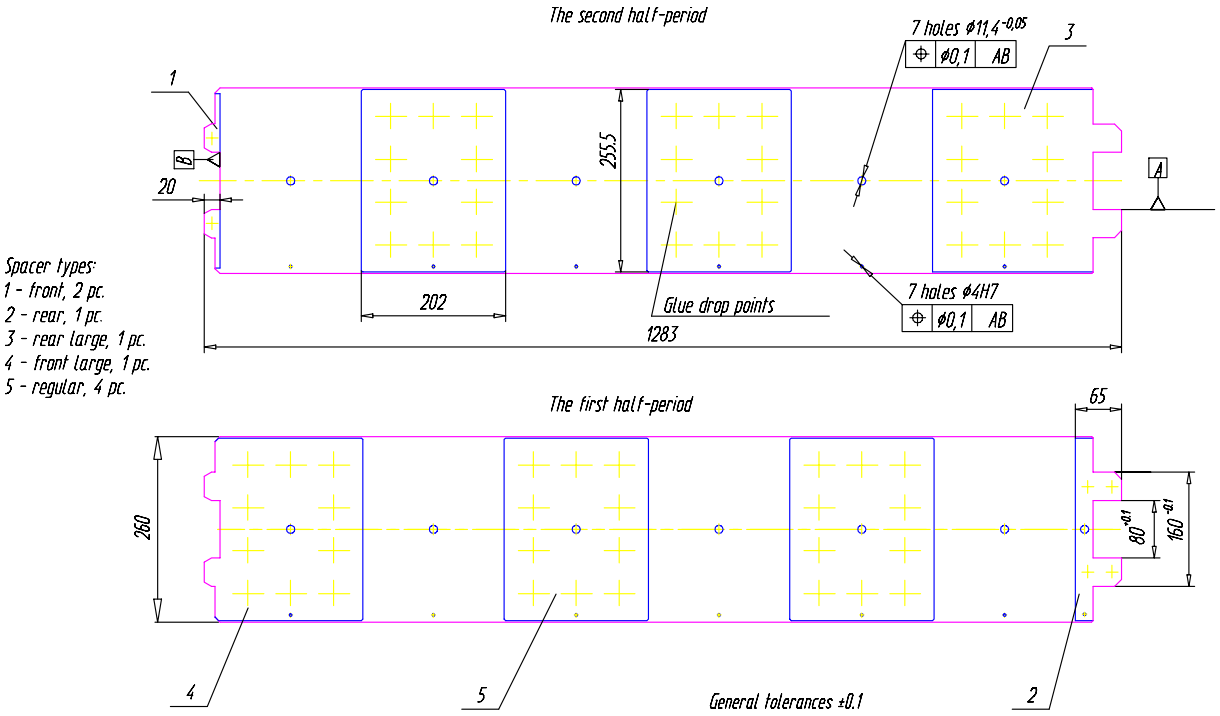

Figure 5.14: *The spacer layout for one period of two master plates.*

The overall structure of one submodule is illustrated in 5.15. The overall dimensions of one submodule are x=525.2 mm wide, y=262 mm high and z=1286 mm deep. The ratio of steel to scintillator is 5.5:1 and the total depth of a submodule amounts to 5.6 interaction lengths.

One submodule consists of 26 identical periods. In order to assemble one submodule the master plates and spacers are stacked in a special submodule assembly tool (see Figure 5.16). The top figure shows the stacking procedure of masters and spacers. The assembling procedure is as follows:

- preparation of masters and spacers including a visual quality check
- cleaning of surface by de-greasing masters and spacers in a bubbling bath using detergent before drying all plates with hot air
- applying manually drops of epoxy glue on well defined areas of the masters and spacers by means of a syringe

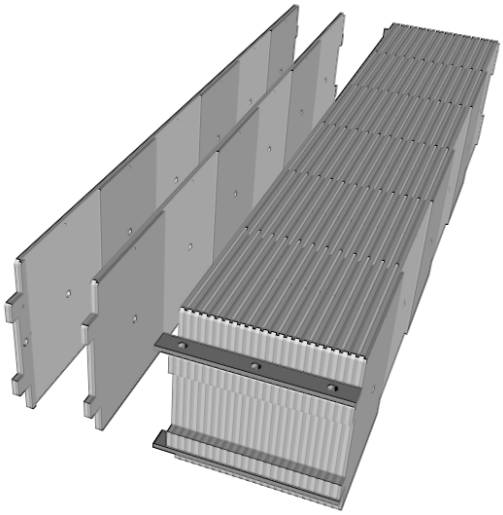

Figure 5.15: *View of the HCAL structure. Two master plates are shown detached with glued spacers. The space between spacers is used for scintillating tile insertion during the optics assembly.*

- stacking up 52 masters with spacers in the assembly tool
- bonding the plates into a laminate by hardening the glue over night in the stressed assembly tool (see bottom of Fig. 5.16)
- next morning two pairs of connecting straps are welded on each corner of the submodule
- rust-proof coating could be applied in a dipping bath (under study)
- checking of the gaps (that will host the scintillators), and storage of submodule for further assembly

A lot of experience in submodule assembly was gained during construction of a total of six HCAL prototypes [33]. Except for the rust-proof coating, the assembly of the prototypes was done according to the steps listed above. From this experience we believe that four submodules can be assembled in one week using one assembly tool.

5.3.3 Construction of modules

One module is assembled from eight submodules that are joint together at the front and at the rear side by two sets of steel bars that are welded to the submodules. At the rear one 4200 mm long back holder is fixed with studs and nuts. The back holder is made of an I-shaped steel beam with several welded reinforced ribs. One module has a dimension of x=4201.5 mm wide, y=262 mm high and z=1655 mm deep (see Fig.5.17), and weights about 9.5 tons. The modules are designed to be the the largest construction element

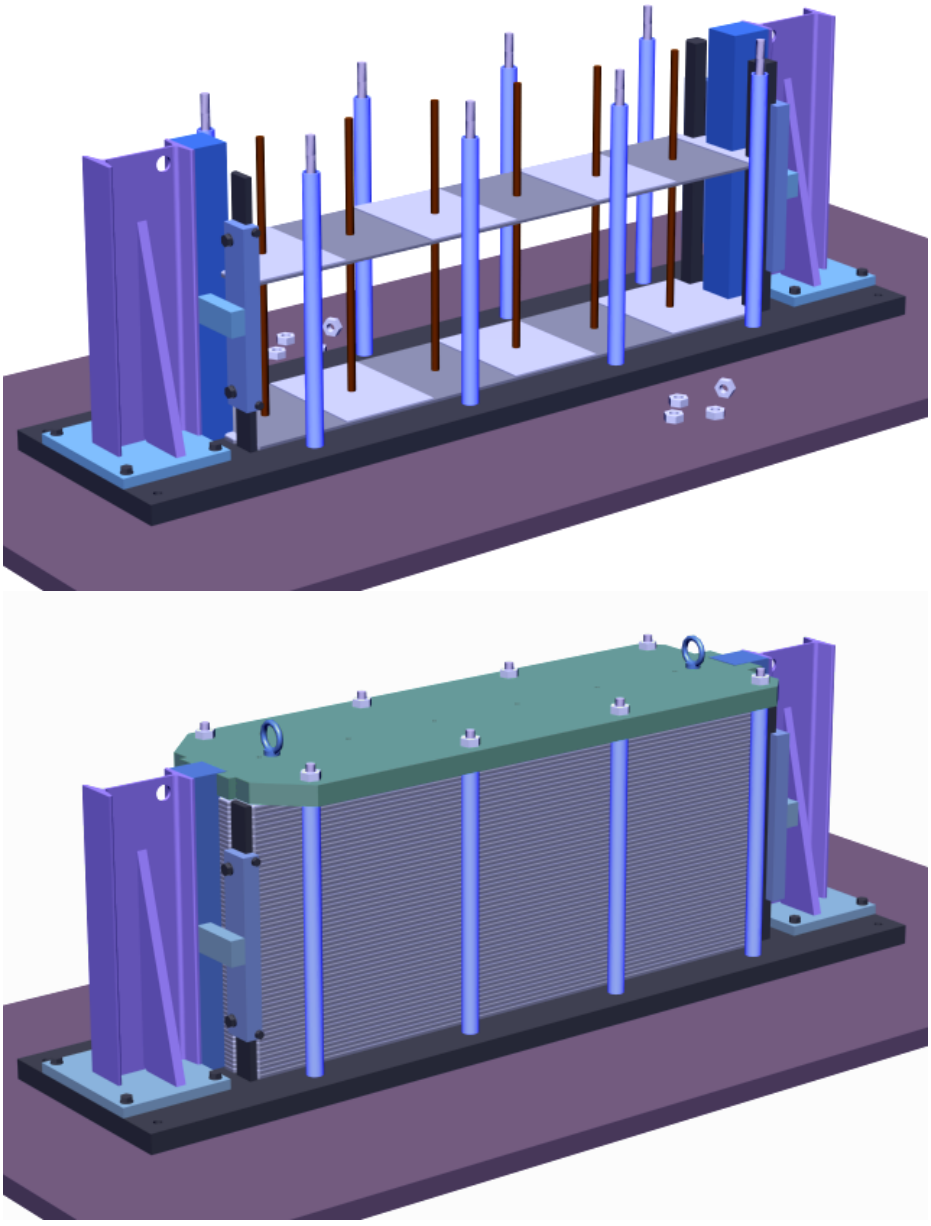

Figure 5.16: *The submodule assembly tool: in the upper figure is shown the master plate insertion, in the bottom figure all plates are stressed for hardening the epoxy glue.*

that is being assembled with optics and tested separately before installation of the overall HCAL detector.

In order to minimize the tolerance requirements for a module (which is a brick in the final HCAL wall), an adjustable inter connection between modules is foreseen. The contact surface between two modules is well defined. At the front face it is the welded 20 mm thick bar and at the rear side it is a flat steel strap welded to the back holder. Small pieces of steel are adjusted such that a horizontal clearance of 0.6 mm between the sampling structure of two modules is reached. This insures that the weight of the

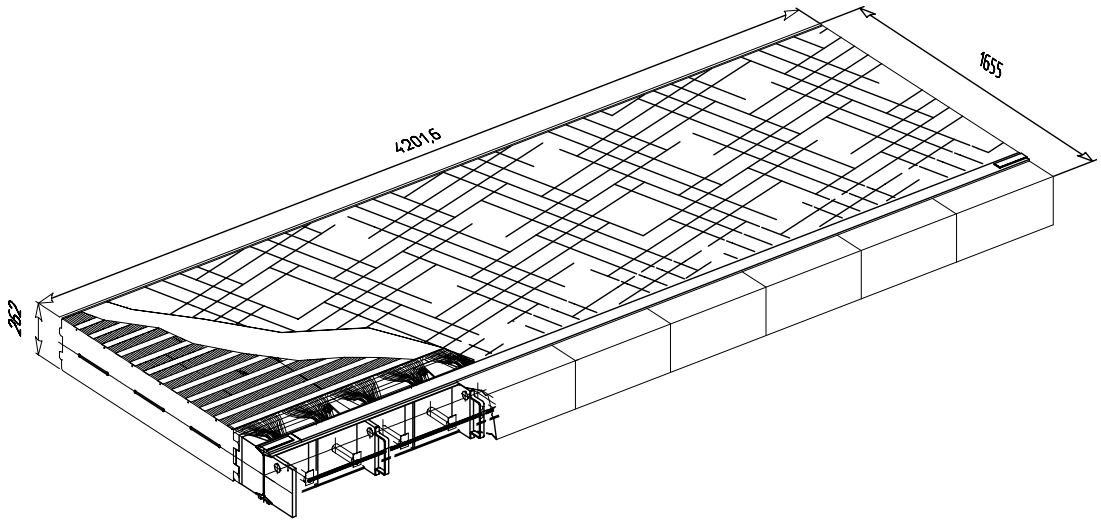

Figure 5.17: *The module structure: eight submodules are assembled to one module, and an I-shape holder is mounted at the back. The whole module is covered with light protecting black paper shown as hatched surface.*

structure is distributed to the front and the back of a module, minimizing the tolerance requirements for the laminate structure of a module.

A detailed strength analysis has been performed [33] calculating the internal stresses for a module at the bottom of the HCAL wall. A maximal deformation in the vertical direction (along y) of 55 microns has been determined (see Fig.5.18). In order to keep the stresses for a module to a minimum when it is maneuvered, a special toll for rotating the module from the vertical to the horizontal position (and vice versa) has been designed [7].

5.3.4 The optical instrumentation

The optics of the tile calorimeter consists of two components, the scintillating tiles and the wavelength shifting (WLS) fibers. Ionizing particles crossing the tiles induce the production of light in the base material with wavelengths in the UV range that are subsequently converted to visible light by scintillating dopants. The scintillating light propagates through the tile to its edges where it is collected by WLS fibers. The fluor in the fiber absorbs the blue light from the scintillator and re-emits it at a longer wavelength.

The scintillating tiles are produced from polystyrene PSM-115 as a base with 1.5% of paraterphenyl (PTP) and 0.03% of POPOP as primary and secondary dopants. For reasons of cost and production rate the injection molding technology is the preferred production technology. The tile dimensions to be produced are shown in Figure 5.19. Two tiles of different dimension are needed to allow a segmentation of HCAL with two different cell sizes. In order to optimize the production, a single type of tile of 256 mm $\times$ 197 mm is being produced, and the smaller tiles of dimension 127 mm $\times$ 197 mm are obtained by cutting big tiles into two pieces. After production the tiles are immediately wrapped into TYVEK of 120-150 micron thickness. This reflective envelope avoids light cross talk between the touching edges of the small tiles, protects the optical reflective surface of

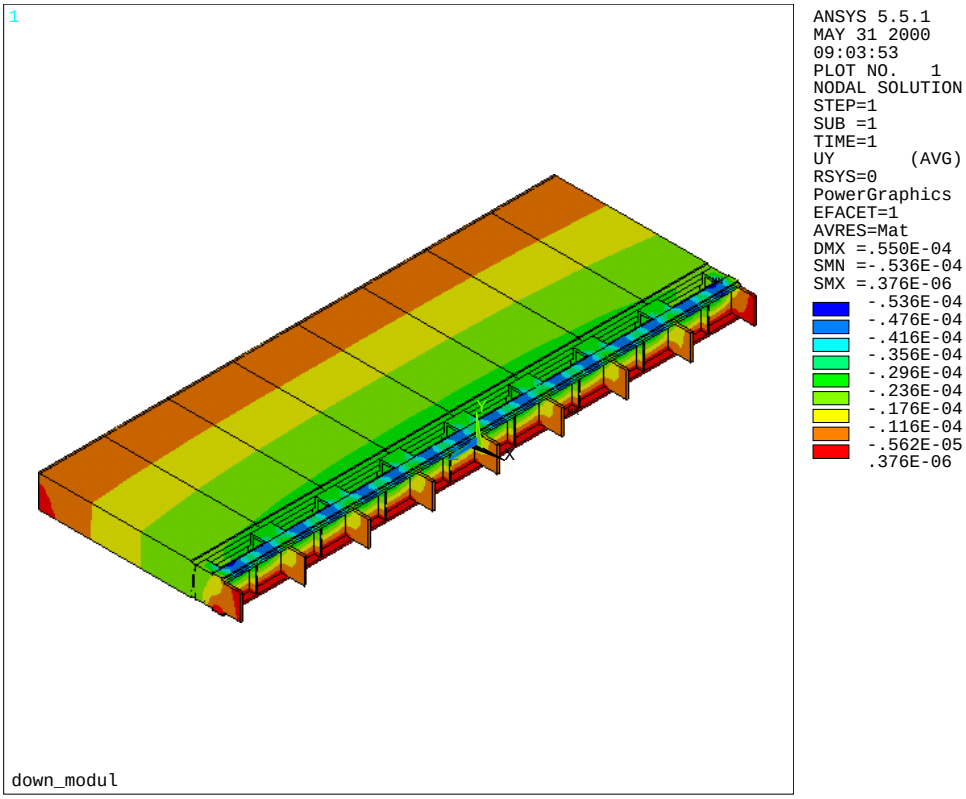

Figure 5.18: *Strength analysis of the distortion in y for the bottom module. The maximum distortion is less than 55 micron.*

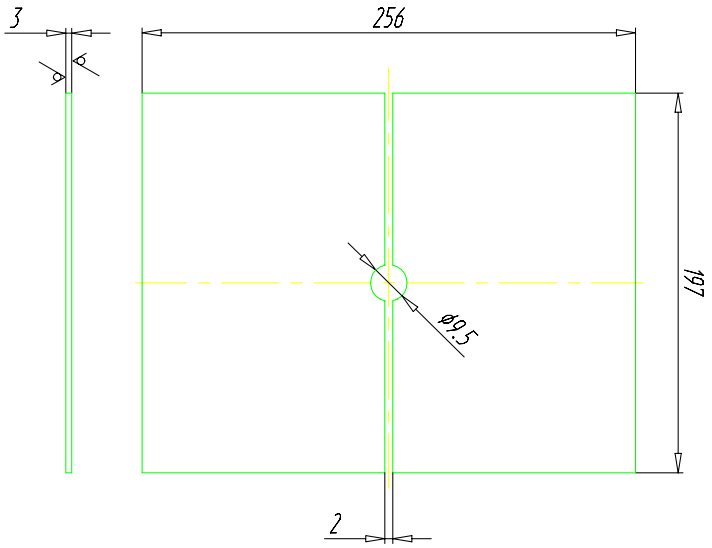

Figure 5.19: *Scintillating tile dimension: two tile types are produced, a big tile of* 256 × 197 mm^2 *and two half-tiles (as shown in figure) for small cells.*

the tiles from contact with materials having an index of refraction that would spoil the internal reflection of the light, and in addition enhances the light yield by redirecting some of the light that is not captured by internal reflections back into the tile. The edges of a tile are wrapped in such a way, that the fiber running along the edge can be easily inserted in between the envelope and the tile edge during the module optics assembly. Quality control of the tile production is foreseen by sampling 10% of all tiles and by measuring the light yield in response to a β-source irradiation at various points of a tile.

Each fiber collects light from three scintillator tiles. The light propagates along the fiber by total reflection. The light collection should be efficient, fast, with low attenuation length and the fibers should be radiation hard. Sample fibers from different producers have been investigated in a comparative way as described in [21, 35]. WLS fibers of 1.2 mm diameter doped with fast shifter have been chosen as baseline solution. Such fibers are commercially available and are produced by Bicron, Kuraray and Pol.Hi.Tech. The choice of fiber will be made in 2001. Since the requirements in radiation hardness are very different for cells close to the beam and far away from the beam, different types of fiber could be foreseen for the inner and outer sections of HCAL. A total of 50k fibers with an identical length of 1.6 m each have to be produced. In order to increase the light collection efficiency the fiber end opposite to the photomultiplier is coated with a layer of reflective aluminium. The coating procedure is being developed and a typical reflectivity of 85% has been obtained on a test sample of 170 fibers.

The optics assembly has been elaborated during the HCAL prototype construction. To equip the laminate structure with optics, the best entity is one module that is rotated in a vertical position for this purpose (with the back holder in a horizontal position). For rotating the module a special tool has been designed [7]. The manual assembly starts by inserting the TYVEK-wrapped tiles into the slits between the master plates. Then the fibers are fed through from top to bottom between the tile edge and the TYVEK envelope. To form a readout cell the fibers are grouped in bundles at the rear side of the module. For calibration purposes [33], two clear fibers are joint to the bundle for each cell that will transport the light from a LED. The bundle of fibers is inserted in a bundle ring and glued together with epoxy glue. After cutting the fiber bundle ends to length, the ends are polished. For mass production a small milling machine will ensure an efficient cutting and polishing of the fiber bundles. For illustration one of the first HCAL prototype modules is shown in Figure 5.20 after optics assembly.

Each cell is readout by one photomultiplier tube that is attached to the back holder of the module. The optical connection between the fiber bundle and the photomultiplier is ensured by a 35 mm long light mixer of squared shape. To protect the photomultiplier tube from the magnetic stray field the tube including the light mixer is housed inside a 3 mm thick steel tube and μ-metal foil to shield against the magnetic stray field. A stray field of approximately 20 Gauss along z but negligible in x and y is expected in the present design [48]. A large variety of photomultiplier tubes (PMT) from various manufacturers is under test [47] and several tubes have been identified as possible candidates that fulfill the requirements for the HCAL readout. The requirements are identical to those of the ECAL (see Table 5.4) apart from the gain, that should be approximately 10 times higher.

Figure 5.20: *One of the first HCAL prototype modules after optics assembly.*

5.3.5 The calibration system and quality control

Once the optics is assembled each module undergoes some quality control. For this purpose the module is connected to the movable-source calibration system, that will also monitor the HCAL performance over the years of operation.

Via stainless-steel pipes that are running through holes in the calorimeter module and that are interconnected with C-shaped tubes, a miniature Cs^{137} radioactive source is passed through every scintillator tile of a module. The source is encapsulated in a 2 mm diameter, 4 mm long stainless steel tube that is welded at both ends. The source is driven by a hydraulic system that is filled with distilled water. The system includes a garage to store the source, and a computer controlled pump and valves that allow to reverse the water flow direction.

The source activity of 5 mCi induces a current of up to 90 nA in the PMT, that is integrated by a slow control electronics circuit. The integration time does not exceed 2 ms and the readout of all PMT channels is repeated each 5 ms. The average source velocity is about $20 \div 40$ cm/s. Recording the signal from each individual tile allows to check the

quality of the optical response and uniformity and to equalize the response of all readout cells by adjusting the HV of the corresponding photomultiplier. The system has been tested and operates successfully on the HCAL prototype [34].

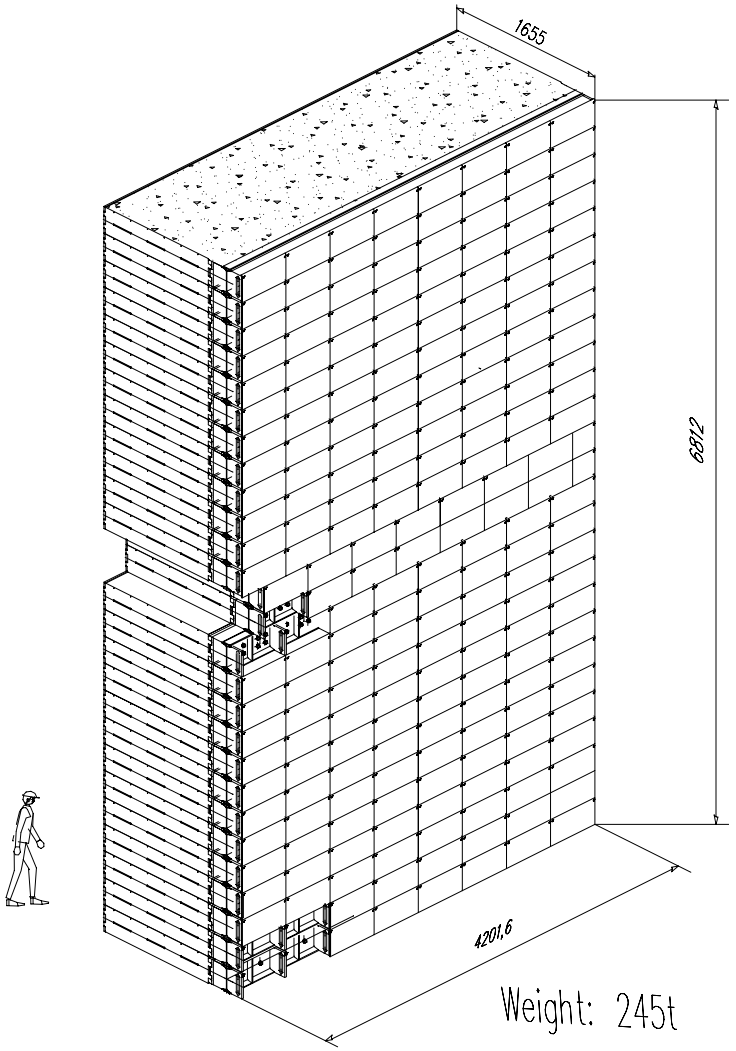

Figure 5.21: *View of one half of the hadron calorimeter: there are 26 horizontal modules stacked on top of each other. Two central modules are shorter to allow the accelerator beam-pipe to traverse.*

5.3.6 Installation of HCAL

The self supporting HCAL structure is split into two parts that can move away from each other into a garage position in order to allow access to e.g. the photomultipliers. Each half is built up by stacking 26 modules, that are fully equipped with optics, on top of each other on a support platform that is placed on rails (see Fig.5.1)and that supports a weight of ≈245 tons per half HCAL. In order to minimize any dead space in between

the two half HCAL structures care is taken in the design to perfectly align the surfaces that will be in contact. Furthermore, the innermost master plate of each module has half width and the periodic sampling structure of scintillator tiles and spacers is being continued without discontinuity to the opposite half. To allow the beam pipe traversing the HCAL wall, a mechanical hole of 525.2 mm $\times$ 525.2 mm is left in the center by using modules in the middle of the HCAL that have a reduced length (see Fig.5.21). The space between the HCAL structure and the beam pipe is filled with shielding material.

Even though the mechanical structure is identical for the whole HCAL detector, the optics are segmented into two sections that have different cell size. The inner section closest to the beam pipe contains 860 cells of 131.3 mm and covers a surface of 4.2 m $\times$ 3.7 m. The outer section has 608 cells of 262.6 mm and extends to 8.4 m $\times$ 6.8 m.

5.4 Electronics of ECAL/HCAL

5.4.1 Overview

Because of the similarity of input signals and functionalities, it has been decided to use a common electronic system for the ECAL and HCAL. This system is based on a deadtimeless and low pedestal integrator system using delay lines, which was already described in the technical proposal [1] and is described in detail in [12, 51], followed by ADC's and pipeline buffers. The front-end crate and its main interconnections are shown in Fig. 5.22. Each card is connected to 32 channels of the ECAL or the HCAL. The image of the calorimeters to cards mapping is shown on Figure 5.23.

After digitisation in the front-end card the data is processed further and sent to a trigger validation card which will be described in the Trigger TDR. The data is also pipelined and stored on the front-end card, and then sent through the back plane to a calorimeter readout card (CROC), which is described in section 5.4.5 and in [52].

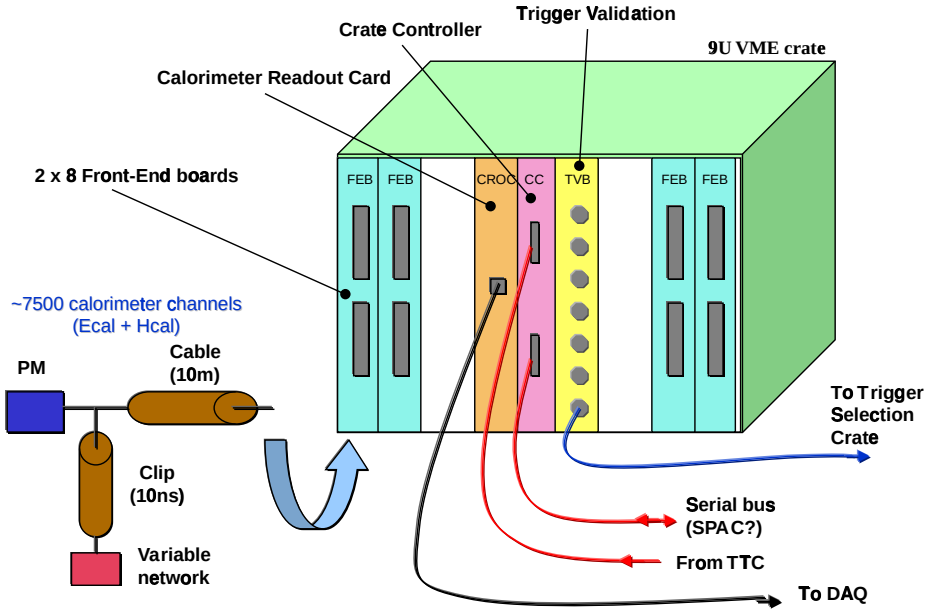

Figure 5.22: *Overview of the Front-End Crate.*

5.4.2 Pulse shaping and front-end chip

Taking advantage of the fact that the scintillator and WLS based calorimeter system is inherently fast, it has been decided to build an electronic system capable of measurements every bunch crossing while being insensitive to pileup from signals associated to a preceding bunch crossing. The PM pulses therefore have to be shaped to eliminate the small tail of the pulses extending after 25 ns. A schematics of the PM signal shaping and of the front-end chip is shown on Fig. 5.24.

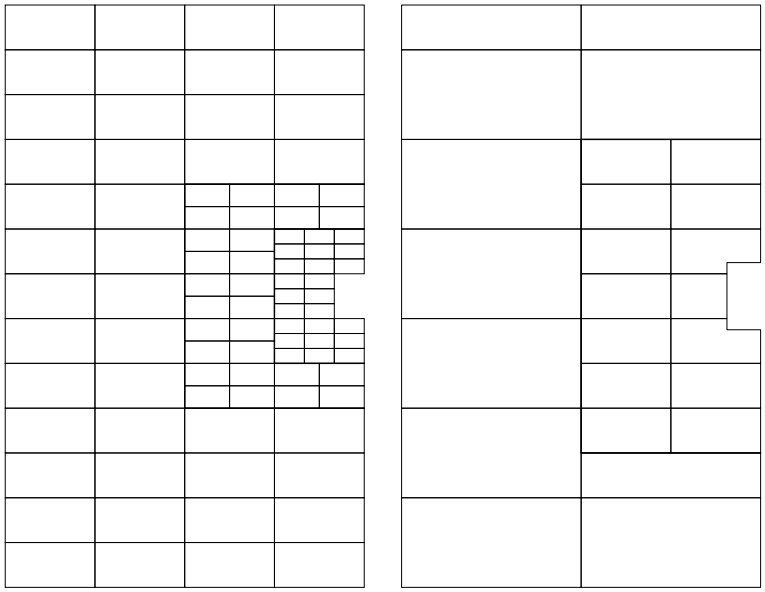

Figure 5.23: *Mapping of the ECAL cells (left) and HCAL cells (right) to their 32 channels cards.*

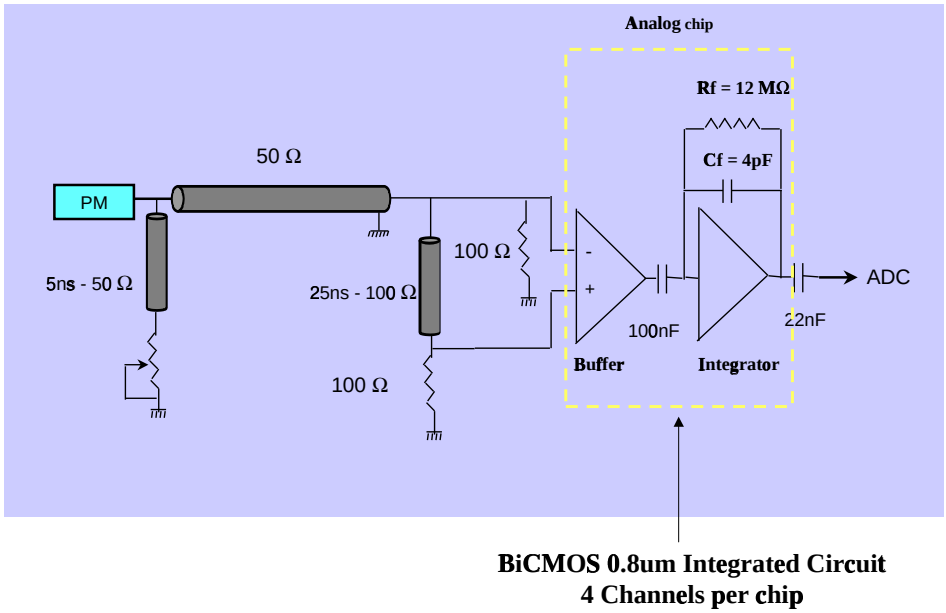

Figure 5.24: *Schematics of the PM signal shaping and of the front-end chip.*

The PM pulse is shortened by a clipping line. The length of the line is typically one meter, giving a FWHM of about 10 ns. The resistor load at the end of the line is adjusted to obtain a return to a 0 Volt level after clipping. Its exact value depends on the fall time of the PM pulse and hence of the WLS fiber used. Typical values are around 25 Ω. A 82 pF capacitor can be used in parallel with the load to speed up the shaped pulse fall time. Of course the cancellation of the later part of the pulse by the pulse reflected at the end of the clipping line is only exact on average. Due to fluctuations in number of photoelectrons as function of time, a fluctuation is introduced in the shaping. However

the effect is small especially for ECAL where there are 1000 photoelectrons per GeV.

The pulses are then sent by ten meters of coaxial cables to the front-end cards which are placed in crates above the calorimeters (see Fig. 5.13). The pulse-shape distortion produced by the cable will be compensated to first order by a pole-zero circuit placed after the integrator (not shown on Fig. 5.24).

The first element of the card is the front-end chip which contains a buffer amplifier and an integrator. To discharge the integrator the same pulse is subtracted in a buffer amplifier after a 25 ns delay, obtained by a lumped-element delay line. Simulated input and output pulses are shown in Fig. 5.25 and the schematics of the analog chip is given in Fig. 5.26.

The circuit has been realized in AMS 0.8 μ BICMOS technology. The last iteration is satisfactory, however further test should be done including tests of chips encapsulated in a plastic package. In this last version a noise of 150 μV has been obtained after a 25 ns integration, which should correspond to a total noise of less than one ADC count. As described in the section 3.4 on prototype results, the tail of the pulse integral in the next sampling is about 2% with an additional fluctuation of 1%. The impact of the amplifier noise on the physics performance has also been discussed in section 3.4. It is found to be negligible as compared to the resolution of the ECAL. It is foreseen to order the final chips in mid 2001.

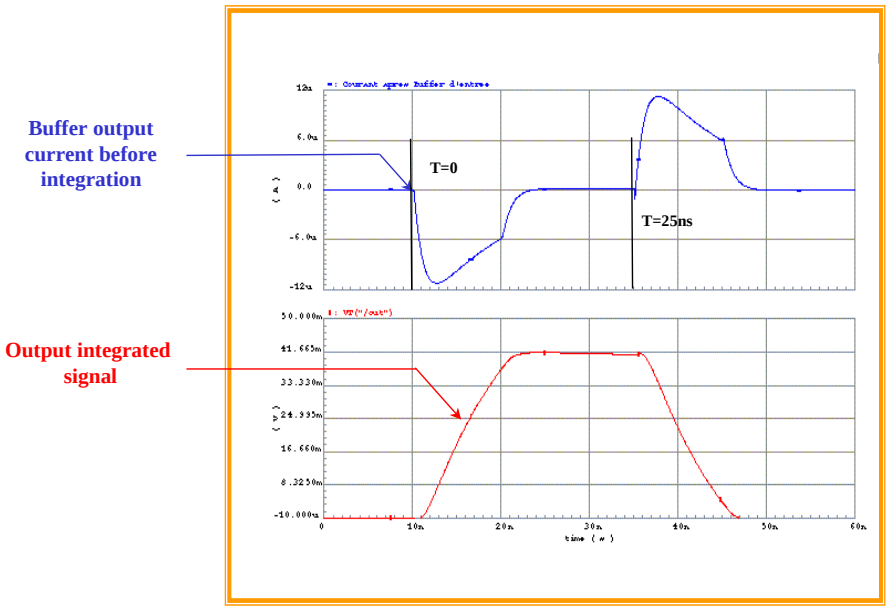

Figure 5.25: *Simulated input and output pulses of the integrator.*

5.4.3 The front-end board

Figure 5.27 shows the block diagram of the 32 channel front-end board. It is a 9U board using the VME mechanics but a specialized serial bus used for ECS purpose.

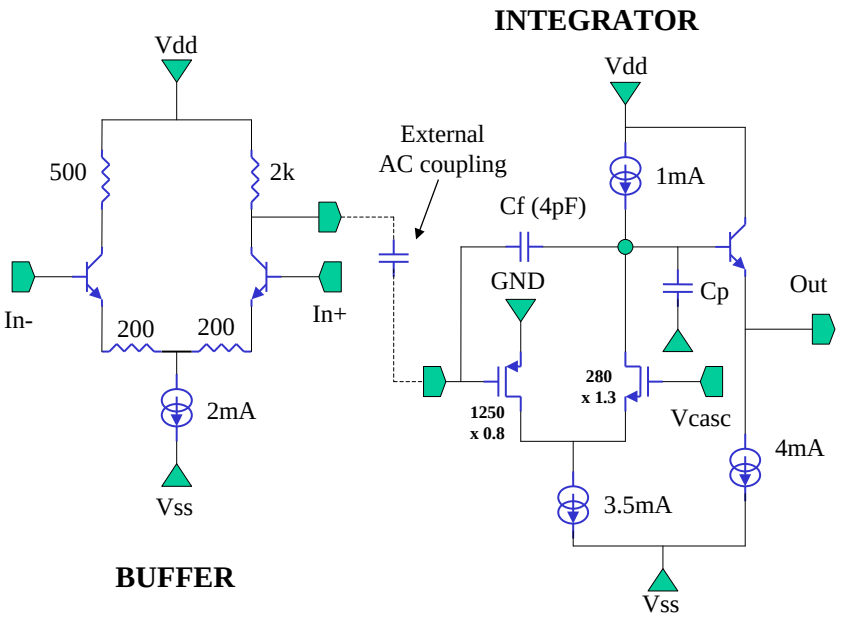

Figure 5.26: *Schematics of the analog chip.*

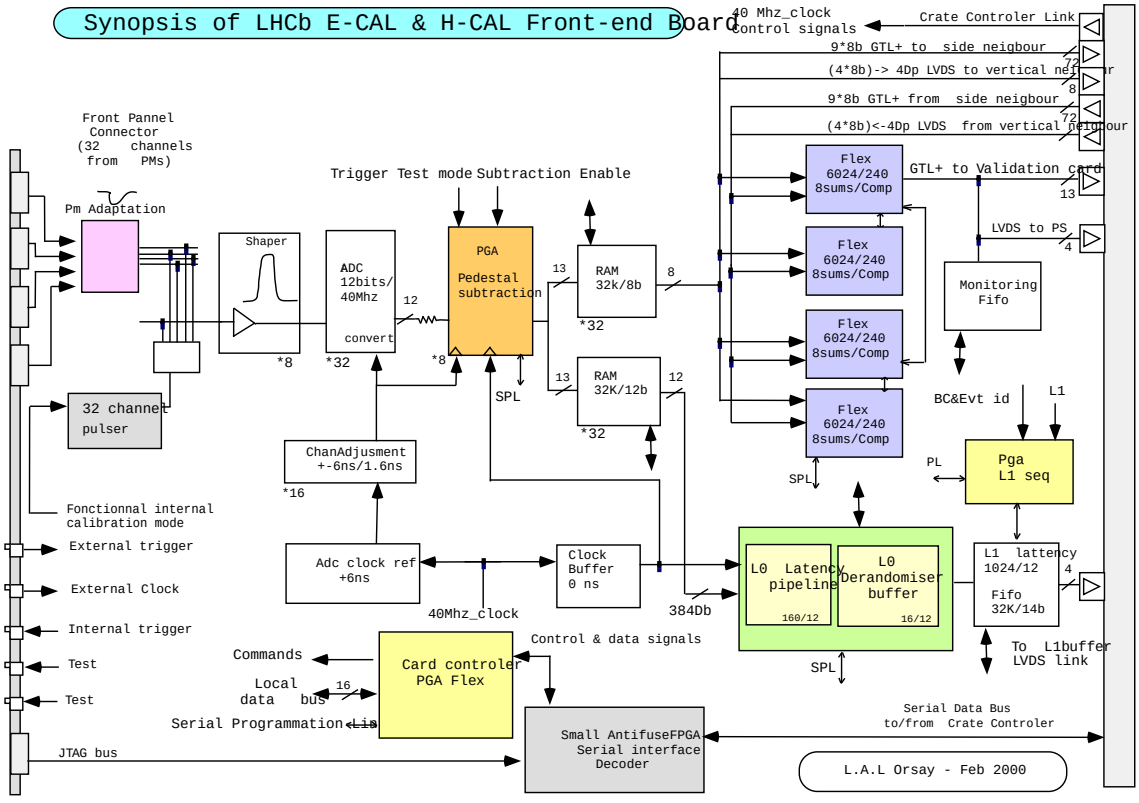

Figure 5.27: *Block diagram of the Front-End board.*

The pulses from the front-end chip, described above, are then sent to 12 bits ADCs. The pulses after integration are flat (within 1%) over ± 2 ns around the maximum. To strobe at the maximum of the pulse, the different delays in the photomultipliers have to be compensated. This is achieved by adjusting the clock of each ADC by a delay chip to an accuracy of 1 ns. The digitized output of the ADCs are then re-synchronized to a common clock (per card) in a register at the entrance of the next chip.

The pulses at the integrator output can be subject to baseline shift and to the influence of low frequency pickup noise which would cause slow variation of the ADC pedestal. These variations are cancelled through a "digital differentiation" by subtracting the digitization in a preceding sample (25 ns before). This subtraction also defines the effective integration time of the amplifier and therefore limits the integrated thermal noise from the buffer amplifier. To decrease the possibility of subtracting a signal present in the same channel, the quantity subtracted is actually the smallest of the two preceding measurements. Even at the highest occupancy, about 5%, the probability of subtracting a significant signal is therefore reduced to less than 0.25%. Simulations have shown that this procedure introduces negligible deterioration of energy and position measurements [15]. However the procedure introduces a small pedestal shift of about 40% of the 40 MHz noise (i.e less then one ADC count) and an increase of the 40 MHz noise by 16%.

The subtraction of the smallest of the two preceding samples is performed in a dedicated FPGA (in the present version 4 channels per FPGA). The data, which is then on 13 bits to allow for a negative result of the subtraction, is then coded by a 32k 12 bits RAM in a pseudo floating format correcting for nonlinearity and subtracting a mean remaining pedestal to an accuracy of about 1/8 th of a count [52]. Actually only an 8k 12 bits memory would be needed, however the smallest commercially available element is now the 32k, and the remaining part of the memory is used to store bit patterns which will be used to test the card functionality.

A similar 32k 8 bits RAM is used to obtain the E_T values for the trigger processing. As will be described in the trigger TDR this information is processed further by forming blocks of 2×2 cells and choosing the cell on the card with the highest E_T content. The trigger is processed in a fully synchronous and pipelined system at 40 MHz.

The 32×12 bits data are stored in a 4 μs fixed latency buffer (160 cells). After a Level 0 decision the data is passed to a 16 deep derandomizer buffer. These two functionalities are obtained by commercial FPGAs. In the present baseline design and current prototype, 8 channels are stored in a EPF10K50E, however other units may be chosen for the final design in mid-2002.

A 34-word buffer is then produced, by creating a header including the bunch crossing ID information, followed by the 32 data words, and a trailer including error detection flags. We use now two extra bits to tag the header and trailer in the block, to allow a safer detection of the event boundary. This block is stored in a 1024 block (events) FIFO ($1k\times34\times14$ bits), waiting for the Level 1 Yes or No decision, which always fires its readout. Only data corresponding to Level 1 Yes is sent over the back plane towards the CROC board [52].

5.4.4 Commercial components

It has been checked that there exists at least one commercial 12 bits ADC satisfying our need. It is the AD9042 used by CMS for its crystal calorimeter. Digital noise fed back to the ADC input is coherent among all channels, and intrinsic thermal noise at the ADC input are found to be 0.2 and 0.5 counts respectively, i.e smaller than the front-end chip noise.

The strobe of the ADC should be adjusted to better than one ns at the maximum of the integrated pulse. This is performed by a commercial delay chip offering a range of $\pm$ 4 ns or $\pm$6.4 ns in steps of 1 or 1.6 ns, respectively. In the final card design, a special LHC-chip of CERN design may be used. As mentioned above the other chips are commercial FPGA's and memories, and are not operated in a critical fashion since the clock speed is only 40 MHz.

5.4.5 The calorimeter readout card and the crate controller

While the front-end chip is essentially finalized and the front-end card baseline solution very well defined, the calorimeter readout card (CROC) and the crate controller card are still under design. Many elements of these cards will be common with the ones required for other LHCb detectors. We therefore expect that the design of these cards will continue to evolve over the next 1-2 years.

A specific functionality of the CROC is the zero suppression. This point has been studied in a first conceptual design of the CROC [52]. A simple option is to apply a threshold and to transmit to the DAQ only those channels above threshold. A label must then identify each channel and the data format is a sequence of label-data-label-data. However for accurate position and energy measurement in ECAL it is better to measure the tail of the showers down to very low values. The idea of the 2 dimensional zero-suppression is to force readout of all the 8 neighboring cells of the cells above a threshold called seeds. It is then possible to raise the threshold of the seeds thus obtaining a similar final amount of data from 2D zero-suppression as from the simple scheme. The proposed method is to build a bitmap of the channel to be readout first by applying a threshold to find the seeds, then by adding the neighbors into the bitmap and to read this map to build the output buffer. It has been checked that the average time available between level 1 trigger (25 μs) is more than needed.

If the threshold for readout of the ECAL/HCAL is set, in the simple option, at 4 ADC counts i.e. at about three times the noise level then, on simulated B events, in average 400 out of 6000 ECAL cells and 200 out of 1500 HCAL cells have to be readout. This corresponds to about 2.5 kbytes of data.

Studies are ongoing to adapt the same crate controller and CROC to the PS/SPD detector. The amount of data per event would be about 2 kbytes.

5.4.6 Radiation levels

At the foreseen position of the crates, present calculations predict a level of radiation of around 100 rad per year [32]. Radiation damage of electronics should therefore not be a

problem. The only problem of concern is the one of single-event upset caused by nuclear interactions in the chips, which change the value of a bit in memories. If this change affects only one channel in one event the problem is not severe. However if a program of a FPGA is affected then all subsequent events would be affected until a reload, and if a program in the CROC were affected it could contaminate a full crate. This question will be addressed in the coming year. It may guide our choice of FPGA or force to move the intelligent part of the CROC and crate controller behind a shielding wall leaving only repeaters in the crate.

5.5 Electronics of preshower and scintillator pad detector

5.5.1 Specific PS and SPD pulse shapes

The signal shape of the PS and SPD have about the same duration as the ECAL and HCAL pulses; on average 85% of the charge is obtained in 25 ns. However, since the average number of photo electrons is only about 25 per MIP, there are very large fluctuations in the signal pulse shape [38]. It was therefore considered unreasonable to try to implement a delay-line pulse shaping as in the ECAL/HCAL. On the other hand, since the useful dynamic range is typically only from 1 MIP to 100 MIP, an ADC with only 10 bits can be used and pedestal stability is not as important as for the ECAL/HCAL electronics, while it is important to integrate the signal over a time as long as possible within the 25 ns limitations. The phototube chosen to detect the light from the PS and SPD fibers is a 64 channel multi-anode PM. The HV is common to all 64 channels and there is a non-adjustable gain dispersion among these channels of about a factor of 4, which however is constant in time. It has therefore been decided to place the "very front-end" amplifier integrator card on the back of the phototubes and to compensate the gain variation by load resistances at the entrance of the amplifier which will be adjusted between 50 Ω and 200 Ω.

5.5.2 The PS "very front-end" design

The solution adopted is to alternate every 25 ns between two integrators and to reset one integrator when the other one is active. The signal is sampled by track-and-hold circuits and the output of the active integrator is chosen by a multiplexer, followed by a twisted-pair cable driver. All circuits elements are functioning in differential mode to improve stability and pickup-noise rejection. The circuit design is shown in Fig. 5.28 and Fig. 5.29 and detailed in [39].

Simulation of the behaviour of the circuits is shown in the case of a 20 GeV incident electron delivering a signal of about 20 MIPs. The signals at the input, after integration, track-and-hold and multiplexer are shown in Fig. 5.30, 5.31, 5.32 and 5.33.

The phasing of the clock with respect to the signal determines the start of the integration. Since the 64 fiber lengths for a given PM are identical and the delay inside the PM is identical within a fraction of one ns, it is sufficient to have one clock adjustment

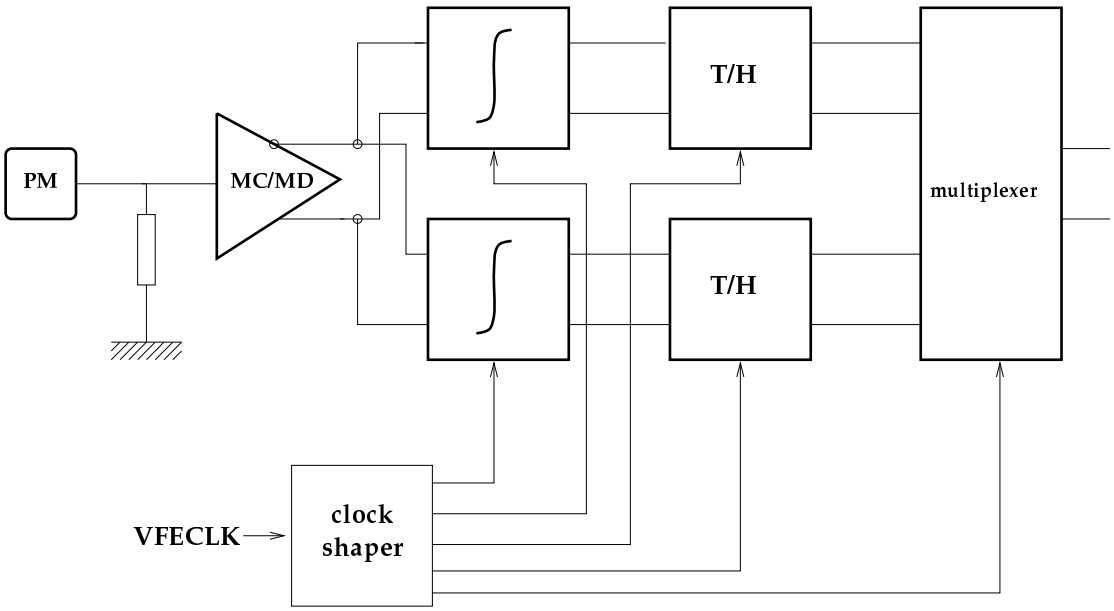

Figure 5.28: *"Very front-end" design.*

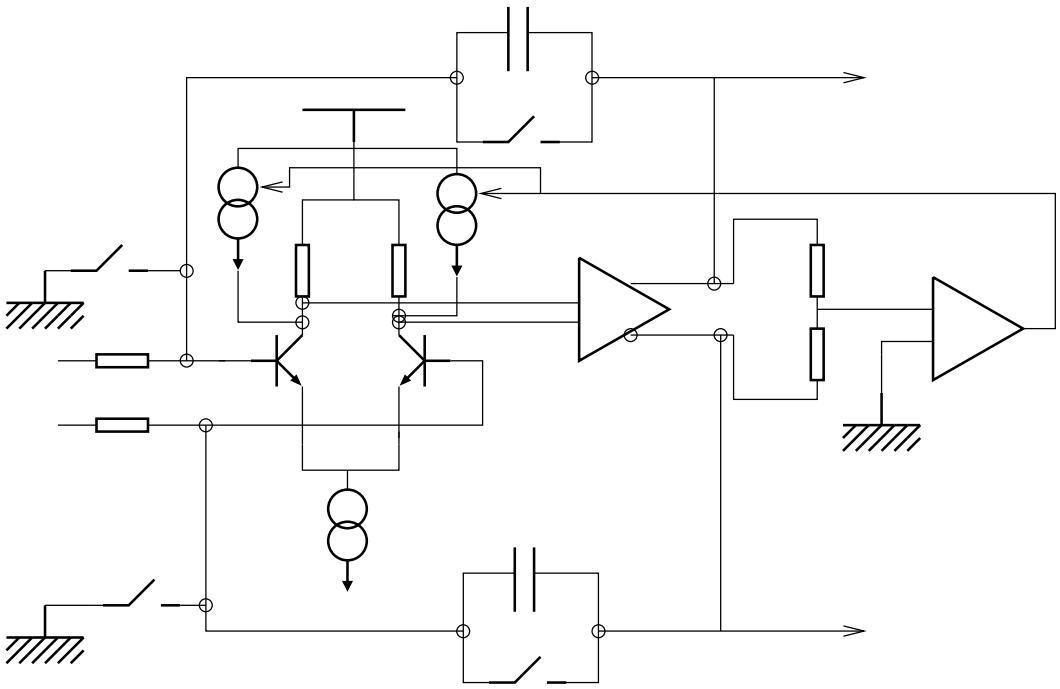

Figure 5.29: *Schematics of the integrator.*

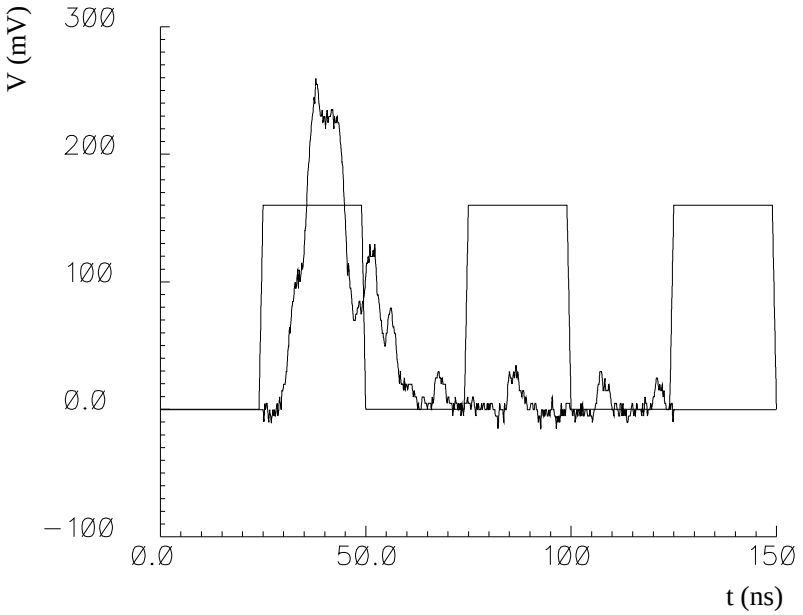

Figure 5.30: *Simulation with a 20 GeV electron signal: clock and input signal.*

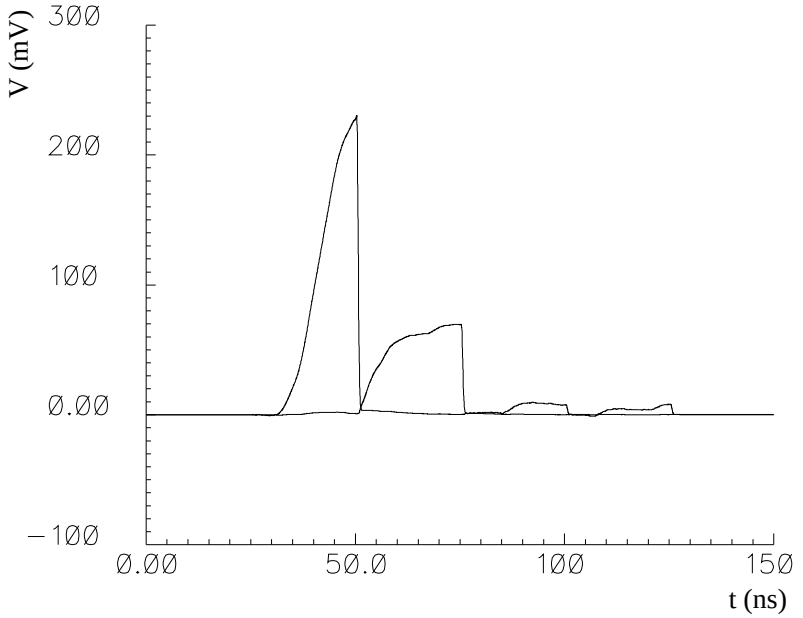

Figure 5.31: *Simulation with a 20 GeV electron signal: integrator outputs of the 2 channels.*

(in steps of one ns) per phototube. The amplifier integrator circuits will be realized in monolithic AMS 0.8 μ BICMOS technology . It is foreseen to implement 8 channels per chip.

As discussed in section 3.4, a prototype has been built (with a single channel) which worked satisfactorily (after a few iterations, as usual). The dynamic range is one Volt with a noise of 1 mV. Eight chips will be grouped in a card on each phototube. The output of the multiplexers are sent through twisted pair cables of 10 to 20 meters length

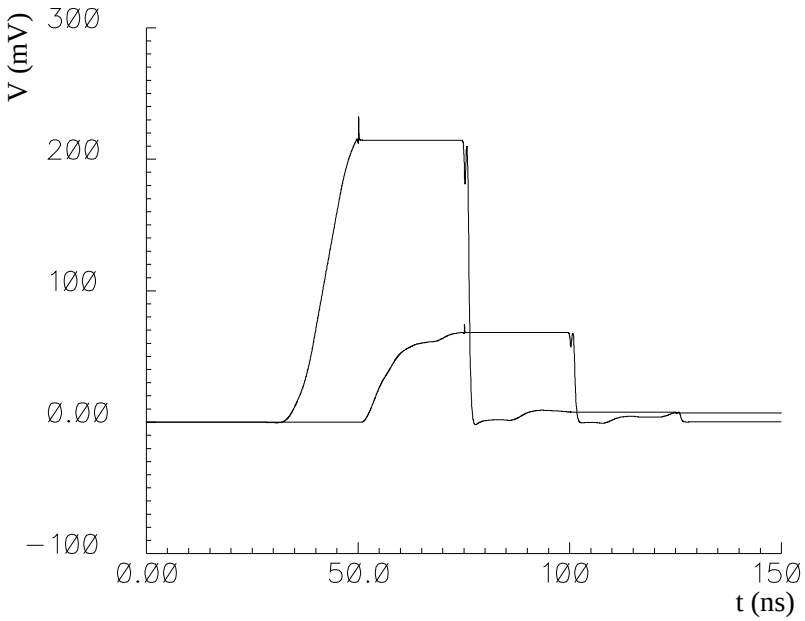

Figure 5.32: *Simulation with a 20 GeV electron signal: track and hold outputs.*

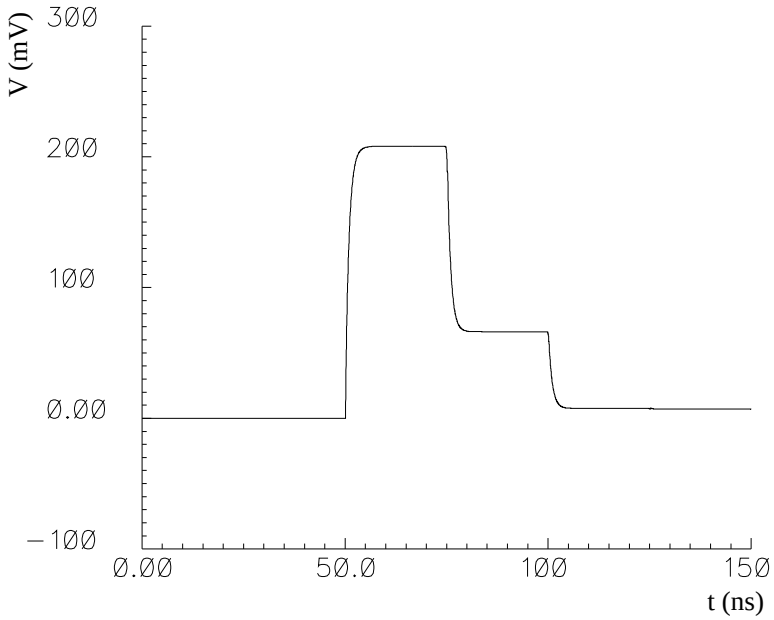

Figure 5.33: *Simulation with a 20 GeV electron signal: output after the multiplexer.*

to the ADC placed in front-end boards.

5.5.3 The SPD "very front-end" design

The SPD function is to discriminate between charged particles and neutrals in a detector which matches the preshower and ECAL cell size. The SPD signals are obtained, as in the case of the PS, from 64 channel multianode photomultipliers. The main difference of specification is that there is no compelling reason to do pulseheight analysis on SPD sig-

nals. It was therefore decided to use a simpler solution with a simple discriminator output and a threshold set at 0.5 MIP thus obtaining 98% efficiency on charged particles [17, 25].

The principle of the design is shown in Fig. 5.34 and detailed in [13]. The front part of the circuit is identical to the one of the preshower. After the track and hold an operational amplifier is used to subtract 15% of a sample from the following one. This cancels on average the charge delivered by a pulse in the time interval between 25 and 50 ns after its start.

The complete circuit has been designed and simulated using SPECTRE as electrical simulator. The results are shown in Fig. 5.35 and show, on an example of four pulses, how one can be sensitive to a wide spectrum of pulses without too much multiple firing of the discriminator and while keeping sensitivity in successive 25 ns periods.

The signal output is sent via twisted pairs to the PS front-end card and the single bit carrying the information on the SPD state is processed together with the 10 bits of the preshower.

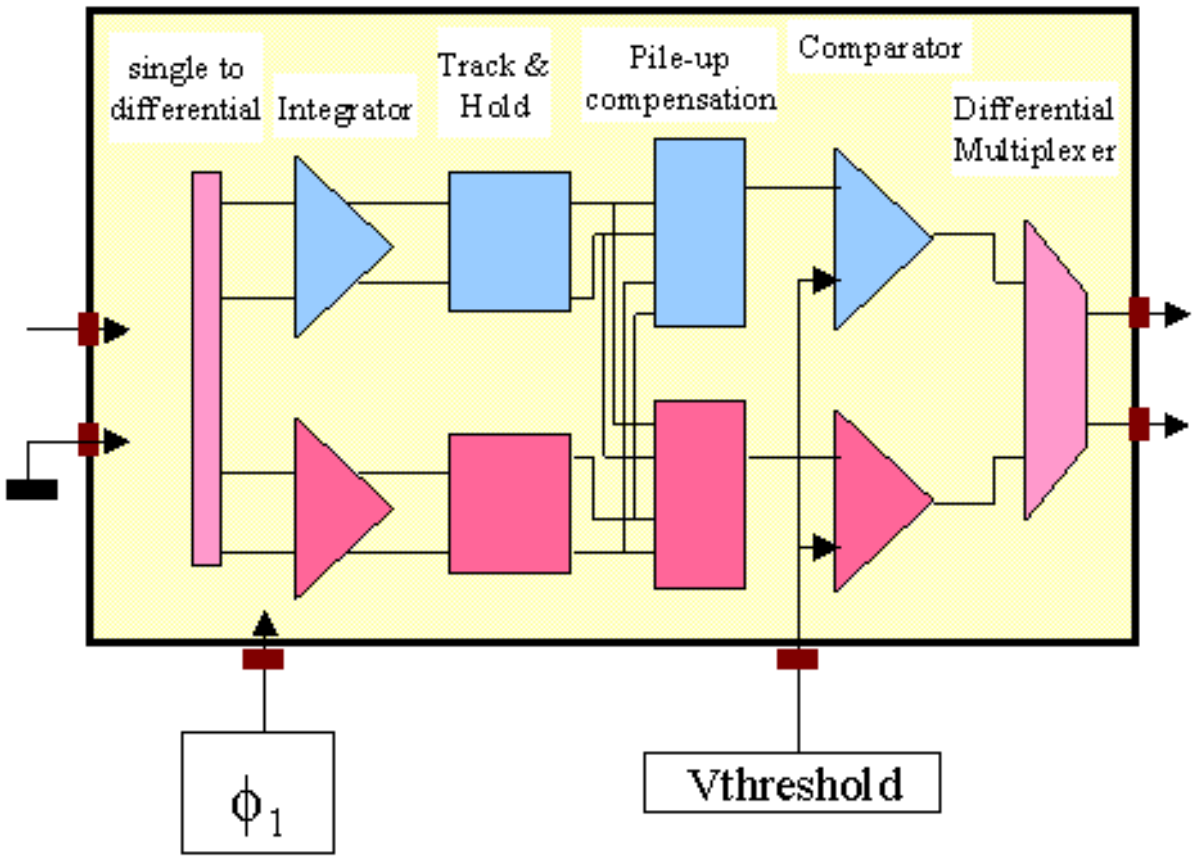

Figure 5.34: *"Very front-end" design for the SPD.*

5.5.4 The PS, SPD front-end board

The front-end boards are in crates that are placed on top of the ECAL, as shown in Fig. 5.13. They receive the analogue signals from 64 PS amplifiers and integrators, and

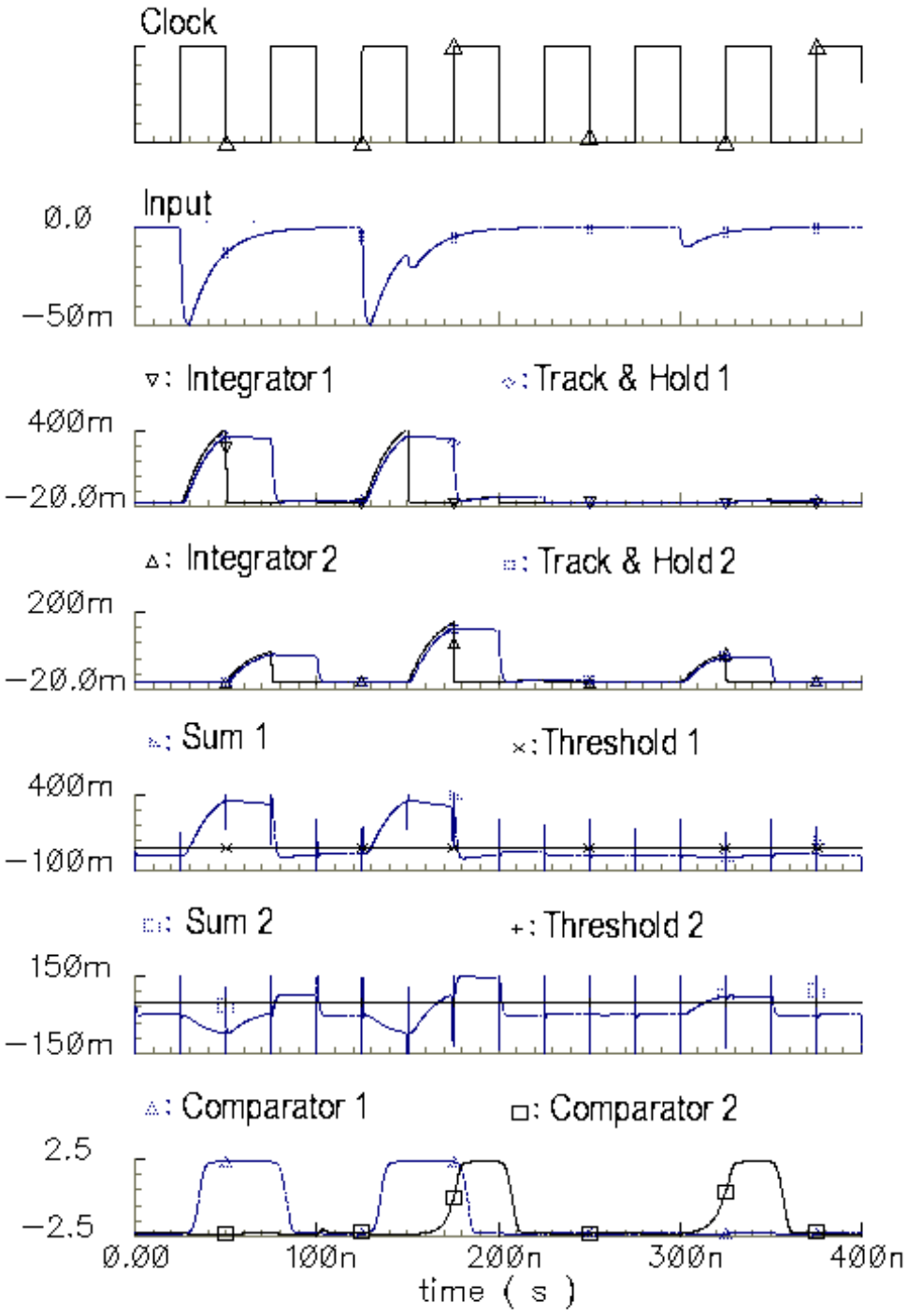

Figure 5.35: *Simulation results of the discriminator blocks. Processing steps for four possible events.*

from the corresponding 64 SPD discriminators. They implement functions similar to the ones of the HCAL/ECAL front-end boards i.e an ADC for the preshower signal, pedestal correction and gain calibration, preparation of trigger information, pipeline storage and selection of data for readout upon reception of trigger signals.

The schematics of the card is shown in Figure 5.36 and the card is described in detail in [14]. The preshower signals are digitized by 10 bits CMOS ADC's, the clock of the ADC are adjusted to be well centered in the sample and hold output from the very front-end cards, a single adjustment is sufficient per card (contrary to the case of the HCAL/ECAL card).

The 10 bits ADC format is then corrected for pedestal and gain variation and coded in an 8 bits pseudo floating format by a Look Up Table (LUT) or RAM. The address range of the RAM has to be at least 11 bits (i.e a 2K RAM) since each of the two integrators used by multiplexing for each signal can have different gains and pedestals. The coding gives 1 bit accuracy from 0 to 63 channels and between 3% and 1.5% accuracy for higher values, which is sufficient in view of the large fluctuations of the preshower.

To take into account the influence of a sample on the following one (since 15% of the charge is integrated in the following sample) a correction is foreseen using the data from two successive samples. This can be performed in a very general way by a 16 bits address LUT (LUT2). The number of registers can be extended to provide extra 25 ns delays compensating the different cable lengths for signals coming from PMs from top or from bottom of the apparatus. The output of the LUT includes 8 bits for the coded pulse height and 1 bit for the trigger, when the signal is typical of an electron or of a photon (for example greater than 5 MIPs).

The PS trigger information, the SPD information and the 8 bits of PS pulse height information are then sent to the Level 0 pipeline the derandomizer buffer and the Level 1 buffer using the same implementation as in the HCAL/ECAL card.

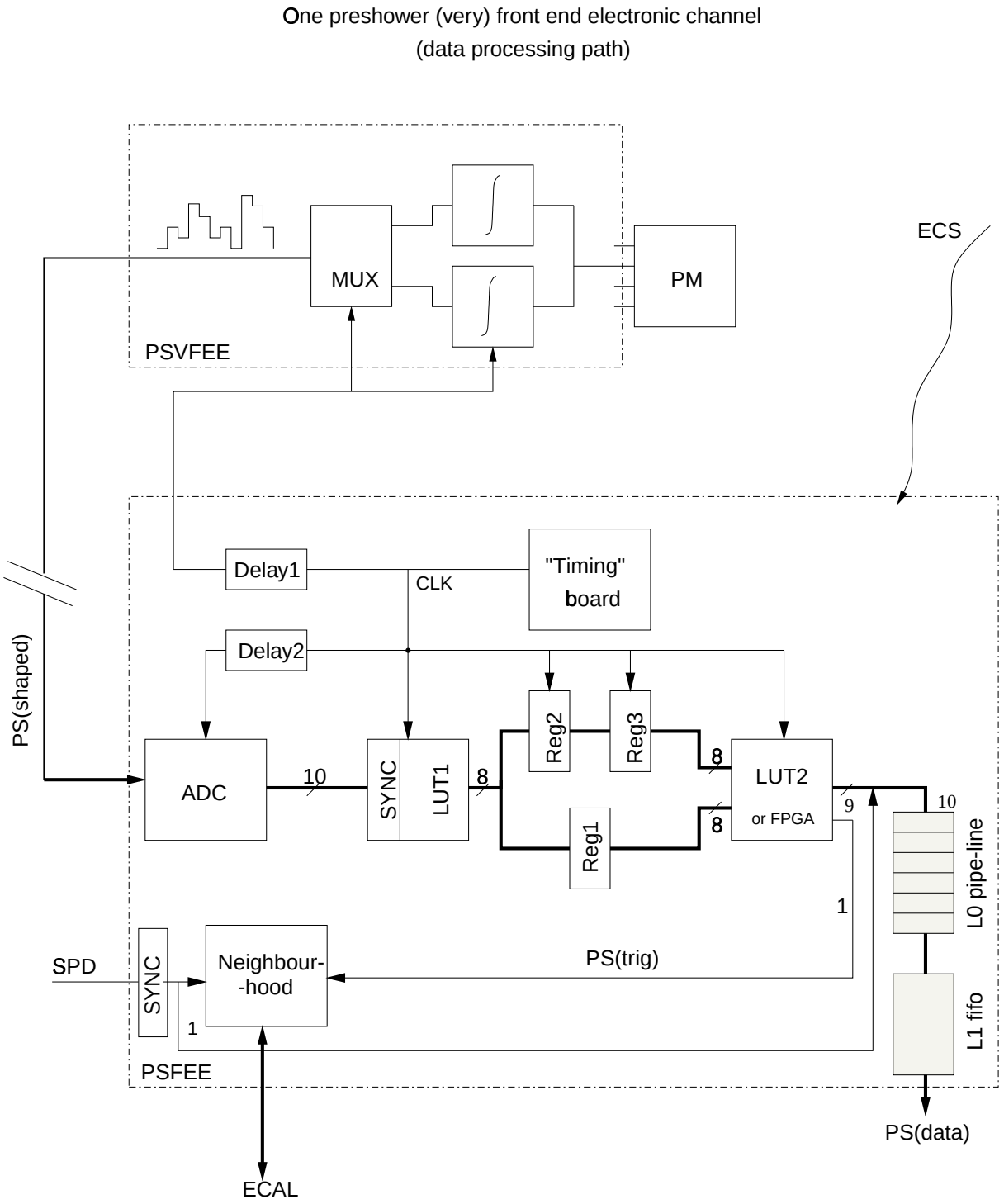

Figure 5.36: *Schematics of the front-end board.*

5.6 Safety aspects

All calorimeter subdetectors will comply with the safety policy at CERN (SAPOCO 42), and will follow the safety rules and codes that are relevant for their construction and operation. In the following we summarize the specific risks to the calorimeter system and some safety measures, as proposed in the Initial Safety Discussion (ISD) with the Technical Inspection and Safety Commission (TIS) at CERN.

- In case of fire in the LHCb experimental cavern, the relative large amount of polystyrene scintillator material that is used in the construction of all calorimeter subdetectors (1 ton for SPD/PS, 17 tons for ECAL and 15 tons for HCAL) is a concern. The safety instructions for "the use of plastic and other non-metallic materials at CERN with respect to fire safety and radiation resistance" (IS41) will be followed, and appropriate smoke detection systems are foreseen.

- The ECAL and HCAL detectors are built from individual modules that are stacked on support structures to a height of 6.3 m and 6.8 m with a width of 7.8 m and 8.4 m for ECAL and HCAL, respectively. The weight of the individual modules that is to be manipulated during the installation phase is $\approx$30 kg for ECAL and 9.5 tons for HCAL. The ECAL has a total weight of 102 tons and is surrounded by a frame, while the HCAL weights 490 tons and is self supporting. The SPD/PS detector is hanging from the top and weights less then 20 tons, including all support beams. The installation procedure for all subdetectors will be determined according to the safety measures (safety code A5) and all lifting tools will be constructed following the corresponding norms (safety code D1 Rev.). The dynamic behaviour under seismic excitation will be studied in collaboration with TIS.

- About 400 high voltage channels are necessary to feed a total of about 7700 photomultiplier tubes for the whole calorimeter system. Depending on the final choice of photomultipliers, the operation voltage will be between 850 V and 1700 V, and the total current per channel will not exceed 2 mA. If the voltage will be above the limit of 1500 V (safety instruction IS33) the appropriate measures for cutting automatically the HV when opening the chassis will be undertaken.

- A 5 to 10 mCi radioactive Cs^{137} source is used for calibration purposes for HCAL. The source is encapsulated in a 2 mm diameter, 4 mm long stainless-steel tube that is welded at both ends. The source is sucked through stainless-steel pipes by a hydraulic system that is filled with distilled water. The system includes a garage to store the source, and a computer controlled pump and valves that allow to reverse the water flow direction. All measures have been taken to ensure compliance with the "Radioprotection Manual" (safety code F).

Chapter 6 Project Organization

6.1 Schedule

The overall work program and schedule for the calorimeter project is summarized in Figure 6.1. It covers the period from the start of the conceptual design up to the end of the project, when the overall system will be installed and commissioned in the LHCb cavern. The planning is such that the calorimeter system can be operated and fully commissioned together with all other LHCb detectors by mid 2005, the time at which LHC operation is anticipated.

The schedule is split into two main parts, the detectors and the electronics. The detectors planning is shown separately for the SPD/PS system, the ECAL, and the HCAL. All detectors consist of the mechanical and the optical components and include the photomultiplier tubes. The electronics planning is subdivided into the three different designs for SPD, PS, and ECAL/HCAL. It includes all front-end electronics components, cards and crates.

The conceptual design for both the detector and the electronics had started right after the LHCb technical proposal and is finalized for all detectors and the ECAL/HCAL electronics, while it is still ongoing for some parts of the SPD and PS electronics. These can proceed up to the end of 2001 without introducing any delays for production. The post TDR project planning includes some final optimization of the engineering design, the tendering, the preproduction and production of all components, the modules assembly, the acceptance tests of modules, and the installation and commissioning of the subsystems.

The pre-production of the SPD/PS detector will start in the beginning of 2001 in order to go into serial production six months later. The assembly of modules is expected to start in mid 2002, and the installation of the detector will follow at the second half of 2004 in order to be fully commissioned in the first quarter of 2005. For the ECAL detector some tooling and sub-components have been produced for a module 0 production. The full production of the 3300 ECAL modules will start in the beginning of 2001 in order to finish by the end of 2003, to leave about one year for installation of the detector and its electronics and for the commissioning. The HCAL detector will start regular production of the mechanics beginning of 2001 after successful completion of a module 0. The optics assembly of the 52 modules will start in parallel at the beginning of 2002, so that the installation of the first half detector can be anticipated at the beginning of 2004. The full HCAL detector will then be commissioned in the first quarter of 2005.

The PS electronics will proceed with the optimization of the engineering design till the end of 2002. Tendering and preproduction of some components will start already at the beginning of 2002 in order to finish the production and acceptance tests in the last

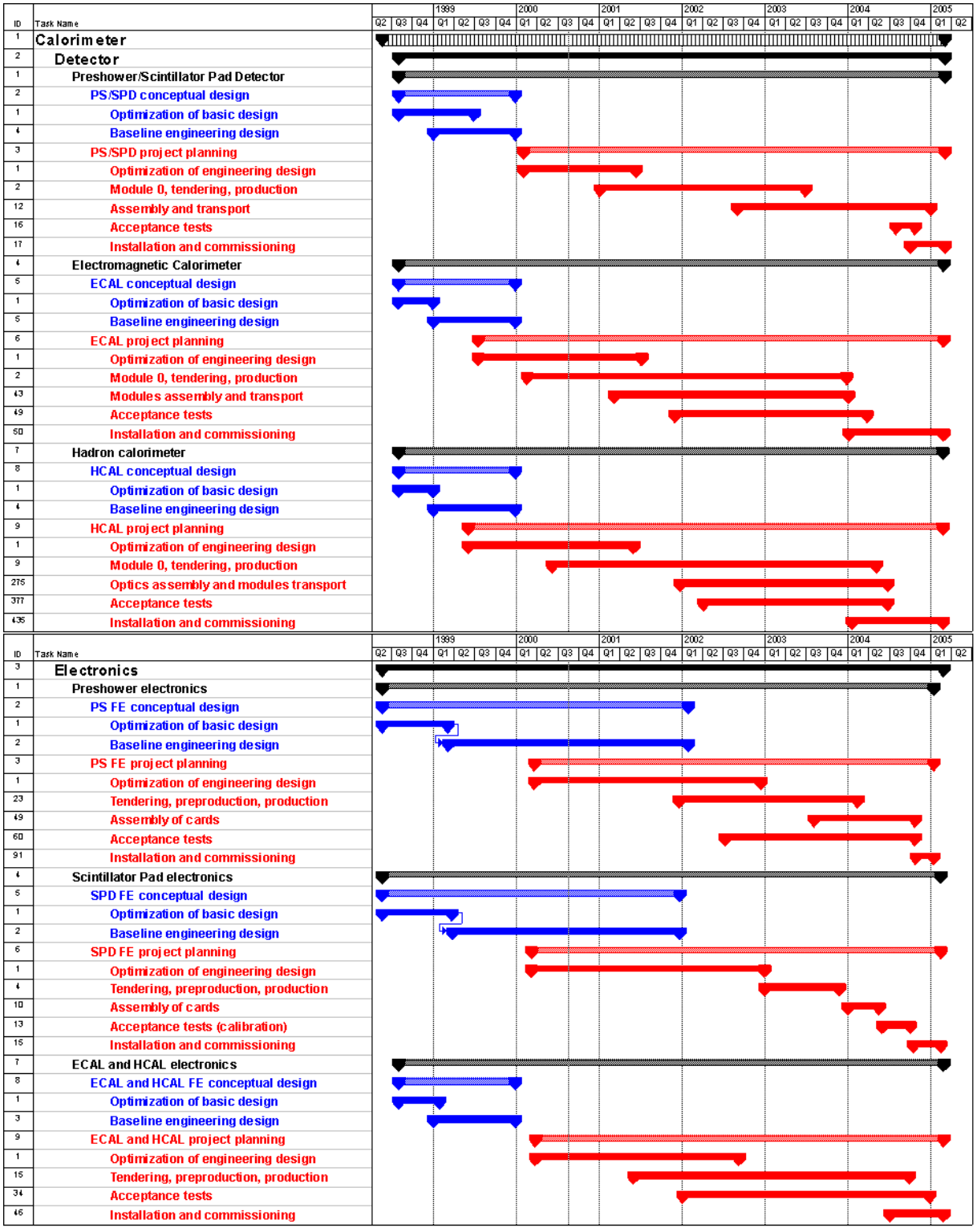

Figure 6.1: *Calorimeter project planning.*

quarter of 2004 and the installation in the first quarter of 2005. The engineering design of the SPD electronics will be further optimized till the end of 2002 so that a one year production period can start at the beginning of 2003. Acceptance tests will follow during 2004 so that the SPD electronics can be installed on the detector by the end of that year. The engineering design of the ECAL/HCAL electronics will be finalized in the second half of 2002, while tendering and preproduction of some components will already start in the middle of 2001. Production is expected to last till the last quarter of 2004 and acceptance tests will go on in parallel from beginning of 2002 onwards. Almost one year is allocated for installation and commissioning, that should finish in the first quarter of 2005.

Table 6.1: *Milestones for the calorimeter project.*

Sub-system	Task	Milestone
Detectors:		
SPD/PS	end of optimization of engineering design	7/2001
	start of serial production	7/2001
	end of supermodule assembly	12/2004
	end of installation	3/2005
ECAL	end of optimization of engineering design	5/2001
	start of serial production	6/2001
	end of module assembly	11/2004
	end of installation	2/2005
HCAL	end of optimization of engineering design	6/2001
	start of serial production	10/2001
	end of optics assembly	6/2004
	end of installation	12/2004
Electronics:		
SPD	end of optimization of engineering design	12/2002
	start of serial production	3/2003
	end of acceptance tests	9/2004
	end of installation	4/2005
PS	end of optimization of engineering design	12/2002
	start of serial production (of chips)	7/2002
	end of acceptance tests	11/2004
	end of installation	4/2005
ECAL/HCAL	end of optimization of engineering design	9/2002
	start of serial production (of cards)	10/2003
	end of acceptance tests	1/2005
	end of installation	4/2005

The schedule given in Figure 6.1 and discussed above is the preferred planning scenario based on realistic estimations of production rates and spending profiles. However, some tasks could be delayed without affecting the completion of other tasks in time. In Table 6.1 are summarized the crucial milestones, that are not all coinciding with the preferred

planning, but that have to be met in order not to delay the overall project completion by the middle of 2005.

6.2 Distribution of responsibilities

Institutes currently working on the LHCb calorimeter system are: CERN; University of Paris-Sud LAL Orsay and University of Clermont-Ferrand II (France); IFIN-NH Bucharest-Magurel (Romania); INR Moscow, ITEP Moscow and IHEP-Serpukhov Protvino (Russia); University of Barcelona (Spain).

How the major tasks of the calorimeter project are shared among the participating institutes, is listed in Table 6.2. Tasks like calorimeter specific software developments, including reconstruction algorithms and DAQ monitoring, will be shared among all participating institutes.

Table 6.2: *List of participating institutes in the calorimeter project.*

Task	Participating Institutes
Detectors:	
SPD/PS	CERN, INR
ECAL	CERN, ITEP
HCAL	Bucharest, CERN, IHEP
Support structures	CERN
Electronics:	
SPD	Barcelona
PS	Clermont
ECAL/HCAL	LAL
Photomultipliers and High Voltage:	
SPD/PS	Barcelona, Clermont
ECAL/HCAL	Bucharest, CERN, IHEP, ITEP, LAL

The overall responsibility for detector construction is shared among INR for SPD/PS, ITEP for ECAL and IHEP for HCAL. The responsible institutes for electronics production are LAL for ECAL/HCAL, Barcelona for SPD and Clermont for PS. CERN will have the responsibility for construction of the support structures, and a responsibility in the overall coordination and in the procurement of materials.

6.3 Cost

The cost of the calorimeter system has been evaluated, taking into account realistic labor prices in different countries. The total cost is 15'360 kCHF (with a western equivalent value of 17'610 KCHF), where the SPD/PS system contributes with 2'840 kCHF, the ECAL with 7'970 kCHF and the HCAL with 4'550 kCHF. Table 6.3 shows the cost estimates split according to the individual tasks of the participating institutes.

Table 6.3: *Calorimeter project costs (kCHF).*

Item	Cost
Detectors:	
SPD/PS	1'140[1]
ECAL	4'450[2]
HCAL	3'350[3]
Support structures	350
Electronics:	
SPD	110
PS	990
ECAL/HCAL	2'010
Photomultipliers and High Voltage:	
SPD/PS	550
ECAL/HCAL	2'410

For the mechanical and optical detector parts about 5% spare modules have been included. For the electronics equipment $\geq$10% spare cards and crates and 5% spare photomultiplier tubes have been accounted for. Wherever possible, the cost estimation of the sub-components is based on quotes from industry.

[1] the western equivalent value is 1'390 kCHF
[2] the western equivalent value is 5'450 kCHF
[3] the western equivalent value is 4'350 kCHF

References

[1] The LHCb Technical Proposal. CERN/LHCC 98-4.

[2] Performance of the Electromagnetic Calorimeter for π^0 detection in Physics channels, LHCb 2000-049.

[3] MC study of LHCb Preshower, LHCb 2000-030.

[4] Design and construction of the electromagnetic calorimeter for the LHCb experiment, LHCb 2000-043.

[5] LHCb hadron trigger and HCAL cell size and length optimisation, LHCb 99-035.

[6] Design and construction of the LHCb Scintillator-Pad/Preshower Detector, LHCb 2000-042.

[7] The Hadron Calorimeter Design and Construction, LHCb 2000-045.

[8] A.Bazilevsky *et al*, IEEE Transactions on Nuclear Science v.43, No.3 (1996).

[9] J.Badier *et al*, "Shashlik Calorimeter: Beam Test Results", Nucl. Instrum. Meth. A348 (1994) 74-86.

[10] ATLAS Tile Calorimeter TDR, CERN/LHCC/96-42, ATLAS TDR 3.

[11] A joint proposal for the Level 0 calorimetric triggers, LHCb 99-017.

[12] The Front-End Electronics for LHCb calorimeters, LHCb 2000-028.

[13] Scintillator Pad Detector Front-End Electronics, LHCb 2000-027.

[14] Front-End Electronics for the LHCb Preshower Detector, LHCb 2000-048.

[15] Investigation of widening of the π^0 mass peak with electronic defects, LHCb 2000-029.

[16] On the possibility of in situ calibration of LHCb calorimeters, LHCb 2000-051.

[17] Experimental performance of PS/SPD prototypes, LHCb 2000-031.

[18] KURARAY Corp., 3-10, Nihonbashi, 2 chome, Chuo-ku, Tokyo, Japan.

[19] BICRON Corp., 12345 Kinsman Rd. Newbury OH 440 USA.

[20] K.Hara *et al*, NIMA 411 (1998) 31.

[21] The WLS Fiber Time Properties study, LHCb 2000-039.

[22] CERN Program Library Long Writeup W5013 (1993).

[23] HAMAMATSU Photonics KK, Electron Tube Center, 314-5, Shimokanzo, Toyooka-village, Iwata-gun, Shizuoka-ken, 438-01 Japan.

[24] S.Aota *et al*, NIM A357 (1995) 71.

[25] Results of tagged photon test beam for the Scintillator Pad Detector, LHCb 2000-032.

[26] HERA-B Collaboration, HERA-B Proposal, DESY-PRC 94/02 May 1994;
HERA-B Collaboration, HERA-B Design Report, DESY-PRC 95/01 January 1995.

[27] Bazilevsky A. *et al*, IEEE Transactions on Nuclear Science v.43, No.3 (1996).

[28] J.Badier *et al*, "Shashlik Calorimeter: Beam Test Results", Nucl.Instrum.Meth. A348 (1994) 74-86.

[29] E.Tarkovsky, "The HERA-B electromagnetic calorimeter", Nucl.Instrum.Meth. A379 (1996) 515.

[30] Fiber density and uniformity of response of LHCb electromagnetic calorimeter, LHCb 2000-034.

[31] Radiation damage of LHCb electromagnetic calorimeter, LHCb 2000-033.

[32] Estimation of absorbed dose levels at possible locations for LHCb detector electronics, LHCb 2000-015.

[33] HCAL Prototype Design and Construction, LHCb 2000-35.

[34] HCAL Prototype Beam-test Results, LHCb 2000-36.

[35] The HCAL Optics Radiation Damage Study, LHCb 2000-37.

[36] The HCAL performance with irradated sub-components, LHCb 2000-38.

[37] Study of PMT FEU-115M and FEU-115M-10, LHCb 2000-040.

[38] LHCb Preshower Signal Characteristics, LHCb 2000-026.

[39] Very Front-End Electronics for LHCb Preshower, LHCb 2000-047.

[40] T.Sjöstrand and M.Bengtsson, Comp. Phys. Comm. **43** (1987) 367.

[41] Tuning of multiple interactions generated by PYTHIA, LHCb 99-028.

[42] An alternative high p_T electron and hadron trigger for LHCb, LHCb 98-058.

[43] An update of the 2×2 implementation for the Level 0 calorimeter triggers, LHCb 99-007.

[44] Proposal for a Level 0 calorimeter trigger system for LHCb, LHCb 99-013.

[45] Performance of the calorimeter triggers ($B \to \pi\pi, B \to D_s K/\pi, B \to J/\Psi K_s, B \to e + X$), LHCb 2000-050.

[46] ALICE Photon Spectrometer PHOS TDR, p.94, 1999.

[47] Some results of PMT studies, LHCb 2000-052.

[48] LHCb Magnet TDR, CERN/LHCC/2000-007, LHCb TDR 1;
Magnetic field of LHCb dipole magnet at subdetectors, cryoplant and electronics racks, LHCb 2000-084.

[49] The facility to control the production of shashlik type electromagnetic calorimeter, LHCb 2000-044.

[50] G.David *et al*, IEEE Transactions on Nuclear Science 45 (1998) 705.

[51] Zero dead-time charge sensitive shaper for calorimeter signal processing, LHCb 2000-041.

[52] The readout of the LHCb calorimeters, LHCb 2000-046.